Durham E-Theses

Magnetic studies on superconducting oxides

Al-Hawery, Abdulaziz S.

How to cite:

Al-Hawery, Abdulaziz S. (1990) *Magnetic studies on superconducting oxides*, Durham theses, Durham University. Available at Durham E-Theses Online: http://etheses.dur.ac.uk/6614/

IN THE NAME OF GOD,
MOST GRACIOUS, MOST MERCIFUL.

MAGNETIC STUDIES ON SUPERCONDUCTING OXIDES

by

ABDULAZIZ S. AL-HAWERY

B.Sc. Umm Al-Qura University

Graduate Society

A Thesis submitted to the University of Durham

in candidature for the degree of

Doctor of Philosophy

January, 1990

2 4 JUL 1991

To the memory of my Father

To my Mother

ACKNOWLEDGEMENTS

ABSTRACT

In the first part of this Thesis the structural and superconducting properties of some Yttrium-Barium-Copper-Oxides (YBCO) superconducting materials have been examined. These materials, which were discovered only about three years ago, have the important property that they become superconducting at temperatures below about 86K. Because this transition temperature (T_c) is well above the temperature (77K) of liquid nitrogen- a readily availible refrigerant- there is very considerable interest in potential technological applications. The nominal composition of YBCO material is $YBa_2Cu_3O_7$ and for superconductivity the value of x must be near $x = 7.0$. X-ray diffraction methods have been used to determine the lattice parameters and values of x for a range of oxides prepared from different starting materials by different routes. These structural studies were extended by Scanning Electron Microscopy which gave information about the grain size and microstructure of the materials. A major part of the work considered the development of an inductance probe technique for examining the superconducting properties. This technique was based on the Meissner effect and involved measuring the inductance of a small coil which was filled with superconducting material as a function of temperature and magnetic field. From these measurements several superconducting properties have been determined. These included the transition temperature (T_c), the percentage of superconducting material present in a given sample, the first critical field (H_{c_1}), and hysteresis. The critical field is the value at which an external magnetic field

penetrates into the superconductor to a depth known as penetration depth (λ) which corresponds to a non-superconducting layer. The values of H_{c_1} were all found to be about 15 gauss, rather smaller than those previously reported in the literature. The variation of λ with temperature was also examined and shown to be in excellent agreement with theory based on a Type II model. In an attempt to correlate these superconducting properties with the structural studies it was shown that the most promising superconductors were those in which the grain size was relatively large (greater than 10μm) and in which the grains were closely packed together.

In the second part of the Thesis some non-superconducting oxides were examined by magnetic resonance methods. In the first group of experiments the epr linewidths of the M=+1/2 $\leftrightarrow$ -1/2 transition of the Cr^{3+} spectrum of Cr/MgO single crystals and powders have been measured at 9GHz before and after annealing. The nominal chromium concentrations ranged from 800 to 15,000 ppm. Specimens were annealed at 500°C in oxygen for up to 150 hours. Annealing produced reductions in peak-to-peak linewidth ($\triangle H_{pp}$) which occurred in two stages. Each followed an exponential

$$\left[\triangle H_{pp}\right]_t = \left[\triangle H_{pp}\right]_0 exp^{(-\alpha t)}$$

and the initial (α_1) and final (α_2) decay rates were determined from the slopes of $Ln\left[\triangle H_{pp}\right]_t$ versus time plots. For single crystals all the values of α_1 were about 0.04 h^{-1}; the smaller values of α_2 were concentration dependent ranging from 0.9×10^{-3} to $1.25 \times 10^{-3} h^{-1}$ for the two sources of strain. The rapid decay rate is associated with cationic vacancy strain relief and the slower decay with removal of lattice distortion

brought about when the Mg^{2+} ions are replaced by Cr^{3+} dopant ions. Similar effects were observed with powders but in these both types of lattice strain were relieved at a slower rate in the powder than in the corresponding single crystal, e.g. for 3600 ppm Cr, $\alpha_1 = 0.016h^{-1}$ and $\alpha_2 = 1.0 \times 10^{-3}h^{-1}$. In the second group of experiments the mechanisms of magnesiochromite formation were studied and the effect of this on epr linewidth was examined. The results of both groups of experiments were related to the more general problem of the dipolar mechanisms responsible for the variation of epr linewidth with concentration in the Cr/MgO system.

CONTENTS

CHAPTER ONE

INTRODUCTION

The main work described in this Thesis is concerned with magnetic studies on some superconducting oxides. The magnetic and superconducting properties are closely related to the composition and microstructure of the material and consequently the purely magnetic studies described had to be supplemented by a considerable amount of structural appraisal of the material. The particular oxides investigated here were of the Yttrium-Barium-Copper Oxide type and among the characterization techniques adopted was electron paramagnetic resonance (e.p.r). This latter technique was used to examine some other oxide ceramics, in particular chromium doped magnesium oxide (Cr/MgO) which is a refractory insulator but not a superconducting material. Consequently, for convenience, the Thesis is divided into two sections, Part I being concerned with the structural and magnetic properties of superconducting oxide ceramics and Part II with the nature of magnetic interactions of the paramagnetic dopant in the diamagnetic magnesium oxide host lattice.

The discovery of the so-called high T_c superconductors occurred in 1986 when Bednorz and Muller [1.1] reported superconducting behaviour in metallic, oxygen-deficient compounds in the Ba-La-Cu-O system with the composition $Ba_x La_{5-x} Cu_{5(3-y)}$. One characteristic of any superconductor is that below a certain temperature, known as the critical temperature T_c, the resistance falls to zero. For all previously known

1

superconducting materials the critical temperatures T_c lie in the range of temperature below about 20K and consequently it was usually necessary to use liquid helium refrigerant to enable the superconducting properties to be utilized. Examples of conventional superconductor applications requiring liquid helium refrigerants are superconducting magnets (which are used to produce very high magnetic fields) and Superconducting Quantum Interference Devices or SQUIDS which are used for measuring very small magnetic fields. The attraction of the new oxide material reported by Bednorz and Muller [1.1] was that the critical temperature was in the 30K range, considerably higher than those of previously known materials. The next major step in the development of high T_c materials occurred in 1987 when Chu and his co-workers [1.2] reported that a stable and reproducible superconducting transition between 80 and 93K had been unambiguously observed both resistively and magnetically in a new Y-Ba-Cu-O compound. This discovery generated interest worldwide because T_c was above the temperature of liquid nitrogen (77K) and hence the possibility could be visualised that the expensive and inconvenient liquid helium requirement could be replaced by the relatively inexpensive and readily available liquid nitrogen. There was also much speculation regarding the possibility of room temperature superconductivity which would of course have many implications for electrical engineering and technology. YBCO belongs, like other new high temperature superconductors, to a structurally flawed crystallographic family known as perovskites. Chu's superconducting powder was composed of the elements yttrium, barium and copper in the ratio 1:2:3 and so is called a 1-2-3 superconductor. The superconducting 1-2-3 YBCO

2

chemical formula is $YBa_2Cu_3O_{7-x}$.

It is helpful first to give a brief summary of the magnetic properties of conventional superconductors. More complete discussions are given in textbooks by Kittel [1.3] and Rose-Innes [1.4]. The most obvious characteristic of all superconductors is that below their transition temperatures (T_c) superconductors have zero resistivity. In the direct measurement of resistance it is usual to employ the four probe method. In this four co-linear contacts are made to a sample of known cross-sectional geometry, the outer pair acting as current leads and the inner pair being used to measure the voltage developd across a known length of sample. This enables the resistance, usually expressed as the ratio of the resistance at given temperature to that at room temperature, to be measured as a function of temperature. The superconducting transition for the Type I superconductor tin is shown in Figure 1.1. For the pure material the transition is very sharp (the temperature width is less than 0.001K) but the addition of impurities has the effect of broadening the transition very considerably. Experimentally it is difficult to measure the extremely low resistance found below T_c and the method adopted has usually been the persistent current technique. Here a current is induced in a closed loop of a superconducting wire maintained below its critical temperature and the magnitude of the magnetic field produced by this current is monitored by a small search coil as a function of time; from the lack of measurable decay of the current it has been deduced that the resistance in the superconducting state is virtually zero. In addition to temperature there is another factor which can cause a transition from the superconducting to the normal (resistive)

3
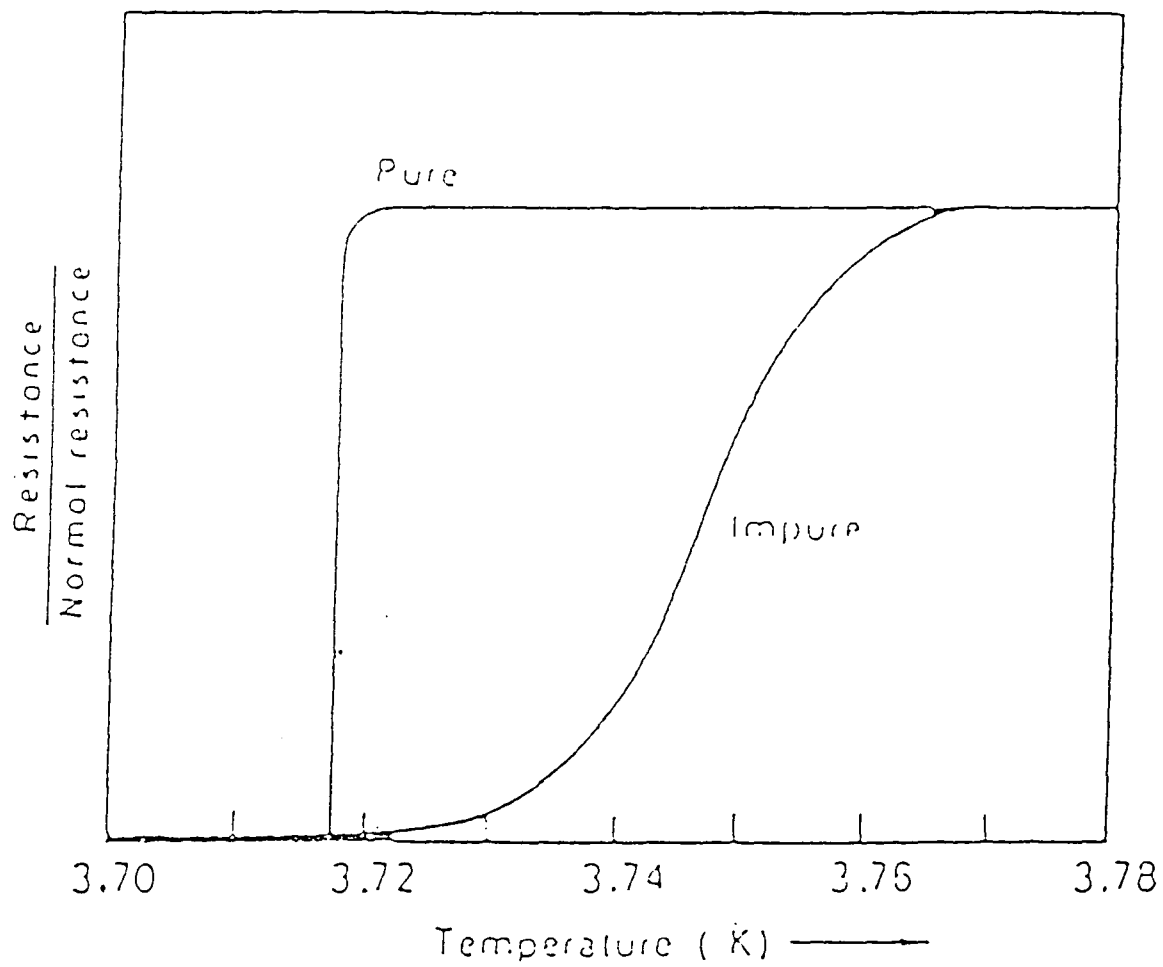
Figure 1.1. Superconducting transition in tin.

state. This is the application of an external magnetic field. Superconductors may be broadly divided into Type I and Type II, according to their quite different behaviour in a magnetic field. Superconductors Type I have a single critical field value and superconductors Type II have two critical field values. For Type I superconductors the external magnetic flux cannot penetrate the body, Figure 1.2, and the flux penetration takes place only when H_c is reached. Examples of this type of behaviour are mercury [1.5] which has T_c=4.2K and H_c=400G and lead [1.5] for which T_c=7.2K and H_c=800G. Some further examples of the critical temperature and critical field of the superconducting elements are given in Table 1.1. As the Table shows the value of H_c is different for each superconducting metal.The value of H_c for a particular element is also temperature dependent. Experimentally it has found that the variation follows the relation

$$H_c = H_0[1 - (T/T_c)^2] \tag{1.1}$$

where H_0 is the critical field at absolute zero and T_c is the transition temperature. This form of behaviour is shown in Figure 1.3. For Type II superconductors, Figure 1.4, there are two critical fields. The first critical field (H_{c1}) occurs when the flux starts to penetrate the material. With increase of the magnetic field the material enters a mixed state between H_{c1} and H_{c2} until, when the higher field H_{c2} is reached, the sample becomes fully normal. Some conventional Type II materials are niobium-tin (Nb_3Sn) [1.6] for which T_c=18K and H_{c2}=210kG and niobium aluminium (Nb_3Al) [1.7] which has a slightly higher critical temperature of T_c=19K and a substantially higher value of H_{c2} of 320kG, molydenium-rhenium ($MO_3 - Re$) for which T_c=10K

4

Element	T_c (K)	H_0 (Gauss)
Aluminium	1.19	99
Cadmium	0.56	30
Gallium	1.09	51
Indium	3.41	283
Lead	7.2	800
Mercury	4.2	400
Osmium	0.7	65-82
Rhenium	1.70	201
Ruthenium	0.49	66
Tantalum	4.5	830
Tin	3.7	306
Titanium	0.40	100
Vanadium	5.3	1310
Zinc	0.88	53
Zirconium	0.75	47

Table 1.1 : Critical temperatures and fields of some superconducting elements.
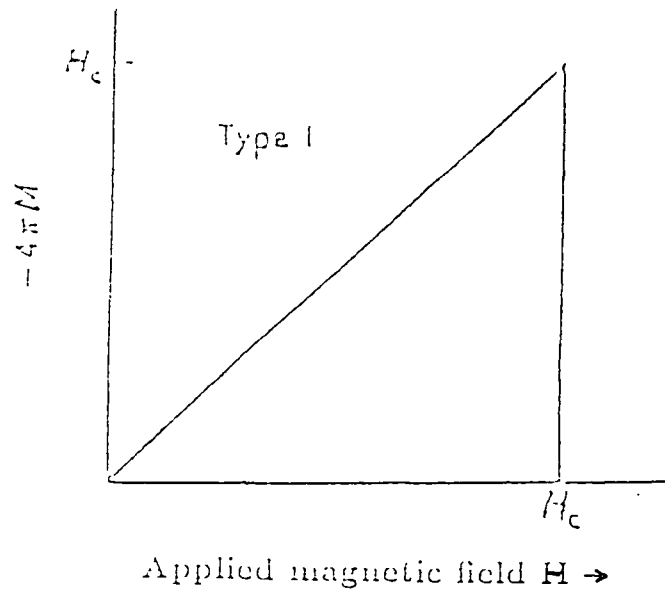
Figure 1.2 : Superconducting magnetization curve of a Type I super-conductor.
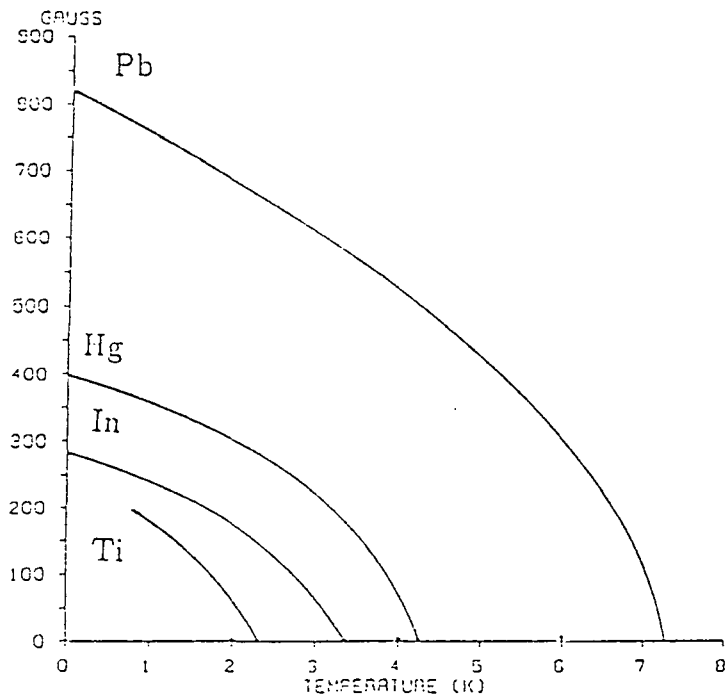
Figure 1.3. Critical field of some superconductors.

Applied magnetic field H →
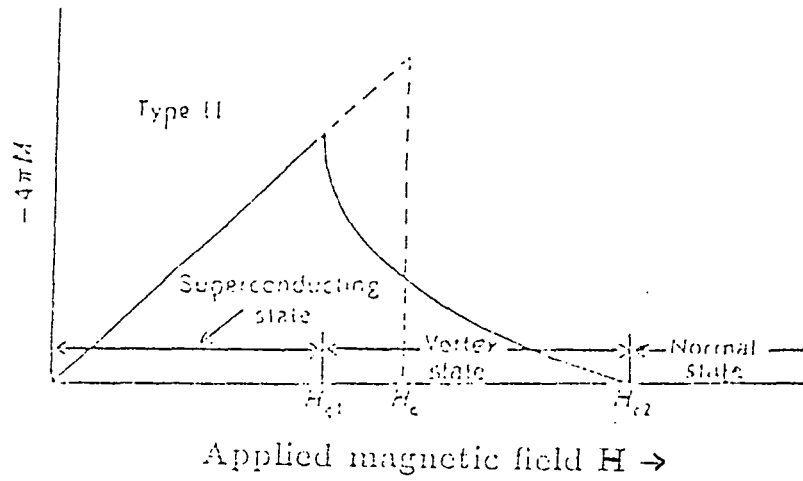
Figure 1.4 : Superconducting magnetization curve of a Type II super-
conductor.
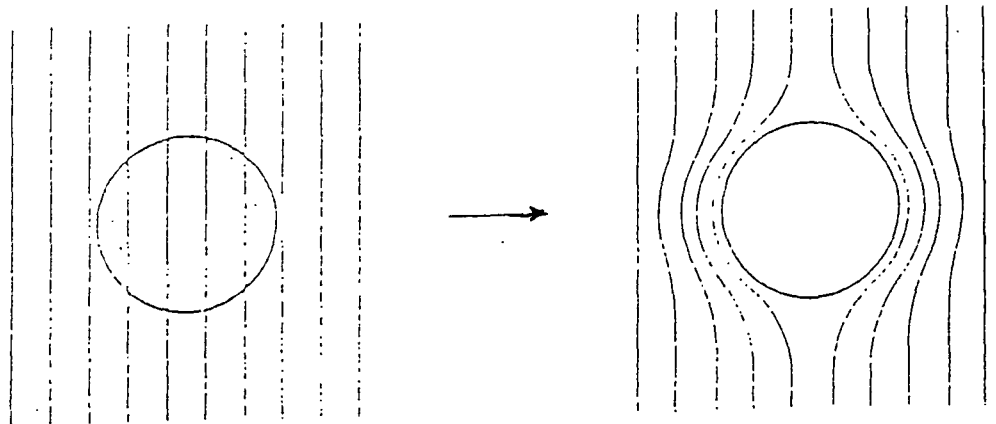
Figure 1.5. Meissner effect in a superconducting sphere cooled in a
constant applied magnetic field.

and H_{c2}=8.4kG and titanium-niobium $(Ti_2 - Nb)$ for which T_c=9K and H_{c2}=100kG [1.4]. In addition there is another field of interest at low temperatures. If a magnetic field H is applied to a superconductor, and the temperature is reduced below T_c, all the magnetic flux is expelled from the body of the material (see Figure 1.5). This explusion of magnetic flux is called the Meissner effect [1.8]. Early workers in superconductivity also discovered that there was an upper limit to the current which could be passed along a piece of superconductor if it were to remain resistanceless. This is called the critical current, though it is more usual to refer to the critical current density J_c which takes account of the cross section of the sample. The critical current is related to the critical magnetic field strength H_c already mentioned. Thus a superconductor loses it's zero resistance when, at any point in the surface, the total magnetic field strength due to the contribution from both the transport current and any external applied magnetic field exceeds the critical field strength H_c. This implies that the stronger the applied magnetic field the smaller is the critical current. If there is no applied magnetic field the only magnetic field will be that generated by the transport current and in this case the critical current is that current which generates the critical magnetic strength H_c at the surface of the superconductor.

There have been several theories of conventional Type I and Type II superconducting behaviour but to date no complete theory of the new oxide superconductors, which form the subject of Part I of this Thesis, has been announced. Although the development of quantum mechanics in the 1920's led to the understanding of ordinary electrical conduction in metals, the origins of superconductivity were not clear

until 1956. This situation encouraged the development of phenomenological theories. These theories, although not attempting to account for the origin of superconductivity, have established that most superconducting phenomena can be derived from a small number of empirical postulates. An early step was made by Gorter and Casimir [1.9], who showed that the thermodynamic properties of superconductors could be accounted for by assuming that their conduction electrons were divided into fluids or phases. The electrons in one phase were considered to have their normal properties, but a proportion was assumed to be condensed into a lower free energy phase in which it could carry current without interacting, that is, without ohmic dissipation. An assumption was that the fraction of electrons in the condensed phase was unity at absolute zero and decreased towards zero as the critical temperature was approached. Following the discovery of the Meissner effect, it became clear that the electromagnetic properties of a superconductor could not be predicted directly from Maxwell's equations for a metal, assuming zero resistivity. In 1935 F. and H. London showed that most of the electromagnetic properties of superconductors, including the Meissner effect, could be accounted for by Maxwell's equations with the addition of the expression

$$\frac{ne^2}{mc}H + curlJ = 0 \qquad (1.2)$$

where J is the current density, H the field, and n,e and m are respectively the concentration, charge and mass of the conduction electrons. London's theory predicted that a magnetic field would exist within a superconductor but that its value would

vary exponentially with depth according to

$$H = H_0 e^{-\frac{x}{\lambda}} \tag{1.3}$$

where

$$\lambda^2 = \left(\frac{mc^2}{4\pi n e^2}\right) \tag{1.4}$$

Here H is the field at a depth x inside a semi-infinite superconductor whose surface field is H_0. The quantity λ is known as the penetration depth. Equation (1.2) predicts that the field should fall to zero inside a superconductor in agreement with the Meissner effect and that it should do so exponentially with a decrement λ. This prediction is found to be approximately correct. The penetration depth can be measured experimentally and is found to vary with temperature, increasing from a value $\lambda(0)$ at absolute zero towards infinity at T_c. Experimentally, the temperature dependence of λ is found to be given by the relation.

$$\frac{\lambda(T)}{\lambda(0)} = \left[1 - \left(\frac{T}{T_c}\right)^4\right]^{-\frac{1}{2}} \tag{1.5}$$

For lead, mercury, tin and indium $\lambda(0)$ lies between 4 and 6×10^{-6} cm. It is found that equation 1.5 can be deduced from the London theory by thermodynamic arguments if n in equation 1.4 is regarded as the concentration of the superconducting portion of the conduction electrons as calculated from the two-fluid model. Although later work has shown that the concepts of the two-fluid model and the equations of the London theory are only exact under certain limiting conditions, these concepts and equations still provide a convenient framework for describing many of the phenomena of superconductivity.

7

The London theory and the two-fluid model did not attempt to explain the origin of superconductivity. The modern microscopic theory, first proposed by Bardeen, Cooper and Schrieffer [1.10] and called the BCS theory, goes a long way towards explaining most of the properties of the superconducting state. No theory can yet explain why only certain metals, alloys and compounds become superconducting at low temperatures. The BCS theory predicts that a special type of attractive interaction between conduction electrons, opposing the normal electrostatic repulsion, can occur in the collective system of electrons and lattice taken together. The attraction takes place by the successive emission and absorption of short-lived virtual phonons between pairs of electrons, and has the effect of pairing-off electrons with opposite spin and with approximately opposite wave vectors or linear momenta. Calculation shows that this attractive force between the electrons of a pair extends over a relatively long distance, which is of the order of 10^{-4} cm;this distance is called the Coherence Length ξ. The momenta of the electron pairs are distributed statistically about zero. The non-zero values of paired momenta, within the distribution, are equivalent to elementary super-currents. Pairing is only effective for electrons close to the Fermi surface; i.e. those with energies lying within about kT_c of the Fermi energy W_F. The attraction between an electron-pair means that the total energy of a pair is lower, by a quantity 2Δ, than the sum of the energies of the two unpaired electrons. At T=0, all electrons close to the Fermi surface pair off and a superconducting energy gap, 2Δ, exists between the superconducting ground state and the normal excited states. The BCS theory predicts that the value of the superconducting energy gap parameter 2Δ

is

$$2\triangle = 3.5kT_c \qquad\qquad (1.6)$$

where T_c is the transition temperature. At the same time, the density of states N(W) are piled up on either side of the energy gap, Figure 1.6a. The pairing off is a collective process involving all electrons near the Fermi surface, together with the lattice through which they move. At finite temperatures, $0 < T < T_c$, some pairs are destroyed by thermal excitation across the energy gap into normal conduction states, and the strength of the collective pairing interaction is reduced. The energy gap becomes smaller and approaches zero as T approaches T_c, Figure 1.6b. At T_c, the normal Fermi distribution is restored.

As regards the new high T_c superconductors there is at present no single complete theory, despite an extremely extensive literature. Some of the recent developments have been reviewed by Phillips [1.11] and an even more recent survey has been given by Ehrenreich and Turnbull [1.12] It is very clear however the occurrence of electron pair formation, which is a pre-condition for superconductivity, is very closely related to the nature and crystallography of the unit cell of the material. Hence there is a need to correlate the measurement of the various superconducting properties with a detailed knowledge of the microstructure of the material investigated.

In Part I of this Thesis Chapter Two is concerned with structural studies of YBCO. The description of the measurements and observations of superconducting properties commences in Chapter Three which is concerned with inductance probe

(a)

(b)
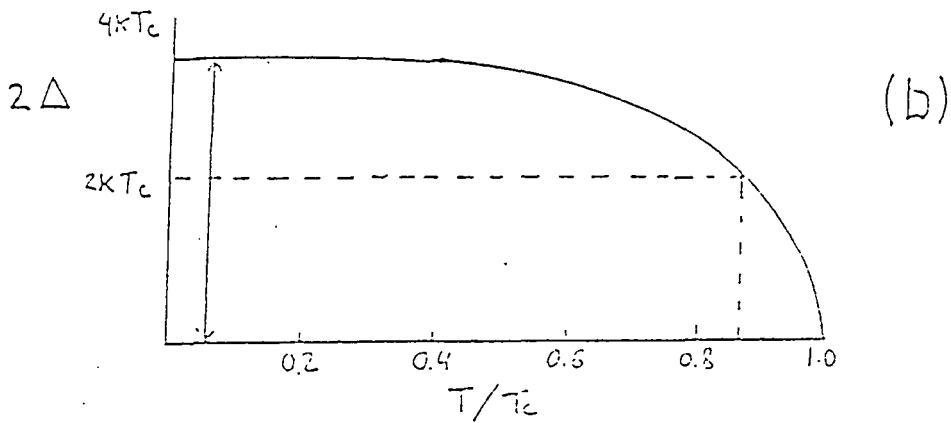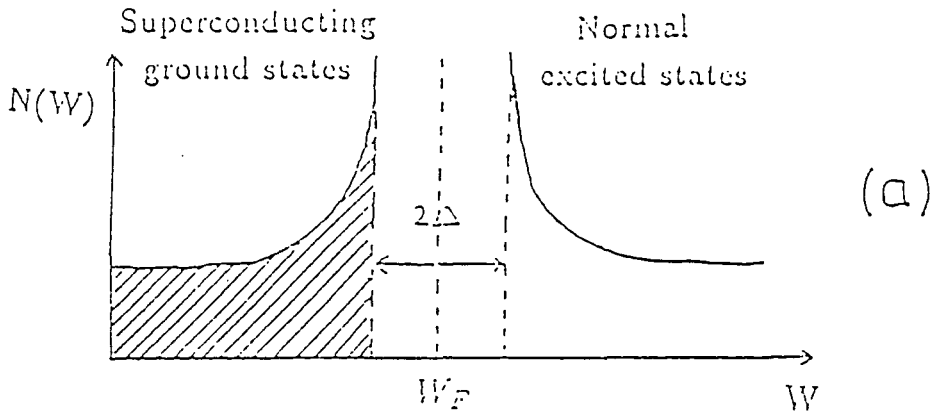
Figure 1.6. (a) Density of states $N(W)$ as a function of energy. At 0K, all the shaded states are occupied. At higher temperatures, there is some excitation across the energy gap.

(b) Variation of the energy gap 2Δ with T as predicted by the BCS Theory

techniques and measurements. Chapter Four reports further studies concerned primarily with critical field and hysteresis observations. Part I continues with Chapter Five which describes e.p.r studies on YBCO and provides additional structural information which complements that obtained by the x-ray and electron-microscopic techniques reported in Chapter Two. Some conclusions on the results obtained in Part I are given in Chapter Six.

Part II of this Thesis is also concerned with the magnetic behaviour of some oxide ceramics but the difference is that these oxides, which were a range of magnesium oxide single crystals doped with chromium at various concentrations, were not superconducting. Magnesium oxide is a refractory insulating material and is of interest for both scientific and technological reasons. On the technological side magnesium oxide finds it's major application as the refractory insulator used in heating elements. Here the major problem is that the insulator must withstand a very high alternating voltage, usually 240 v. a.c, while at temperatures of about 800°C; it must also be in powder form such that the powder has the correct flow characteristics to enable it to be packed into the space between the heater and its surrounding sheath and also to be moulded with the sheath in the manufacture of the heating element. On the scientific side the cubic unit cell of magnesium oxide makes it a very suitable material to use as a host lattice for the examination of magnetic interactions between paramagnetic ions which may be introduced, usually substitutionally for magnesium, by including of controlled amount of the dopant oxide during crystal growth. There have been a number of studies of both the dielectric behaviour of doped magnesium

oxide [1.13-1.18] and of the e.p.r behaviour of several paramagnetic ions particularly ions of the iron group [1.19-1.23]. In these magnetically dilute solids the magnetic interaction between the paramagnetic centers is dipolar broadening and the MgO system provides a very good basis with which to test dipolar broadening theories. The work described in Part II is entirely concerned with e.p.r studies on Cr/MgO and extends the work previously reported (c.f [1.24]) in two directions. These extensions primarily concerned the investigation of two factors which may require corrections to observed experimental data to be made before comparisons with theoretical models are possibile. In Chapter Seven the effect of lattice strain in broadening the e.p.r linewidth in Cr/MgO single crystals is discussed and in Chapter Eight another factor, that of magnesium chromite formation, is described and its effect in e.p.r linewidth discussed.

REFERENCES

1.1. J.G.Bednorz and K.A.Muller, Z-Phys B-Cond. Matt. 64, 189, (1986).

1.2. M.K.Wu, J.R.Ashburn, C.J.Torng, P.H.Hor, R.L.Meng, L.Gao, Z.J.Huang, Y.Q.Wang and C.W.Chu, Phys. Rev. Lett. 58, 908, (1987).

1.3. C.Kittel, "Introduction to Solid State Physics" 5th ed, John Wiley & Sons, U.S.A. (1976).

1.4. A.C.Rose-Innes and E.H.Rhoderick, "Introduction to Superconductivity", 2nd ed, Pergamon Press, U.K. (1976).

1.5. H.Kamerlingh Onnes, Akad and van Wetenschappen, (Amsterdam) 14, 113, (1911).

1.6. T.G.Berlincourt and R.R.Hake, Phys. Rev. 131, 140, (1963).

1.7. Y.Shapira and L.J.Neuringer, Phys. Rev. 140, A1638, (1965).

1.8. W.Meissner and R.Ochsenfeld, Naturwiss, 21, 787, (1933).

1.9. C.J.Gorter and H.B.G.Casimir, Physica, 1, 306, (1934).

1.10. J.Bardeen, L.N.Cooper and J.R.Schrieffer, Phys. Rev. 108, 1175, (1957).

1.11. J.C.Phillips, "Physics of High T_c Superconductors" 1st. ed. Academic Press Inc. London Ltd. U.K. (1989).

1.12. H.Ehrenreich and D.Turnbull, "Solid State Physics" Vol. 42, Academic Press, Inc. London (1989).

1.13. J.S.Thorp and N.Enayati-Rad, J. Mater. Sci. 16, 255, (1981).

1.14. J.S.Thorp, B.L.J.Kulesza, N.E.Rad and S.V.J.Kenmuir, Ibid. 16, 1052, (1981).

1.15. J.S.Thorp, M.D.Hossain and S.V.J.Kenmuir, Solid State Commu. 38, 455, (1981).

1.16. M.D.Hossain and J.S.Thorp, Pakistan J. Sci. Industr. Res. 26(6), 361, (1983).

1.17. A.D.Inglis, G.H.Russell and J.S.Thorp, J. Mater. Sci. 17, 2939, (1982).

1.18. J.S.Thorp, N.E.Rad, D.Evans and C.D.H.Williams, J. Mater. Sci. 21, 3091, (1986).

1.19. J.S.Thorp and A.R.Skinner, J. Magn. Magn. Mater. 69, 34, (1987).

1.20. G.Rius and A.Herve, Solid State Commu. 11, 795, (1972).

1.21. J.S.Thorp, M.D.Hossain and L.J.C.Bluck, J. Mater. Sci. 14, 2853, (1979).

1.22. J.S.Thorp, R.A.Vasquez, C.Adcock and W.Hutton, J. Mater. Sci. 11, 89, (1976).

1.23. J.S.Thorp, M.D.Hossain, L.J.C.Bluck and T.G.Bushell, J. Mater. Sci. 15, 903, (1980).

1.24. A.R.Skinner, Ph.D. Thesis, Durham University (1986).

Part I
Studies on
Superconducting Oxides

CHAPTER TWO

STRUCTURAL STUDIES OF YBCO

2.1 X-ray Diffraction Method.

2.1.1 Introduction.

Both x-ray diffraction and neutron diffraction methods have been used extensively to determine the unit cell and the lattice parameters of YBCO. The structure of $YBa_2Cu_3O_{7-x}$ is shown in Figure 2.1 [2.1]. It consists of corner-linked CuO_4 square-pyramidal groups nominally containing Cu^{2+} connected as sheets in the a-b plane. There are also distorted square-planar CuO_4 groups (which are nominally Cu^{3+}) corner-linked parallel to the b direction. It has been shown as, will appear later, that the superconducting behaviour of YBCO is critically dependent on precise details of the structure and in particular the stoichiometry of the material. No complete theory has been put forward but most models assume that these planes and chains are involved. For example Nishino et al [2.2] have proposed a model for superconducting Cu oxides based on the hybridization of the oxygen P band with the d band of Cu while Macfarlane et al [2.3] examined in detail the effect of oxygen stoichiometry on the phonon spectrum. Here conventional photographic powder diffraction methods have been used to characterize a number of YBCO samples which had been prepared by different methods. The spectra were obtained with a Phillips 11.50 cm diameter camera using filtered CuK_α radiation.

14
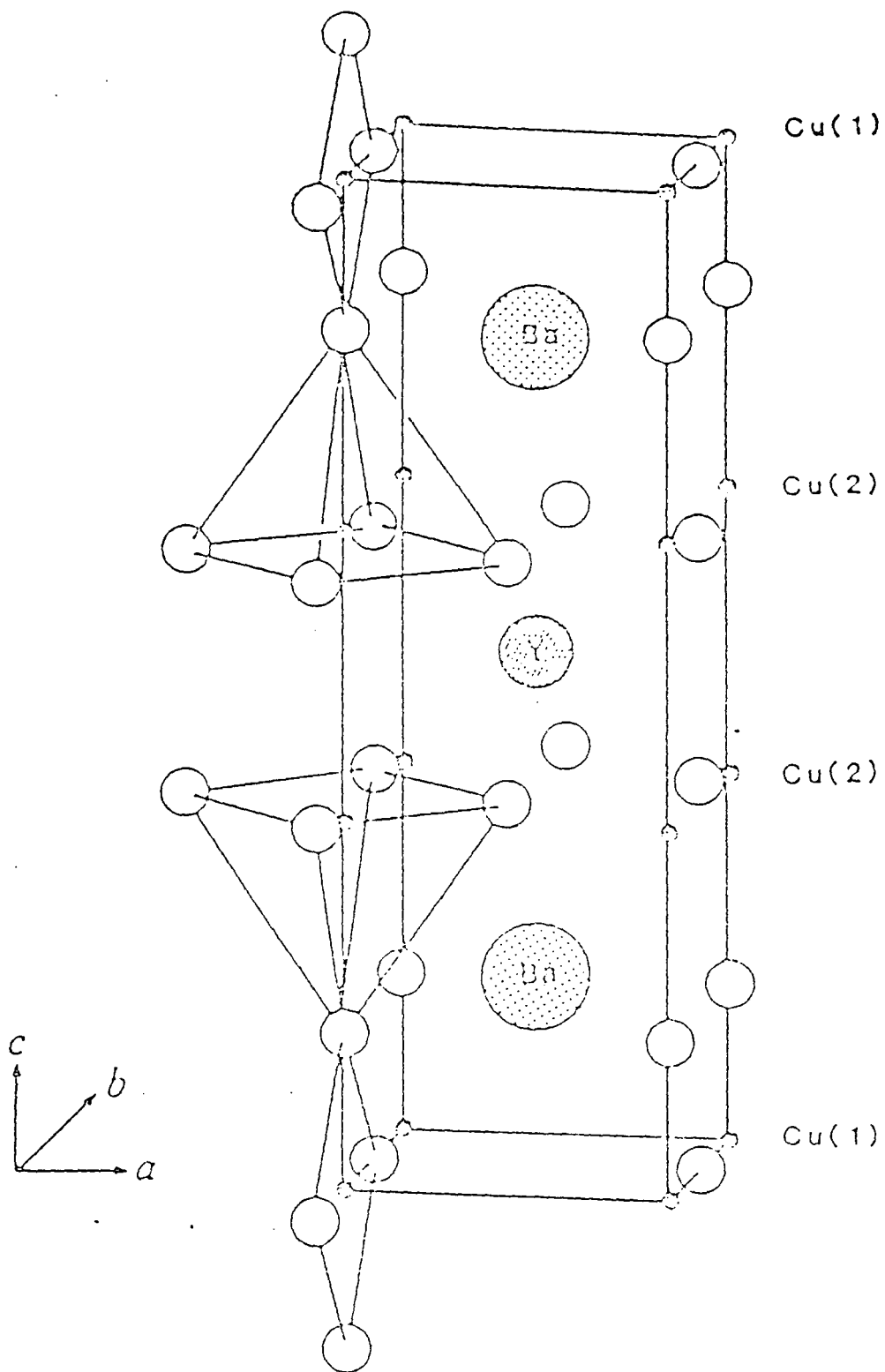
Figure 2.1   Structure of YBa$_2$Cu$_3$O$_{7-x}$.

The interplanar spacings (d-values) were obtained by measuring the line positions with a vernier ruler, deriving the corresponding Bragg angles θ and obtaining d from the Bragg equation.

$$\lambda = 2d_{hkl} \, sin\theta_{hkl} \qquad (2.1)$$

This gives data in the form shown in Table 2.1 which lists the d-values of all the lines observed for specimen (1A) together with a visual estimate of their relative intensities.

The spectra for other samples were obtained and analysed in a similar way.

2.1.2 Comparison of Observed d-values with Previous Data

There is considerable disagreement between the results for d-values which have been published by different authors. This makes it difficult to find the correct standard of reference on which to base further analyses for the derivation of the unit cell parameters. Here West's paper [2.4] has been used as the most reliable recent publication. A comparison of the d-values observed for specimen (1A) and West's data is given in Table 2.2. The fit of both the number of lines observed and the d-values is very good. The agreement between the d-value derived from the photographically recorded spectra and West's calculation values is within 0.5%; the error in d-value determination was estimated as $\pm 0.008 \mathring{A}$. West's calculation, based on an orthorhombic unit cell, showed that 32 lines should be present in the spectrum and of these 21 lines have been observed, the remainder being of too weak intensity to be recorded. Three lines were seen which were not in West's calculated listing; these

15

No of Line	d-value ($\mathring{A}$)	I	No of Line	d-value ($\mathring{A}$)	I
1	3.826	w	11	1.731	w
2	2.863	m	12	1.660	w
3	2.725	vs	13	1.650	w
4	2.333	m	14	1.579	s
5	2.228	m	15	1.488	vw
6	2.033	vw	16	1.428	vw
7	1.977	vw	17	1.371	vw
8	1.943	m	18	1.361	m
9	1.911	m	19	1.293	w
10	1.772	w	20	1.227	m
			21	1.211	m

Table 2.1 : Interplanar spacings for specimen (1A)

West's data				Specimen 1A	
hkl	d(obs.)Å	d(calc.)Å	I	d(obs.)Å	I
002	5.8700	5.8469	vw	-	
003	-	3.8980	-	-	
010	3.8889	3.8871	m	-	
100	3.8202	3.8206	w	3.826	w
012	3.2377	3.2370	w	-	
102	3.1977	3.1983	w	-	
013	2.7524	2.7524	s	-	
103	-	2.7285	-	-	
110	2.7265	2.7248	vs	2.725	vs
111	2.6536	2.6537	vw	-	
112	2.4694	2.4698	w	-	
005	2.3373	2.3388	m	2.333	m
014	-	2.3364	-	-	
104	2.3206	2.3217	w	-	
113	2.2321	2.2332	m	2.228	m
020	1.9439	1.9435	s	1.943	m
200	1.9092	1.9103	m	1.911	m
115	1.7741	1.7747	w	1.772	w
120	1.7321	1.7323	vw	1.731	w
210	1.7146	1.7144	vw	-	
121	-	1.7136	-	-	
007	1.6705	1.6706	vw	-	
122	1.6604	1.6609	vw	1.660	w
212	1.6461	1.6452	vw	1.650	w
123	1.5832	1.5830	s	1.579	s
213	1.5693	1.5694	m	-	
025	1.4942	1.4948	vw	-	
205	-	1.4795	-	-	
214	1.4787	1.4789	vw	1.488	vw
117	1.4247	1.4242	vw	1.428	vw
026	1.3765	1.3762	vw	1.371	vw
220	1.3625	1.3624	m	1.361	m

Table 2.2 : Comparison of d-values of specimen (1A) with West's published listing,
w=weak, m=medium, s=strong, v=very.

had d-values of 2.863 Å (m), 2.033 Å (vw) and 1.977 Å (vw) but have not yet been identified. Comparison of the same experimental x-ray spectrum of 1A with other published listings of d-values [2.5 - 2.9] shows the wide range of discrepancy encountered. This comparison is made in Table 2.3 (It will be seen later that the d-values depend on the stoichiometry and this may provide a reason for some of the lack of agreement shown in Table 2.3).

2.1.3 Derivation of Lattice Parameters and Oxygen Stoichiometry.

It can be seen from Tables 2.2 and 2.3 that the closest fit is with West's data which is for an orthorhombic unit cell of composition $YBa_2Cu_3O_{6.90}$. The relation between the interplaner spacing (d) and the lattice parameters (a,b,c) for an orthorhombic cell is

$$\frac{1}{d^2} = \frac{h^2}{a^2} + \frac{k^2}{b^2} + \frac{l^2}{c^2} \tag{2.2}$$

and the a, b, c values can be obtained most easily from the d-values of the (200), (020) and (005) reflections respectively. For specimen 1A it is found that a=3.822Å, b=3.886Å, c= 11.665Å. These may be compared with West's values of a=3.8206Å, b=3.887Å, c=11.693Å and it can be seen that there is fair correlation.

It is useful here to summarise some of West's results. The crystal structure and electrical properties of $YBa_2Cu_3O_x$ depend on the value of x. At high x values, eg. 7.0, the phase is orthorhombic and becomes superconducting at low temperature. At lower values, eg. 6.0, the phase is tetragonal and non-superconducting at all

2θ	d-values ($\overset{\circ}{A}$)					
	1A	R.Beyer et al[2.5]	A.Reller et al[2.6]	R.Cava et al[2.7]	Binod Kumar et al[2.8]	D.Blank et al[2.9]
23.25	3.826	3.821	3.825	3.822	3.826	3.820
31.25	2.863					
32.875	2.725	2.727		2.726	2.726	2.726
38.60	2.333	2.336	2.332	2.336	2.332	2.334
40.50	2.228		2.231	2.232		
44.575	2.033					
45.90	1.977					
46.75	1.943	1.948	1.943	1.946	1.943	1.945
47.60	1.911	1.910	1.912	1.911	1.912	1.910
51.575	1.772	1.774	1.772	1.775	1.770	1.773
52.90	1.731		1.732	1.734	1.731	1.733
55.35	1.660	1.661	1.660	1.662	1.661	1.662
55.70	1.650	1.646				
58.45	1.579	1.584			1.580	
62.425	1.488				1.491	1.494
65.375	1.428					
68.425	1.371				1.374	1.375
69.00	1.361				1.362	1.363
73.225	1.293				1.296	
77.875	1.227				1.227	
79.10	1.211				1.211	

Table 2.3 : Comparison of d-values for specimen (1A) with other published data.

temperatures. The value of x in a particular sample depends on processing conditions, especially temperature and oxygen partial pressure.

The orthorhombic-tetragonal transition occurs with decreasing x and appears to be a continuous, second order transition [2.10] The transition has been observed directly by high temperature x-ray and neutron diffraction [2.11,2.12]. Starting with a sample of x=7.0, the sample starts to lose oxygen on heating in air above 400° C [2.11,2.13-2.15]. By about 650° C, sufficient oxygen has been lost for x to decrease to 6.5; at the same time, the orthorhombic distortion of the sample has gradually decreased until the structure appears to be tetragonal at temperature $> 650°C$, corresponding to x<6.5 [2.11]. On heating in different atmospheres, the transition may be displaced to higher or lower temperatures, depending on the partial pressure of oxygen: thus, in pure oxygen, it occurs near 700° C, but in an atmosphere of 2% oxygen, it occurs at about 620°C [2.11]. The critical factor in controlling the transition appears to be the composition x. Even though x is itself temperature and atmosphere dependent, under equilibrium conditions at high temperatures the transition appears always to occur at x=6.5.

In West's work stock samples of $YBa_2Cu_3O_x$ were prepared by solid state reaction of Y_2O_3, CuO and $BaCO_3$ in Au foil boats in electric muffle furnaces in air. Samples were heated at $700 - 800°C$ for a few hours to drive off CO_2, crushed and heated at $900 - 950°C$ for 12-24 hours to complete the reaction. The samples were then cooled slowly to 400° C, removed from the furnace and crushed to a fine pow-

der. Completeness of reaction was confirmed by x-ray powder diffraction with a Hagg Guinier camera using CuK_{α_1} radiation. For accurate d-spacing measurements, KCl was added as an internal standard and the films measured with a travelling microscope. The powder patterns were indexed and accurate lattice parameters obtained by least squares refinement of the complete powder pattern, for d-spacings down to $1.5\mathring{A}$.

In order to determine the oxygen content x of samples, West et al used thermogravimetry, based on the widely observed result that x=7.0 in samples heated to constant weight in pure oxygen at 400° C. Samples of $YBa_2Cu_3O_x$ with initially x=7.0 were heated in isothermal steps and graphs of x against temperature constructed. This was done for three gas atmospheres, oxygen, air and 5% oxygen, 95% nitrogen. The results are shown in Figure 2.2 and are in good agreement with those of some other thermogravimetry studies [2.13-2.15]. From these graphs, the equilibrium value of x could be determined for any temperature in the range covered. By using these calibration curves of temperature against composition, Figure 2.2, lattice parameters were obtained as a function of composition, Figure 2.3. From these, the following observations may be made. First, the lattice parameters are very similar for all three data sets and are essentially independent of atmosphere or annealing temperature. Second, the orthorhombic-tetragonal transition occurs at x=6.41 ±0.01, which is significantly lower than the high temperature value of 6.5. Third, the composition dependence of c shows a marked change in slope at x=6.55 ± 0.05. The anomalous c behaviour, Figure 2.3, which is reflected even more clearly in a similar anomaly in the
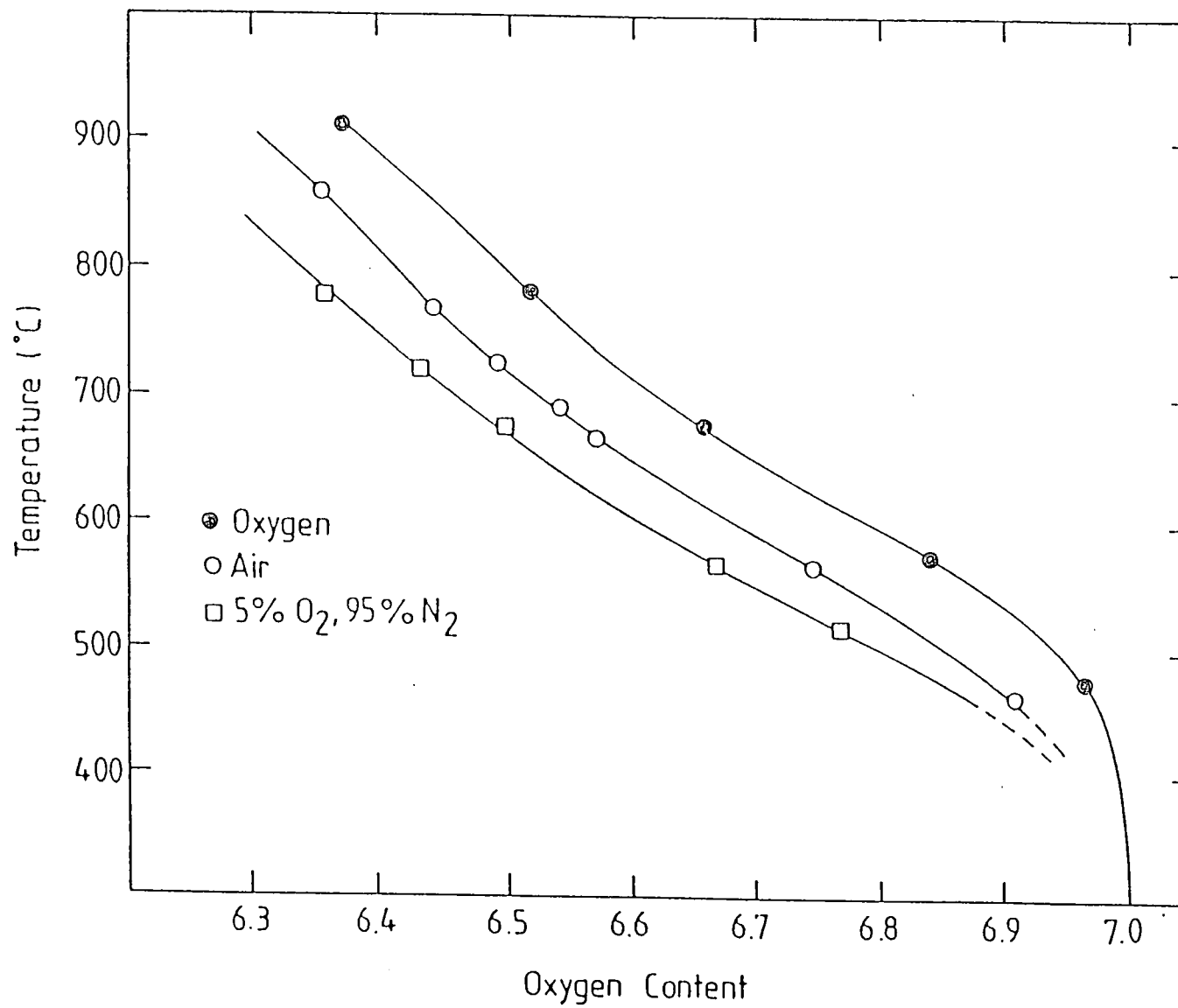
Figure 2.2   Variation of oxygen content with annealing temperature
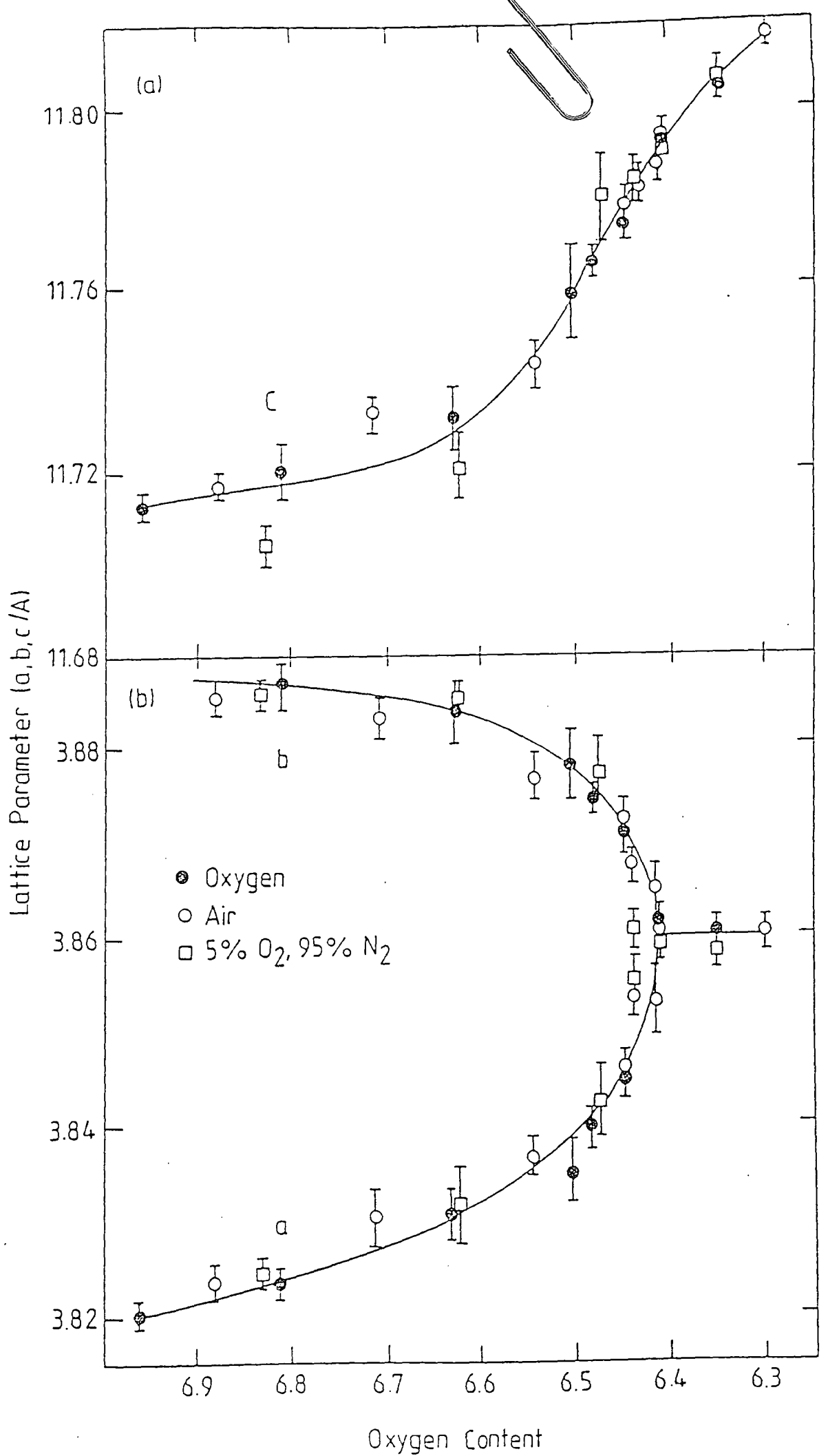
Figure 2.3 Variation of lattice parameters with oxygen content

unit cell volume, Figure 2.4, occurs over the approximate composition range 6.5 to 6.4 which again coincides with those compositions which transform to orthorhombic on quenching, with creation of O(4) vacancies. Thus, creation of O(4) vacancies in the (0,0,z) positions leads to a decrease in the net electrostatic attractive force in the c direction and consequently to an anomalous increase in c. This anomalous increase is superposed on a more gradual increase in c and cell volume with decreasing x, which may be accounted for by the gradual decrease in bonding forces with reduction of the sample. In the present work West's graphical data has been used to obtain the oxygen content of the various YBCO specimens examined from the measured lattice parameters.

In the case of the specimens considered so far, i.e 1A, the oxygen content determined from the a and b values are 6.9 and 6.9 respectively; the c value of 11.665 $\mathring{A}$ would yield an oxygen content of greater than 7.00. The unit cell volume (173.25 $(\mathring{A})^3$) would, according to Figure 2.4, also gives an oxygen content greater than 7.00. The oxygen content may also be estimated from data given in the paper by Specht et al [2.16]. These authors also examined the effect of oxygen pressure on the orthorhombic-tetragonal transition in the high-temperature superconductor $YBa_2Cu_3O_x$ by high-resolution x-ray diffraction measurements. They gave data relating the unit cell volume of the $YBa_2Cu_3O_x$ and the values of x which is reproduced here as Table 2.4. This Table has been used to estimate x from both the c dimension and the unit cell volume. The collected data for specimen 1A is given in Table 2.5 which shows that x is greater than 6.9.

19

Unit-cell volume ortho. $(\mathring{A}^3)$	x oxygen atoms	c/3 ortho. $(\mathring{A}^3)$
173.5(2)	6.97(2)	3.893(2)
174.6(2)	6.97(2)	3.906(2)
175.5(2)	6.97(2)	3.914(2)
176.0(2)	6.96(3)	3.921(2)
177.2(2)	6.95(2)	3.934(2)
178.4(2)	6.84(2)	3.949(2)
180.1(2)	6.71(2)	3.962(2)
181.4(2)	6.56(2)	3.978(2)

Table 2.4: Variation of unit cell volume with oxygen content

	Specimen 1A Cell Parameter	Oxygen Content West's et al	Oxygen Content Specht et al
a	3.822	6.9	-
b	3.886	6.9	-
c	11.665	>7.0	>6.97
c/3	3.888	-	-
Volume	173.25	>7.0	>6.97

Table 2.5: Estimates of oxygen content of specimen 1A derived from unit cell parameters.
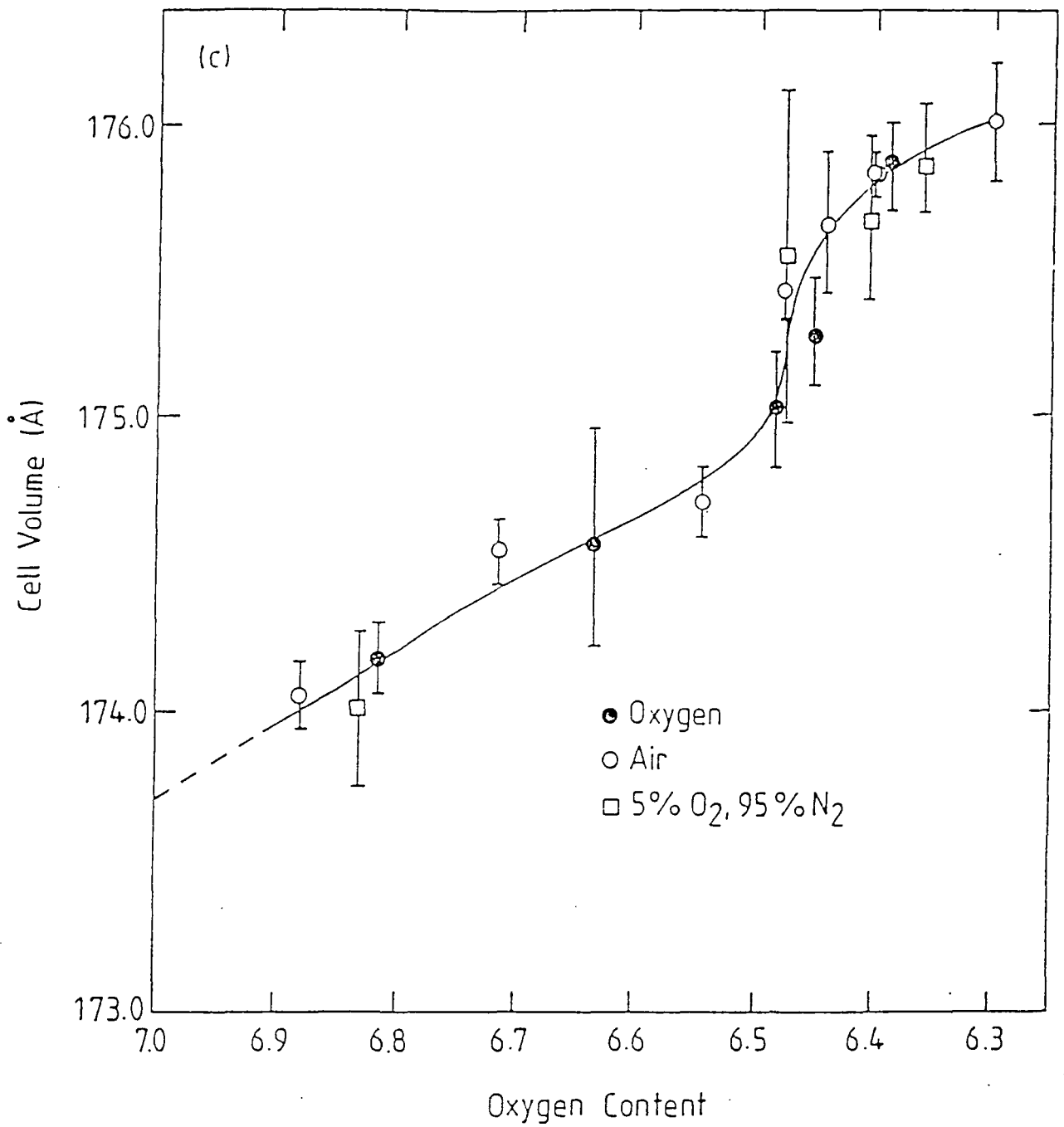
Figure 2.4 Variation of unit cell volume with oxygen content

2.1.4 XRD on other as received samples.

In a similar manner x-ray diffraction spectra were recorded photographically for a series of YBCO samples which had been obtained from various sources and had been made by different methods from different types and grades of starting material. These preparation methods are given, to the extent that they are known, in Table 2.6. A comparison of the numbers of lines seen in each spectrum (and the corresponding d-values) for five other samples is made in Table 2.7. The lattice parameter values and the estimates of oxygen content are given in Table 2.8. It is interesting to note, as will be discussed in detail in Chapter Three, that specimens 2A and 3A showed some superconducting behaviour. However specimen 4A, whose lattice parameters were very different from those of $YBa_2Cu_3O_7$, did not show any superconductvity.

2.1.5 The Effect of Annealing.

It is commonly held that after initial preparation samples of YBCO may degrade due to absorption of atmospheric water vapour which converts the oxide to a hydroxide. To overcome this samples are usually annealed in oxygen, often at 450°C, for several hours. It is thought that this decomposes any hydroxide and also restores the oxygen stoichiometry. The effect of annealing at various temperatures and partial pressures has been examined in detail by the authors to whom reference has been already been made [2.4, 2.16]. The annealing temperature must be kept below about 450°C in order to prevent loss of oxygen from samples of original com-

Specmin Reference	Starting Materials and Preparation Method
1A	Oxide route; spectroscopically pure BaO, Y_2O_3; small scale
2A	Peroxide route; commercial grade BaO_2, Y_2O_3, CuO; large scale production material
3A	Peroxide route; Y_2O_3 (99.99%), BaO_2 (GPR grade), CuO (Analor)
4A	Oxalate route (small scale milled oxalate); Y_2O_3, $Ba(COO)_2.H_2O$, CuO
5A and 6A	New synthetic methods to reduce impurity levels

Table 2.6 : Methods of preparation and starting materials used in manufacture of specimens examined. [In specimens 1A to 4A the iron content was about 700ppm as compared with less than 30ppm for 5A and 6A]

hkl	1A(Å)	2A(Å)	3A(Å)	4A(Å)	5A(Å)	6A(Å)
100	3.826	-	3.826	-	-	-
110	2.725	2.727	2.723	2.717	2.728	2.716
005	2.333	2.326	2.338	2.299	2.327	2.325
113	2.228	2.227	2.221	-	2.231	2.231
020	1.943	1.945	-	-	1.941	-
200	1.911	1.911	-	1.929	-	1.919
115	1.772	-	-	-	-	1.778
120	1.731	-	1.731	1.735	1.735	1.730
122	1.660	-	-	-	1.666	-
212	1.650	-	1.656	1.646	-	1.657
123	1.579	1.575	1.577	1.577	1.583	1.580
214	1.488	-	1.480	1.506	1.495	1.490
117	1.428	-	1.420	-	1.425	1.420
026	1.371	-	-	-	-	-
220	1.361	1.351	1.360	1.366	1.369	1.365

Table 2.7: Comparison of d-values of YBCO specimens made by different methods.

	2A(Å)	3A(Å)	4A(Å)
a	3.822	3.826	3.858
b	3.890	3.883	3.780
c	11.67	11.69	11.50
c/3	3.890	3.896	3.833
Unit cell volume	173.50	173.67	167.70
Oxygen content c/3(Specht)	6.97	6.97	<Limit
Volume (Specht)	6.97	6.97	Well below limit

Table 2.8: Unit cell characterization and oxygen content

for other YBCO specimens.

Lattic Parameter $\mathring{A}$	0 HRS		Specimen 2A 86 HRS at 450° C	Specimen 3A 60 HRS at 300° C	West's Value For $YBa_2Cu_3O_7$
	2A	3A			
a	3.822	3.826	3.812	3.836	3.8206
b	3.890	3.883	3.894	3.882	3.887
c	11.67	11.69	11.61	11.66	11.693
c/3	3.89	3.896	3.87	3.876	3.897
Volume $\mathring{A}^3$	173.50	173.67	172.33	173.63	173.69

Table 2.9: Effect of annealing in oxygen on lattice parameters and unit cell volume.

position $YBa_2Cu_3O_7$, which is the only superconducting phase. The present interest in annealing arose for two reasons. In the first place annealing was used to find out whether samples of nominal composition $YBa_2Cu_3O_7$ which did not superconduct could be restored to the superconducting phase by oxygen heat treatment. In the second place (see Chapter Three) it was hoped to increase the percentage of superconducting material present in those samples which did show some superconducting behaviour by similar oxygen heat treatment. Table 2.9 shows the changes in lattice parameter and unit cell volume observed after annealing in oxygen for two specimens, 2A and 3A. For comparison West's values for the composition $YBa_2Cu_3O_7$ are included. It appears that for both specimens the heat treatment has produced some reduction in the c parameter which causes a corresponding reduction in the unit cell volume. However the lattice parameters are still noticably different from those given by West for the superconducting phase $YBa_2Cu_3O_7$. In the powder photographic method used an accuracy of $\pm 0.008 \mathring{A}$ was attainable; the changes observed were well above the experimental error and thus can be used to establish major differences; more refined diffraction techniques would be required to follow the lattice parameter changes in more precise detail.

2.2 X-ray Fluorescence.

In x-ray diffraction (XRD) the diffraction pattern obtained by diffracting a monochromatic x-ray beam from a crystal lattice is obtained. The XRD spectrum is unique to a particular unit cell geometry and thus forms the basis of "analysis by

structure". In x-ray fluorescence on the other hand the material is a irradiated by high energy x-rays such that the characteristic radiation from each element in the sample is excited. Thus XRF provides a method for elemental analysis but does not by itself give any information on the type or structure of the unit cell. It is a well developed technique which can with care be used for either qualitative or quantitative analyses. The general principles of a fluorescence x-ray spectrometer are shown in Figure 2.5. The principles are discussed fully by Cullity [2.17]. It is usual to use a tungsten target operating at 100kV to provide the primary high energy x-ray beam. The separation of the fluorescence wavelengths is achieved by the use of a rotatable single crystal analyser using a fixed interplaner spacing d. The form of the XRF spectrum, illustrated in Figure 2.6, shows that each line can be attributed to a particular emission from a particular element. Here a conventional XRF spectrometer was used to analyse several of the YBCO specimens. The result from the instrument appears in the form of a table of counts per second (obtained over a given period of time, usually four seconds) at each 2θ value at which any line is observed over the range from $2\theta=10°$ to $2\theta=125°$. The elements are identified from the 2θ values by reference to wavelength tables. An example showing part of the recorded data is given in Table 2.10 which shows the comparative counting rates observed for the major lines and some impurities. The quantitative analysis is made using a standard reference sample. Here the reference standard was Igneous Rock whose composition was accurately known from chemical analysis. For a given element the intensity in counts per second is found for a given emission line. The intensity of the same emission line

Line	2θ	CPS
Y $K_\beta 2$	29.800	4213
Y $K_\beta 1$	30.20	48803
Y$K_\alpha 1$	34.00	130981
Y$K_\alpha 1(2)$	71.200	1339
Y$K_\alpha 2(2)$	71.600	896
Ba $K_\beta 2$	13.400	7894
Ba$K_\beta 1$	13.800	30547
Ba$K_\alpha 1$	15.600	120237
Ba$K_\beta 2(2)$	27.800	3266
Ba $K_\alpha 1$ (2)	31.400	11386
Ba$K_\alpha 2$	31.800	6462
Ba$L_\gamma 4$	93.800	361
Ba$L_\gamma 2$	97.200	976
Ba$L_\gamma 1$	104.000	3345
Cu$K_\beta 1$	58.600	18378
Cu$K_\alpha 1$	65.600	110405

Table 2.10 : Form of data obtained from XRF spectrometer (for

major constituents; counting period 4 seconds).

Impurity	1A	2A	4A	Accuracy
Fe	690	690	780	± 20 ppm
Sr	26	2950	50	± 5ppm
Zn	65	120	12	± 5ppm
Cr	5	5	10	± 2ppm
Rb	5	15	5	± 2ppm
Ga	5	30	5	± 2ppm
Mn	300	300	800	± 20 ppm

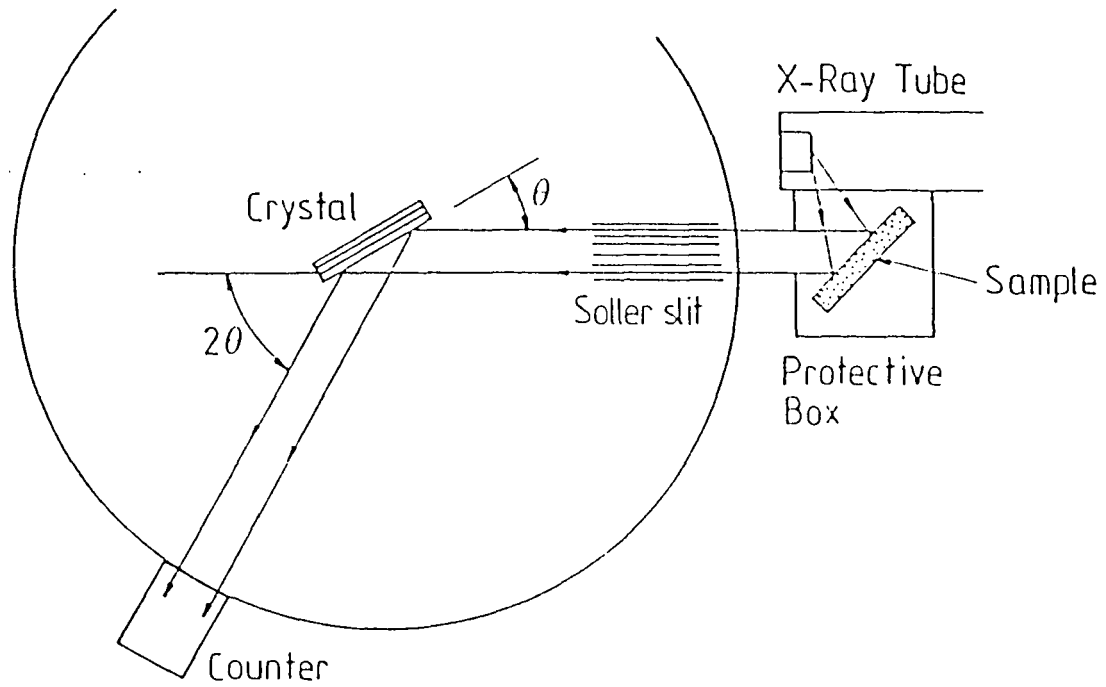Table 2.11 : XRF analysis of YBCO specimen; concentration given in ppm.

Figure 2.5   Essential parts of a fluorescent x-ray spectrometer, flat-crystal type.
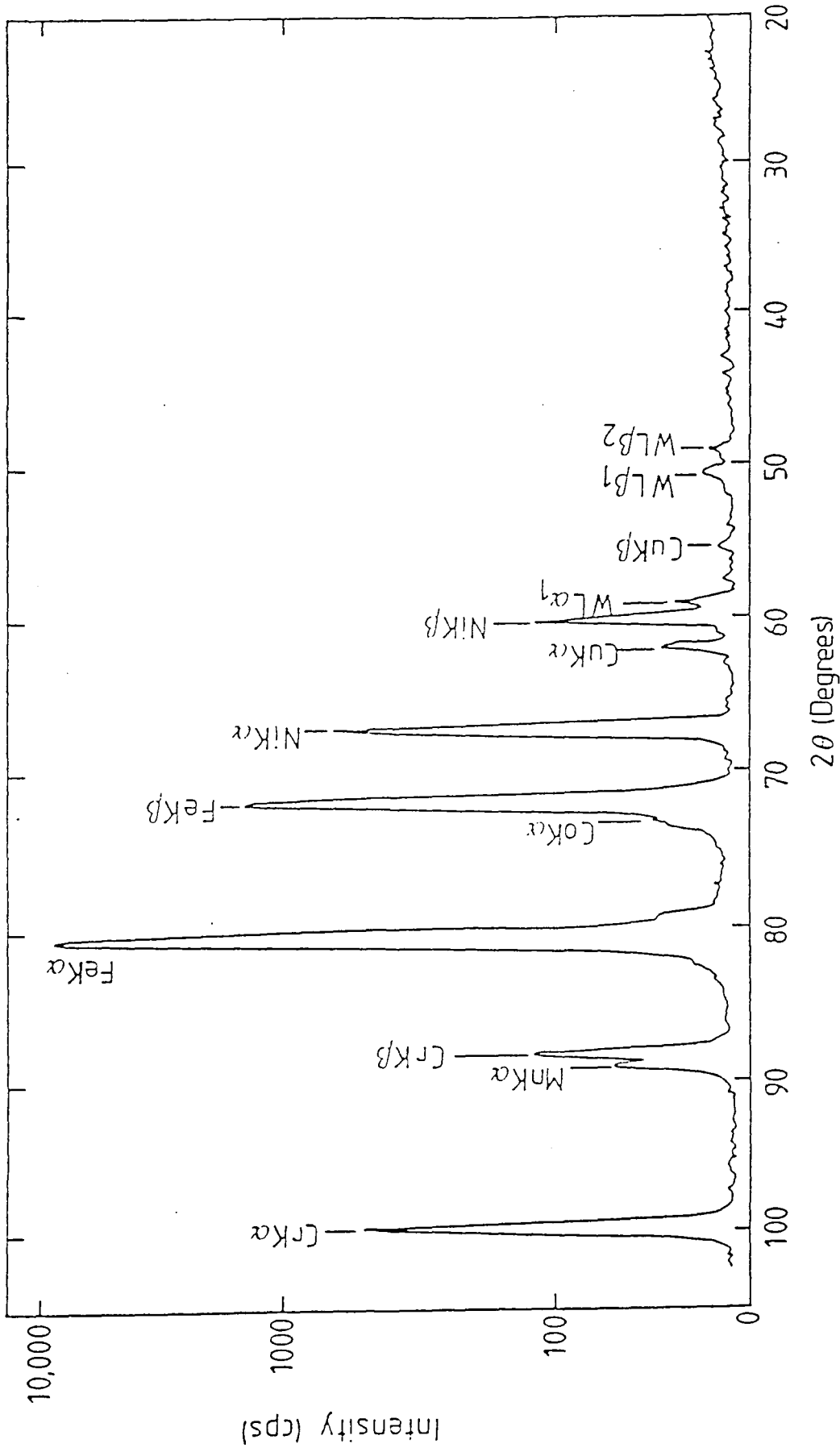
Figure 2.6 Fluorescent spectrum recording of stainless steel. Mica crystal analyzer used in transmission. Note logarithmic intensity scale.

from the standard is then observed and the concentration of the element is obtained by direct comparison of intensities. The major impurities found are listed in Table 2.11, which shows that the major impurities are iron, manganese and zinc present in amounts of about 700ppm, 500ppm and 100ppm respectively. It is also evident that 2A is abnormal in that there appears to be a very high strontium content which is not seen in the other samples. The spectrometer could not detect oxygen directly but was used specifically to detect iron group elements. The ferromagnetic elements are particularly important because if present the very large positive susceptibility distorts both the susceptibility and magnetization measurements making it very difficult to detect a small amount of diamagnetic behaviour. Here the XRF analysis shows that iron is present at about 780ppm level in all the samples; it is thought that the major source of iron contamination originates in the copper oxide. The XRF alone cannot distinguish whether the iron is present as an element or combined as a (ferromagnetic) compound. The XRF technique can also be used to determine the Y:Ba:Cu ratio but this involves correction of the intensities observed in the XRF spectrum for factors such as atomic number (which determines the emission wavelength), absorption and self fluorescence and these computer software packages were not available here.

2.3 Scanning Electron Microscopy (SEM):

2.3.1 General Principle:

A Cambridge Stereoscan S600 SEM was used to investigate the surface topogra-

phies of the samples of superconductor material. A schematic diagram of the SEM is shown in Figure 2.7. The SEM may be operated in several modes (e.g. secondary emission mode, energy dispersive analysis by x-rays (EDAX), electron beam induced current (EBIC) mode etc) by imaging the signals derived from different interactions which occur between the incident electron beam and the specimen [2.18]. The secondary emission and EDAX modes were used in the present investigation.

The basic principle of operation in this mode is that as the electron beam is scanned across the sample, secondary electrons are emitted from the specimen surface. The secondary electron coefficient depends critically on the composition and orientation of the area illuminated by the primary electron beam. Consequently by imaging the variations in secondary emission high contrast can be obtained. The secondary electron beam on the sample is synchronised to the output signal from the cathode ray tube with the same raster generator to avoid any time-lag in the image formation. In this way a micograph of the sample is produced on the screen. There is a problem, however, with an insulating sample, the surfaces of which become electrostatically charged by the electron beam. This induced field deflects the electron beam and so destroys the SEM image of the sample. In the present investigations special precautions were necessary with some samples.

The EDAX mode depends on a different principle. As the operating voltage of the SEM is 25 kV x-rays are produced by the interaction of the electron beam with the sample. Each element produces its own characteristic x-ray spectrum which
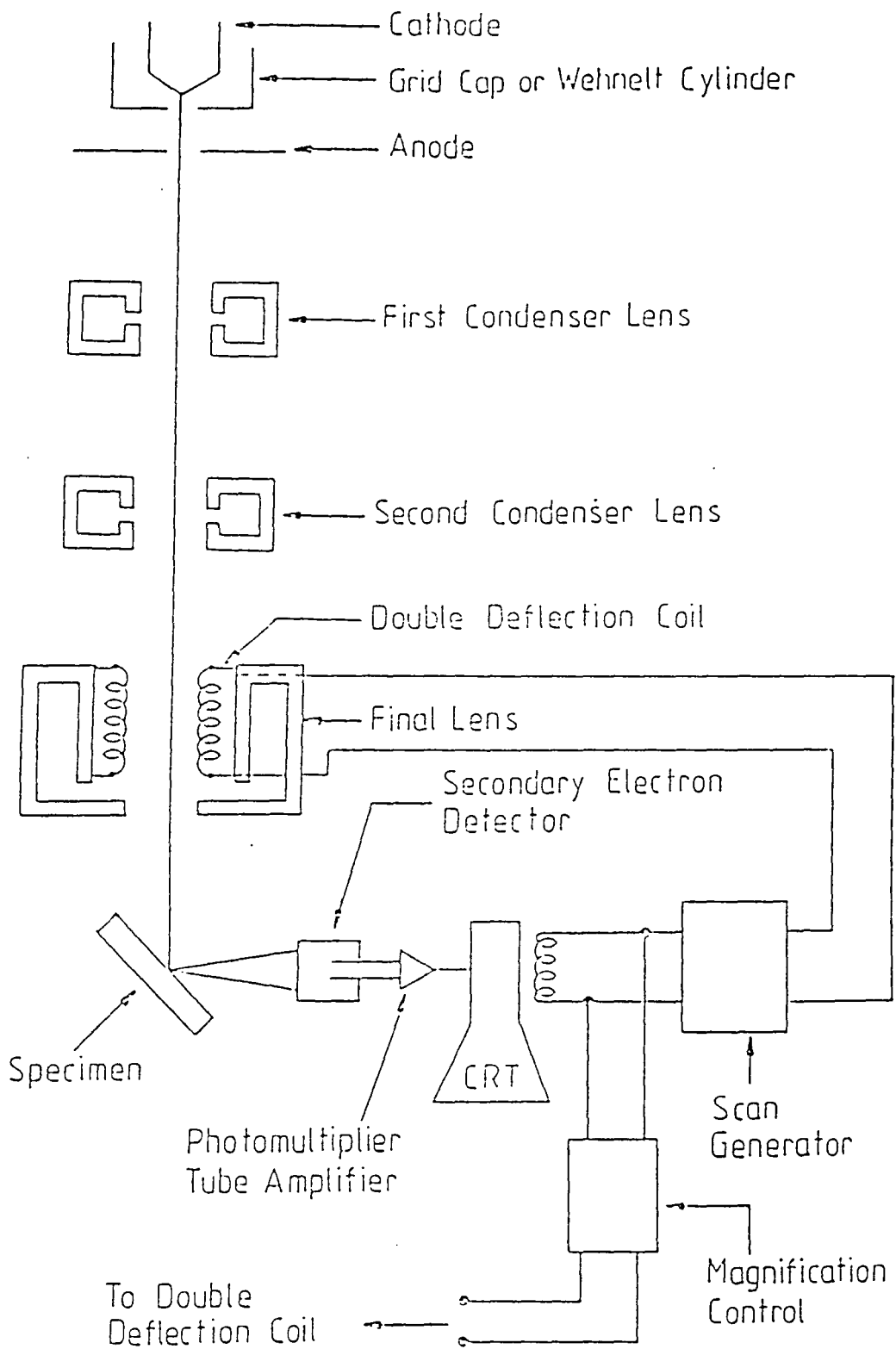
**Figure 2.7** General arrangement of SEM.

may be analysed to identify the element. The x-rays emitted from the surface of the sample pass through a thin beryllium window into a precooled Lithium drifted Silicon detector. This leads to the ejection of photo-electrons which give up most of their energy in the formation of electron-hole pairs. The reverse bias on the p-n junction in the detector forces the electron-hole pairs to form a charge pulse. This charge pulse is converted into a voltage pulse by a suitable charge sensitive pre-amplifier. The amplitude of the voltage pulse is proportional to the magnitude of the charge released by the photoelectron which in turn is proportional to the energy of the incident x-ray photons originating from the elements of the sample. Thus an energy spectrum of the x-rays can be built up and analysed in a multichannel analyser to identify the elements present in the sample. The resulting spectrum can be displayed on the screen or printed out to give a permanent record. The main advantage of EDAX is that, since the diameter of the electron beam used in the SEM is only about $1\mu m$, analysis of small volumes becomes possible.

2.3.2 SEM/EDAX Analysis of YBCO Powders.

The first SEM/EDAX analysis was undertaken on powders which were affixed to the specimen mount using silver paste. An example is shown in Figure 2.8 which refers to specimen 1A. It is evident that there is a large range of grain size and shape. The majority of particles have dimensions of 4μm, but a number are as large as 10μm while there are in addition smaller randomly distributed particles of size $< 1\mu$m. The particle shapes are irregular. However there are several larger particles which
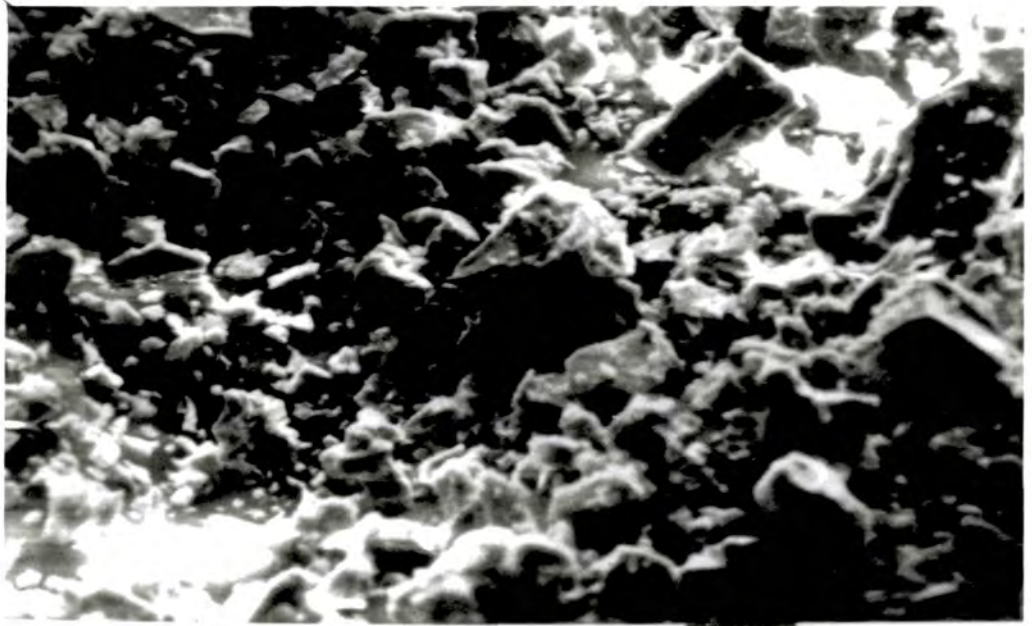
(a)
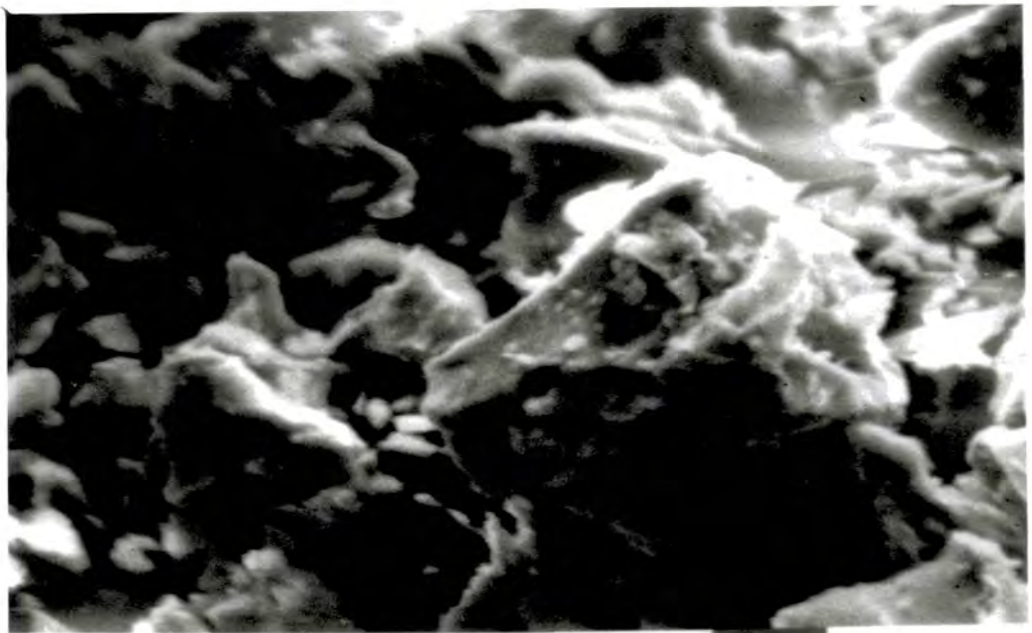
(b)

Figure 2.8: SEM micrographs 1A, powder.

show distinct crystallographic features and display flat surfaces with angled faces, suggesting small single crystals. Some of these large grains, e.g. in Figure 2.8(b), appear to be encrusted with smaller material of irregular shape. The smallest grains appear to be more nearly spherical, randomly distributed and of size less than about 1μ. Other specimens were examined in both powder and sintered pellet form. The comparative result for specimen 3A powder is shown in Figure 2.9 in which Figure 2.9(b) shows a higher magnification view of part of the area shown in Figure 2.9(a). In Figure 2.9 the general features are similar to those of the pure specimen 1A; there is again a range of grain size with a mean size about 5μ. After converting this powder to a sintered pellet (made by pressing at 150 atmospheres and sintering at $950°C$) it can be seen that there is a noticeable change in the microstructure. The micrographs given in Figure 2.10(a) and Figure 2.10(b) were obtained from different regions near the center of the pellet; the micrograph shown in Figure 2.10(c) is of a region near the edge of the pellet, taken at a higher magnification. Referring to Figure 2.10(a) and 2.10(b) it can be seen that the average grain size has increased to about 10 μm. Comparison with Figure 2.9 shows that a major difference is that the shape of many of the grains has changed. Whereas in the powder most grains were irregular in shape, in the pellet many are mainly square and some are packed into rows. Many of these individual square or rectangular grains are packed into rows in a regular manner with their edges in contact. Even in areas, e.g. Figure 2.10(b), where the alignment of the grains is not so marked there still appears to be good grain-to-grain contact. In places the square grains are arranged in very well ordered rows suggesting
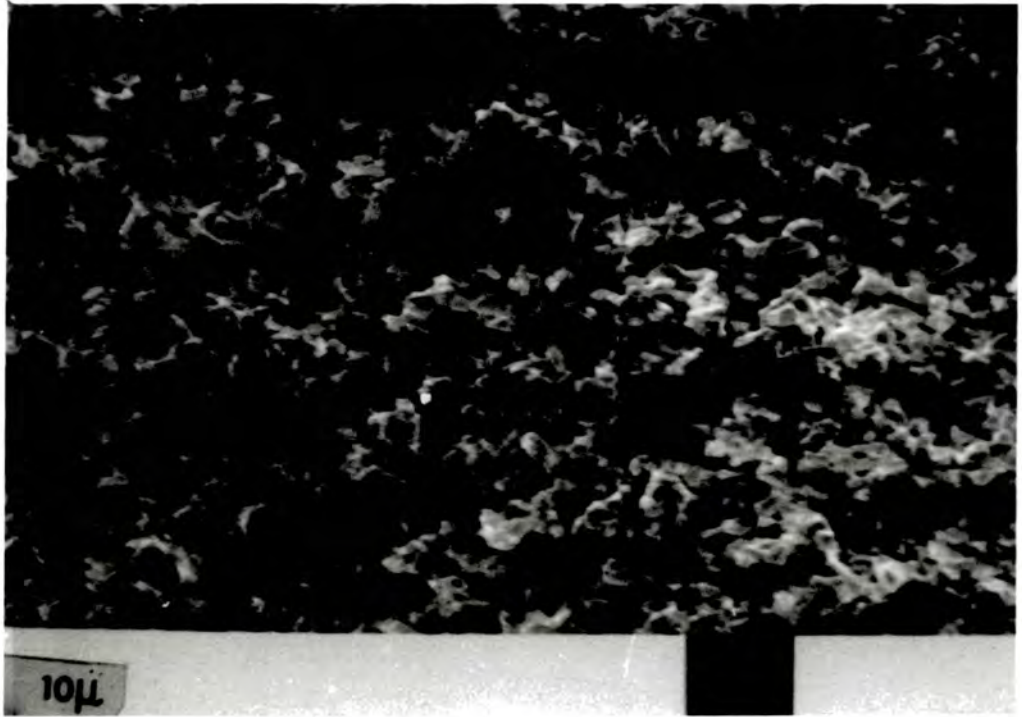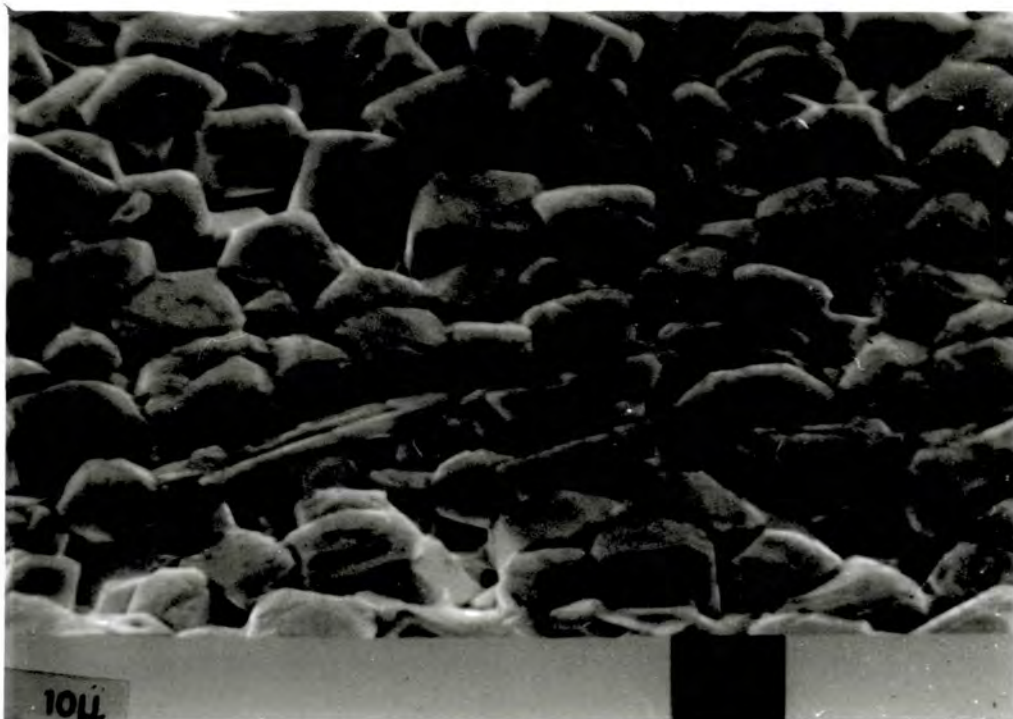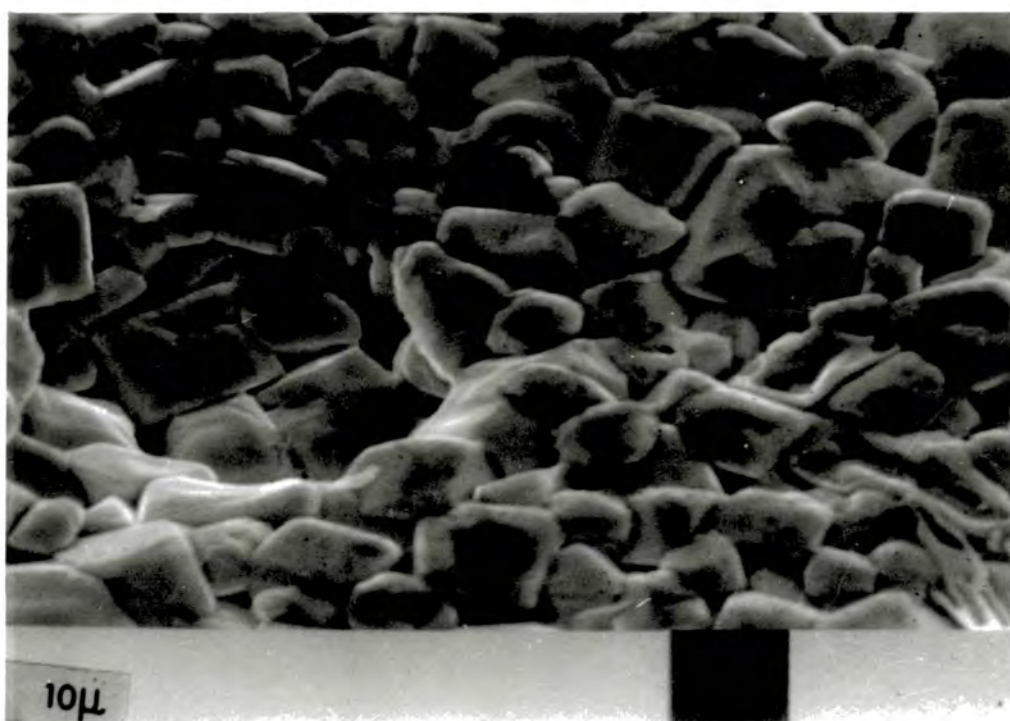
(a)
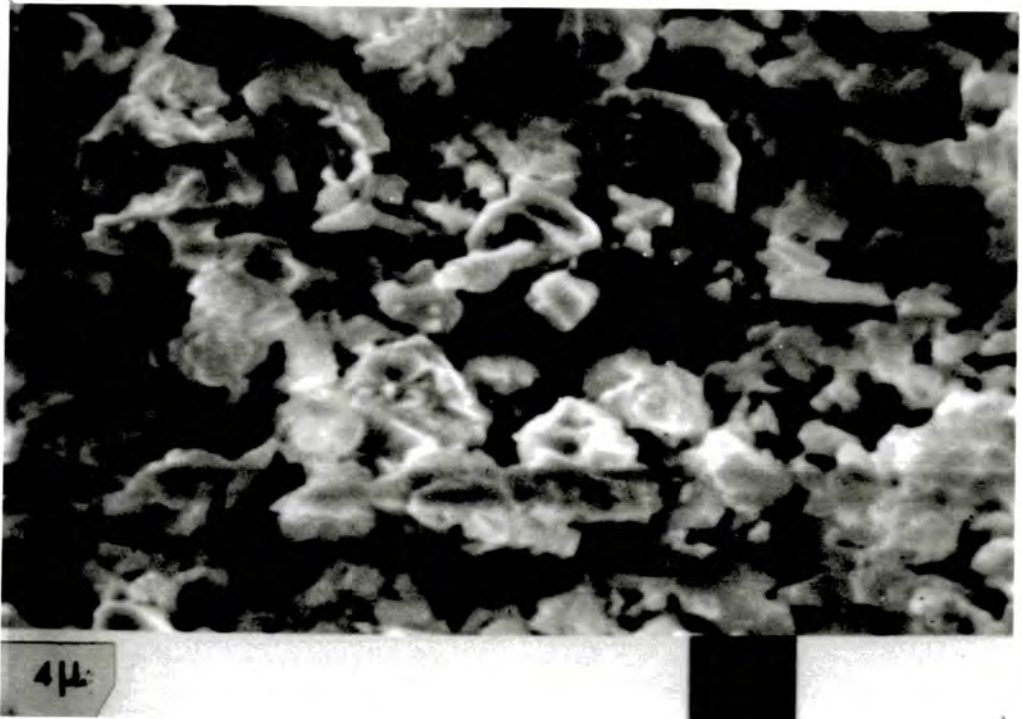
(b)

Figure 2.9: SEM micrographs 3A, powder.

(a)

(b)

Figure 2.10: SEM micrographs of 3A, sintered pellet.

4µ

(c)

Figure 2.10: SEM micrographs of 3A, sintered pellet.

some degree of alignment of orientation. There are in addition many grains which are smaller (up to 5μm) and which are rounded in shape and interspersed at random among the larger square grains. Referring now to Figure 2.10(c), which was taken near the edge of the pellet, it is clear that the microstructure is quite different from that near the center of the pellet. There is a mixture of a few well spaced large grains and background of much smaller particles. The large grains do exhibit crystallographic features and their size is about 6 to 8μm; some appear to have hexagonal symmetry. The small grains show size variations from about 1μm to less than 0.25μm; the larger of these are nearly square whereas the smallest ones seem rounded. Comparing this region of the sintered 3A pellet with the micrograph of 1A powder taken at the same magnification (Figure 2.8) shows that in the former the grains have much cleaner faces suggesting some degree of melting and grain growth which is consistent with the sintering treatment.

For specimen 5A two typical micrographs are shown in Figure 2.11(a) and 2.11(b);these correspond to two different areas of the sintered pellet, (a) being near the center of the pellet and (b) being near the edge. At the center the grain size is small, the largest only being about 4μm with many in the range 1 to 2μm; the grains appear to be rounded and loosely packed with no evidence for melting at the grain boundary. Near the edge (Figure 2.11(b)) the grain structure is indistinct; there appears to be a fibre like structure superimposed on a fused matrix. As regards specimen 7A, Figure 2.12(a) shows two micrographs taken at different magnification at a region near the center of the sintered pellet; the grains are well formed and fairly
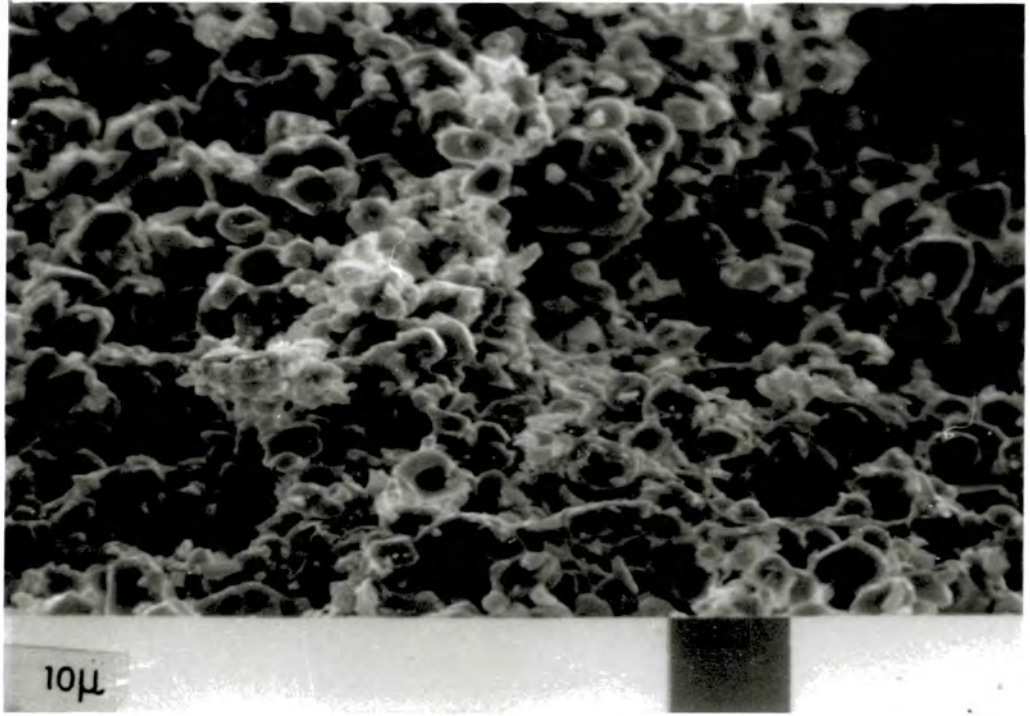
(a)
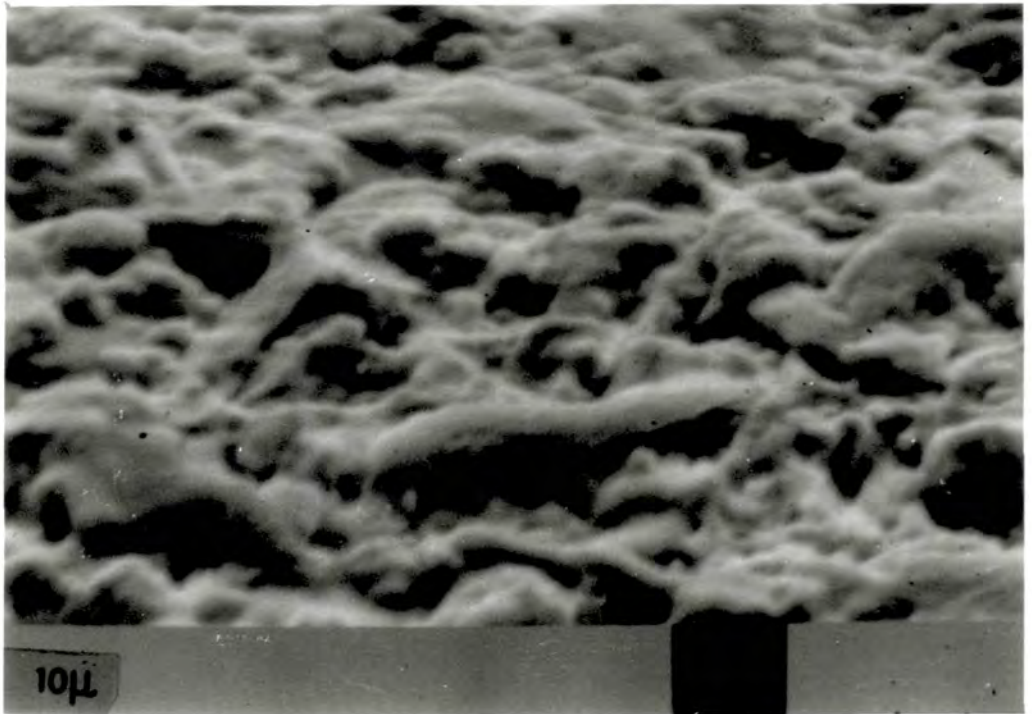
(b)

Figure 2.11: SEM micrographs 5A, sintered pellet.

10μ

4μ
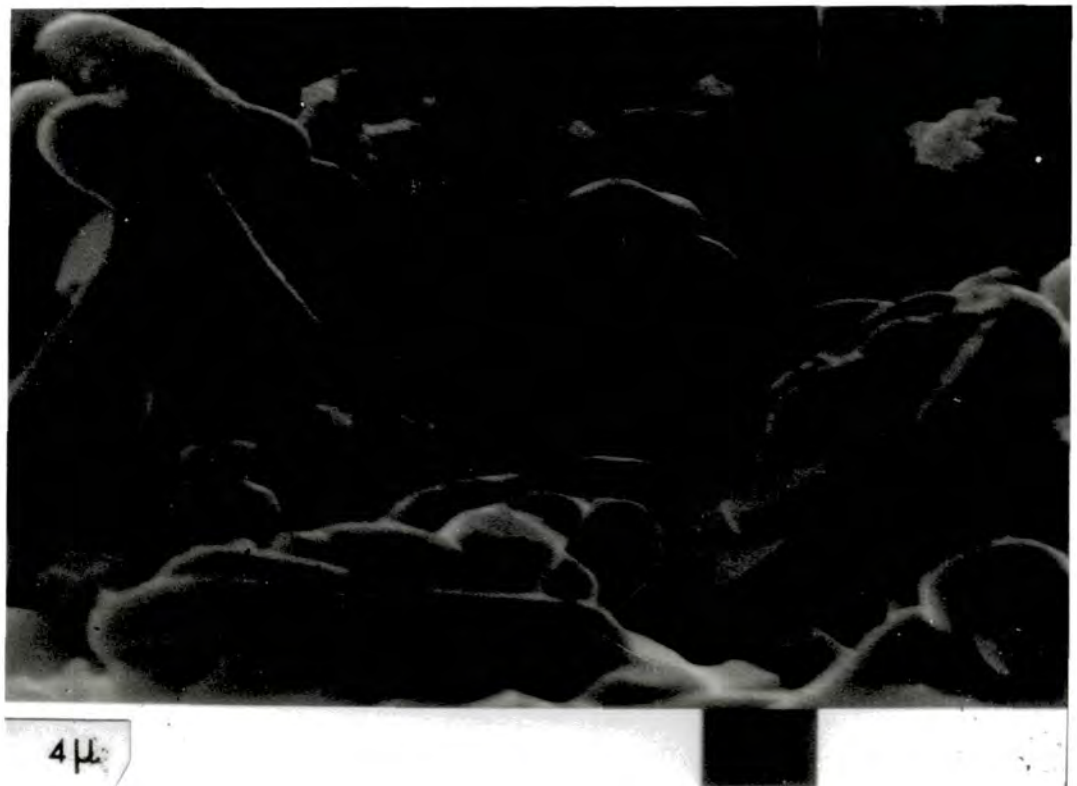
Figure 2.12 (a): SEM micrographs 7A, sintered pellet.
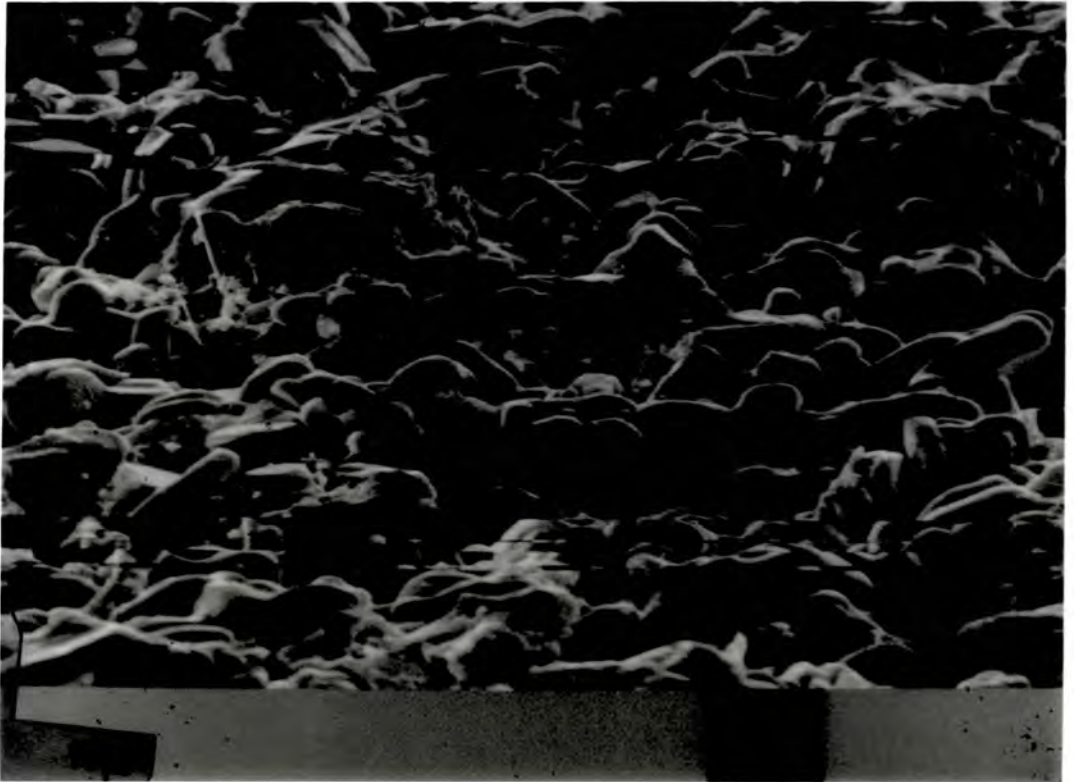
Figure 2.12 (b): SEM micrographs 7A, sintered pellet.

uniform in shape and size with a mean grain size of 10μm. At a region near to the edge, Figure 2.12(b), the average grain size appears to be a little smaller and there are also a number of very small features not so apparent in Figure 2.12(a).

In considering the EDAX data reservations must be made as regards the extent to which directly observed elemental intensities may be used to estimate stoichiometric ratios. The observed intensities must be corrected to allow for the variation of emission wavelength with atomic number, preferential absorption and self-fluorescence (in a similar manner to XRF quantitative analysis). These corrections are particularly important with powders. Computer packages for making these correction can be obtained but were not available on the equipment used here.

It is however valid to seek to obtain comparative variations in the levels of individual elements at different positions on the specimen either by (a) making a series of large area scans under identical instrumental conditions or (b) using the spot mode of operation (which gives a beam size of $1\mu m$) to isolate and analyse individual grains. Here both approaches have been adopted, concentrating on the intensity variation in the $Y(L_\alpha)$, $Ba(L_\alpha)$ and $Cu(K_\alpha)$ lines respectively. Two examples of EDAX spectra of superconducting powders are given in Figures 2.13 and 2.14 from which the differences in corresponding peak height are evident. The quantitative results for specimen 1A (powder)are given in Table 2.12. Large area $(100\mu m \times 57\mu m)$ analyses were made at twelve different positions, Table 2.12 (a); these show that the Ba level is nearly constant, that the Cu level varies (with one extreme exception) by

Position	Intensity (mm)		
	Y(L)	Ba(L)	Cu(K)
1	15	178	192
2	24	192	169
3	192	115	56
4	23	191	165
5	52	189	128
6	138	191	107
7	71	165	190
8	15	190	159
9	95	190	116
10	20	120	190
11	38	166	192
12	20	121	189

Table 2.12 (a) : EDAX Large area analysis.

Position	Intensity (mm)			Grain size (μm)
	Y(L)	Ba(L)	Cu(K)	
Area (a)				
13	12	192	106	4
14	61	191	79	4
15	20	192	94	4
Area (b)				
16	60	191	114	10
17	57	192	135	10
Area (c)				
18	42	192	78	10
19	76	192	113	10
20	118	192	96	> 10
21	23	191	189	> 10

Table 2.12 (b) : EDAX Individual grain analysis

Table 2.12 : EDAX analysis of YBCO powders; specimen 1A
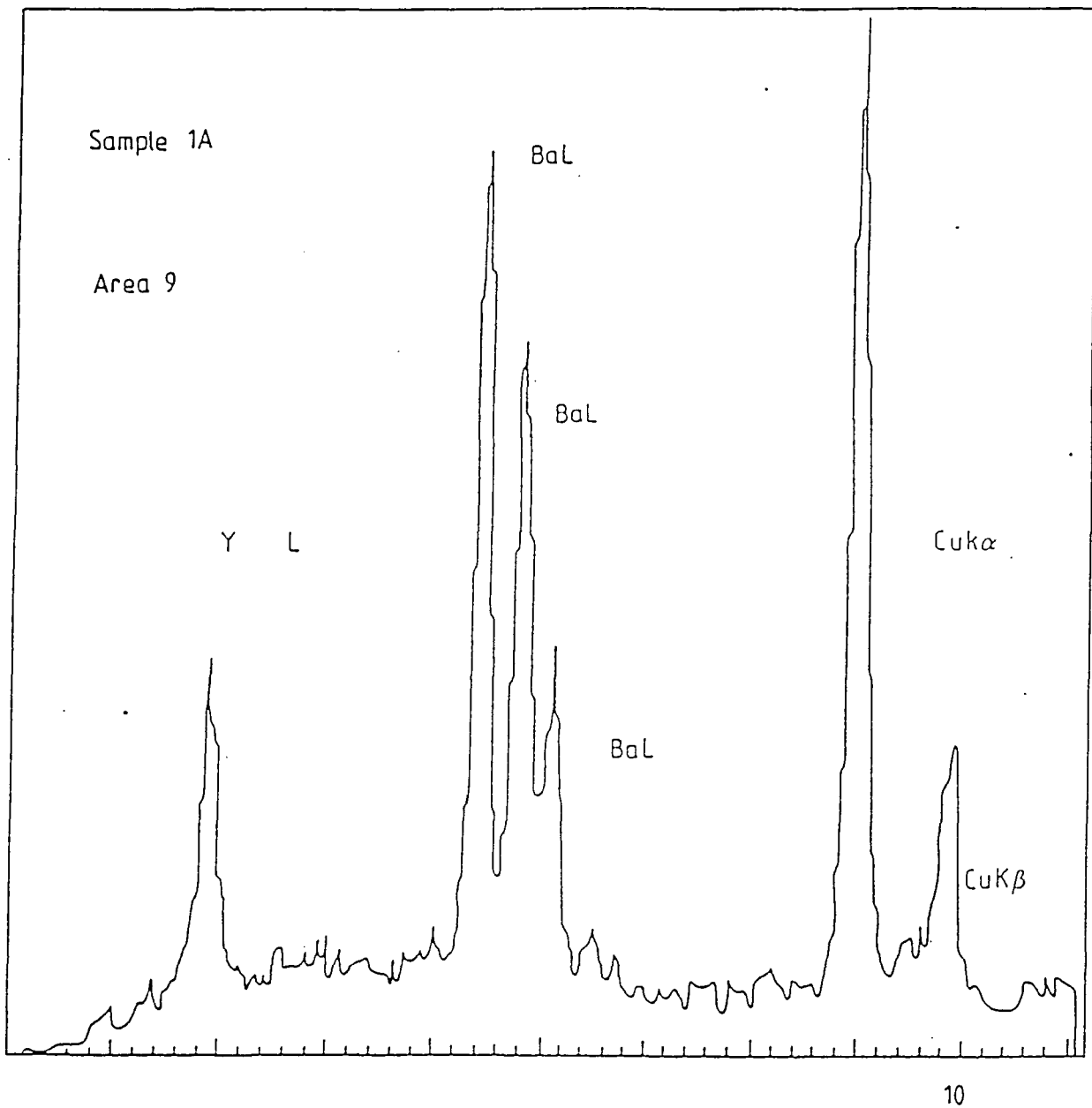
Figure 2.13: EDAX spectrum; specimen 1A, area 9.
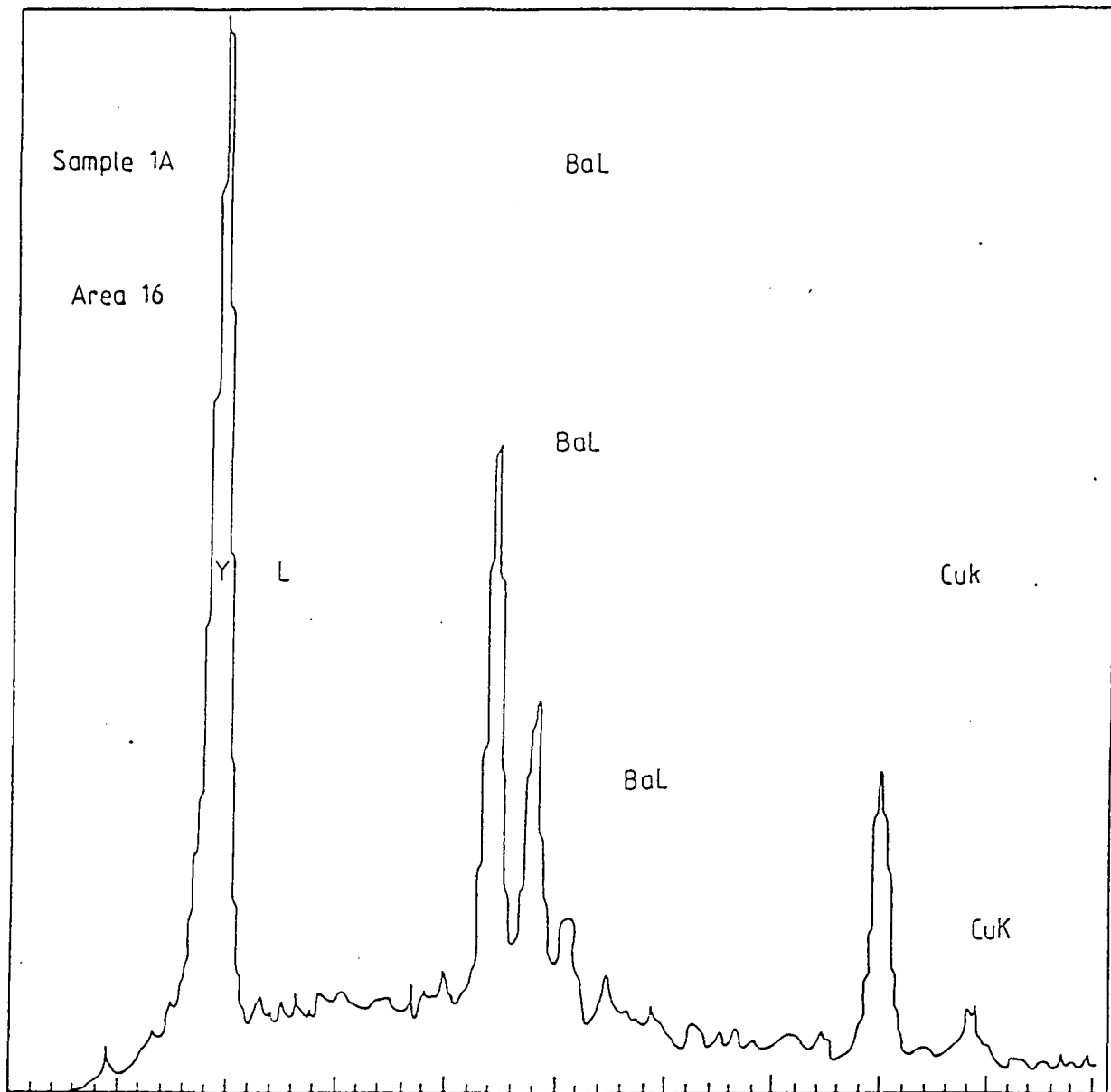
Figure 2.14: EDAX spectrum; specimen 1A, area 16.

about 40% and that the Y content is the most variable, changing by factors of up to eight times. The corresponding individual grain analyses, Table 2.12 (b), show the same trends though not quite to as great an extent. Nine individual grains, three having a size of $4\mu m$, four of $10\mu m$ and two $> 10\mu m$, were examined. The Ba intensity was constant to within 1%; the Cu intensity showed 20% variation over a selection of $4\mu m$ and $10\mu m$ grains, with wider discrepancies for some grains of larger size ($> 10\mu m$). Again the Y level showed most variation, changing by factors of about five between different grains. This evidence suggested that there were considerable differences in the Y:Ba:Cu stoichiometric ratios between different grains though it is not possible to express these differences quantitively in terms of departures from the ideal 1:2:3 ratio.

Two other YBCO powder specimens, 3A and 4A were examined in a similar way (3A showed superconductivity at 86 K whereas 4A did not). The EDAX results are given in Tables 2.13 and 2.14 which include both large area and single grain analyses.

Comparison of Table 2.13 (specimen 3A) with Table 2.12 (specimen 1A) shows that the Ba level is remarkably constant averaging 190 mm in each case and the levels of both the Cu and Y signals are very similar for each material. Similar comments apply to the comparison both of Table 2.14 (4A) with Table 2.12 (1A) and of Table 2.13 (3A) with Table 2.14 (4A). The main point which emerges from the EDAX studies is that there must be quite large differences in the stoichiometric ratio of Y:Ba:Cu between different grains in each of the materials examined. As discussed in

Position	Intensity (mm)			Grain size (μm)
	Y(L)	Ba(L)	Cu(K)	
Large area analysis				
1	93	191	125	
2	73	192	125	
3	52	192	135	
4	37	192	172	
5	86	191	115	
Individual grain analysis				
6	24	191	145	2
7	24	191	120	4
8	58	190	133	4
9	34	192	131	10

Table 2.13 : EDAX analysis of YBCO powder 3A.

Position	Intensity (mm)		
	Y(L)	Ba(L)	Cu(K)
1	53	192	147
2	35	190	175
3	71	192	189
4	51	186	191
5	27	191	130
6	128	191	114
7	26	189	191
8	60	192	130
9	41	192	152

Table 2.14 : EDAX analysis of YBCO powder 4A; large area

($100\mu m \times 57\mu m$) averages at different positions.

Chapter Three it has been concluded that even in the best sample less than 10% of the material is superconducting. The EDAX data supports this conclusion particularly if account is taken mainly of the individual grain analysis, which are the most reliable from the EDAX point of view.

Similar studies were made on some solid pellets. These had been made from the powders 3A and 5A by pressing at 150 atmospheres and sintering at $950°C$ for four hours. The collected data for individual grains of size varying from about 2μm to $> 10\mu$m is given in Tables 2.15 and 2.16. Here also the Ba content is constant to within 1%, the Cu content appears to be more constant than was observed in the corresponding powder and varies only by about 15%, and the Y content also seems to be less variable.

No	Intensity (mm)			Grain size (μm)
	Y(L)	Ba(L)	Cu(K)	
Circular grains				
1	75	192	92	10
2	85	192	106	10
3	82	191	104	10
4	67	190	135	10
5	100	192	116	10
Rectangular grains				
6	82	192	166	10
7	60	192	132	10
8	71	191	110	10
9	103	191	110	10
10	128	191	83	10

Table 2.15 : EDAX analysis of YBCO pellet; specimen 3A.

No	Intensity (mm)			Grain size (μm)
	Y(L)	Ba(L)	Cu(K)	
Circular grains				
1	192	149	170	10
2	192	104	72	10
3	105	190	145	10
4	112	192	123	10
5	65	191	147	>10
6	55	105	190	>10
7	120	193	180	>10
Rectangular grains				
8	97	191	102	<10
9	107	192	177	<10
10	123	192	114	<10
11	143	192	116	< 10
12	127	190	123	< 10
13	95	192	130	<10
14	95	192	130	<10

Table 2.16 : EDAX analysis of YBCO pellet; specimen 5A.

REFERENCES

2.1. W.I.F.David, P.P.Edwards, M.R.Harrison, R.Jones and C.C.Wilson, Nature, 331, 245, (1988).

2.2. T.Nishino, M.Kikuchi, and J.Kanamori. Solid State Comm. 68, 455, (1988)

2.3. R.M.Macfarlane, H.J.Rosen, E.M.Engler, R.D.Jacowitz and V.Y.Lee, Phys. Rev.█ 38B, 284, (1988).

2.4. C.Namgung, A.R.West, J.T.S.Irvine and J.H.Binks. Superconductor Science and Techonlogy. 1, 169, (1988).

2.5. R.Beyers, G.Lim, E.M.Engler, R.J.Savoy, T.M.Shaw, T.R.Dinger, W.J. Gallagher and R.L.Sandstrom. Appl. Phys. Lett. 50, 1918, (1987).

2.6. A.Reller, J.G.Bednorz and K.A.Muller. ZPhys. B-Condensed Matter. 67, 285, (1987).

2.7. R.J.Cava, B.Batlogg, R.B.van Dover, D.W.Murphy, S.Sunshine, T.Siegrist, J.P.Remeika E.A.Rietman, S.Zahurak and G.P.Espinosa. Phys. Rev. Lett. 58, 1676, (1987).

2.8. Binod Kumar, J.D.Wolf, S.R.Smith. J. Mate. Scin. Lett. 7, 149, (1988).

2.9. D.H.A.Blank, J.Flokstra, G.J.Gerritsma, L.J.M. Van De Klundert and G.J.M.Velders.█ Physica 145B, 222, (1987).

2.10. P.P.Freitas and T.S.Plaskett. Phys. Rev. B36, 5723, (1987).

2.11. J.D.Jorgensen, M.A.Beno, D.G.Hinks, L.Soderholm, K.J.Volin, C.U.Segre, K.Zhang█

and M.S.Kleefisch. Phys. Rev. B36, 3608, (1987).

2.12. R.Kanno, Y.Takeda, M.Hasegawa, O.Yamamoto, M.Takano, Y.Ikeda and Y.Bando
Mat. Res. Bull. 22, 1525, (1987).

2.13. J.T.S.Irvine, J.H.Binks and A.R.West. Proc. Europ. Workshop on high T_c
superconductors and potential applications 297, (1987).

2.14. P.Strobel, J.J.Capponi, C.Chaillout, M.Marezio and J.L.Tholence. Nature, 327,
306, (1987).

2.15. P.K.Gallagher, H.M.O'Bryan, S.A.Sunshine and D.W.Murphy. Mat. Res. Bull.
22, 995, (1987).

2.16. E.D.Specht, C.J.Sparks, A.G.Dhere, J.Brynestad, O.B.Cavin, D.M.Kroeger and
H.A.Oye, Phys. Rev. B37, 7426, (1988).

2.17. B.D.Cullity "Elements of X-ray Diffraction" Addison-Wesley Publishing Company, Inc. U.S.A 3rd Ed. (1967).

2.18. J.I.Goldstein (ed) and H.Yokowitz (ed), Practical Scanning Electron Microscopy,
Plenum Press (1975).

CHAPTER THREE

INDUCTANCE-PROBE TECHNIQUES; MEASUREMENT

OF T_c AND SUPERCONDUCTING PERCENTAGE

3.1 Construction and Operation of Coil.

At the superconducting transition temperature magnetic flux is expelled from the specimen according to the Meissner effect [3.1]. As a result of this, if a coil of wire is wound around a superconductor the inductance of the coil should fall dramatically at the critical transition temperature (T_c), assuming that the coil is completely filled with the superconductor. For the YBCO specimens examined the critical temperature (T_c) was expected to be near 86 K [3.2]. Consequently it was sufficient to provide cryogenic facilities which enabled temperatures down to about that of liquid nitrogen (77 K) to be obtained. A piece of insulator (Tufnol) was turned down to the shape shown in Figure (3.1); the coil was formed from three thousand turns of 48 gauge copper wire wrapped around the insulator. Enough powder was pressed lightly into the central region C of the holder to ensure that the coil was completely filled, i.e the powder occupied the whole space between levels A and B . The apparatus used for low temperature measurement is shown in Figure (3.2). The stainless steel cryostat used for measurements at temperatures in the range between 293 K and 80K had three chambers: (a) the outermost chamber, (b) the mid-chamber, (c)the innermost chamber. The mid-chamber was a reservoir for liquid nitrogen. The specimen was

Thermocouple
(Cu/constantan)

Insulator

Level A

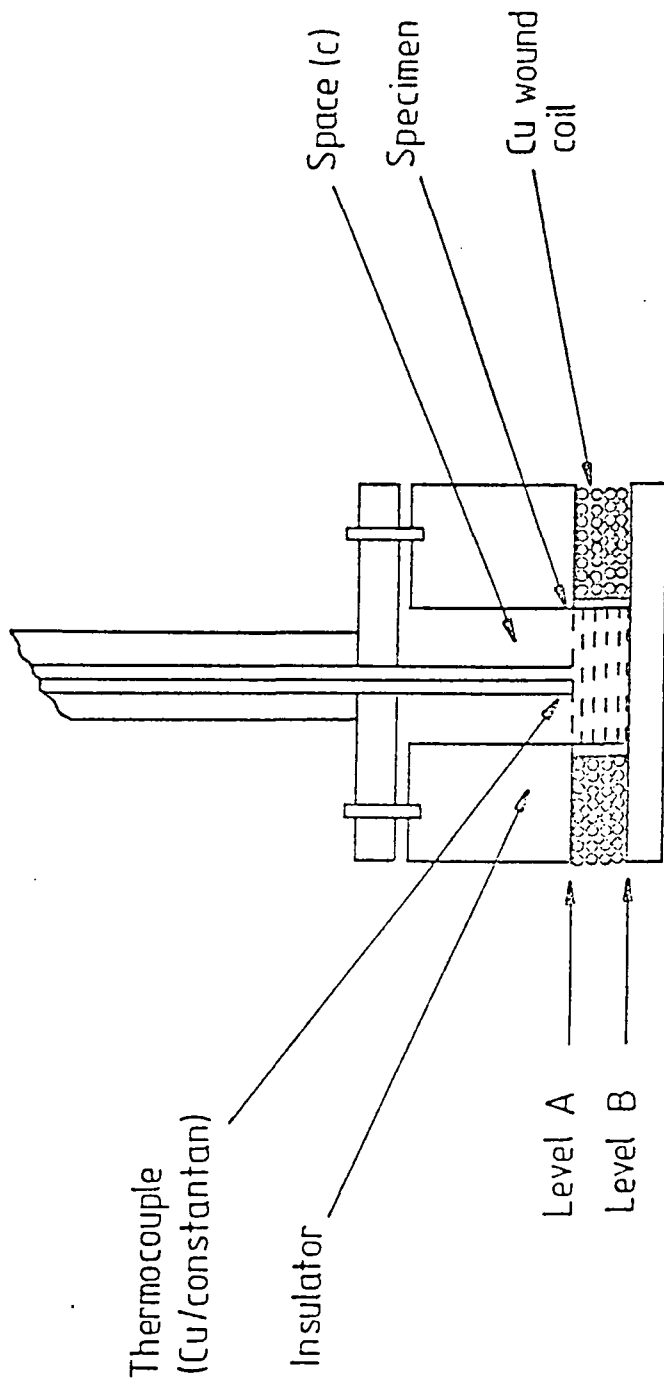Level B

Space (c)

Specimen

Cu wound
coil

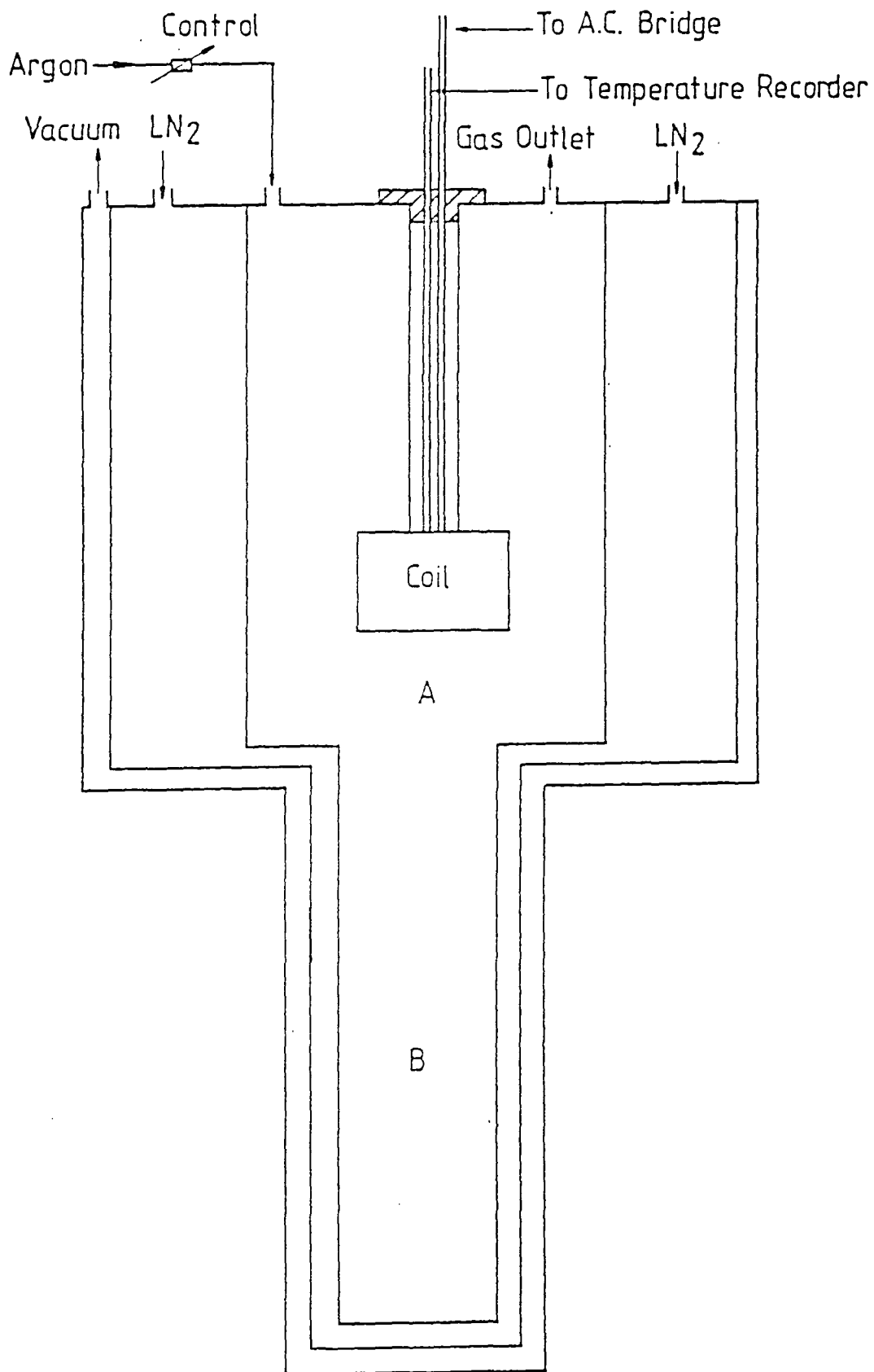Figure 3.1: Construction of inductance probe.

Figure 3.2: Cryostat arrangements for L-T measurements (293K to 77K)

suspended in the innermost chamber and was held in place by a tube of stainless steel which also acted as a heat insulator between the low temperature specimen and the room temperature cryostat head . A Cu/constantan thermocouple, mounted near the specimen and connected to a temperature recorder (a Type 207 Digital Indicator), gave a direct temperature reading of the specimen; (note that the thermocouple is in contact with the powder so that there will be no difference between the temperature recorded and that of the powder). A small volume of liquid nitrogen was placed down the innermost chamber. The remainder of the inner chamber was filled with dry argon gas at 740 mm of Hg pressure. With this procedure it was possible to obtain temperatures from 80 K to 293 K with an accuracy $\pm 1K$. The system was very stable, especially if measurements were made during the warming up period; it was necessary to run the system for about five hours to warm the specimen from 80 K to 293 K. The top plate, provided with four thin metallic electrodes isolated from each other, was designed to suit the experiment. The specimen, which was suspended inside the inner metallic chamber, and the cryostat were properly earthed to avoid any unwanted interference from electrical sources external to the cryostat. The inductance measurements were taken by using a Marconi Bridge (TF 1313A); in the initial experiments a frequency of 10 KHz was used, the standard operating frequency of the bridge.

3.2 Calibration of the system

In order to be sure that the system was working properly measurements were

first made of inductance versus temperature for the empty coil. This result is shown in Figure (3.3). As expected, no sudden drop in the inductance was observed at 86K. Between 293K and 77K the inductance falls steadily but only from 147.50mH to 147.10mH, a small decrease which is attributable to the small contraction of the coil on cooling. Secondly, a similar experiment was carried out with a different coil filled with a non-superconducting powder. For this purpose pure aluminium oxide, (Al_2O_3), was chosen. Figure (3.4) gives the inductance versus temperature variation and shows that only a very slight fall in the inductance was observed over the whole temperature range; again there was no sudden change at 86 K, showing as expected that there was no change in the magnetic properties of the (Al_2O_3) on passing through 86K.

3.3 Transition Temperature Data .

The observation [3.2,3.3], of transition temperatures (T_c) greater than 80K in the superconductor $YBa_2Cu_3O_{7-x}$ was probably one of the greatest discoveries in science for practical application in industry. Several experiments have focused on measuring the characteristic superconducting behaviour of this compound [3.4-3.10]. An example of an inductance temperature curve obtained here is given in Figure (3.5) which refers to a high purity YBCO specimen made at Durham. By comparison with the behaviour of the coil filled with non-superconducting material, (Figure (3.4)), the new feature is the sudden drop in the inductance at (T_c). The value for (T_c) is 90 K and this could easily be measured to ±1 K. The width of the transition is
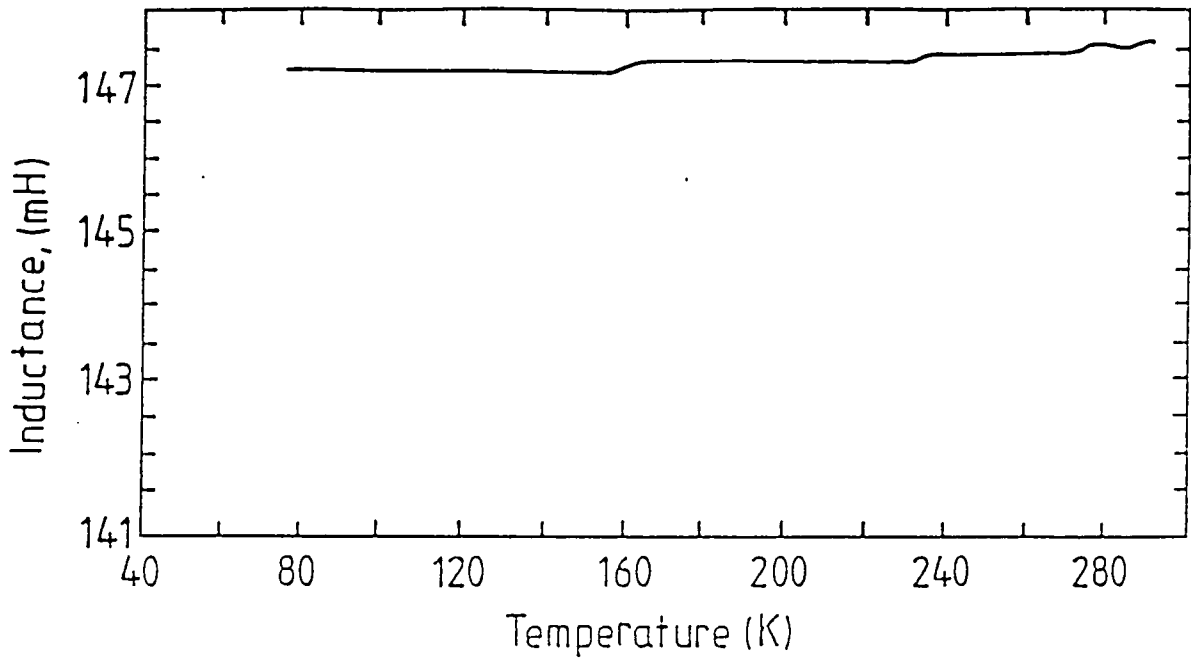
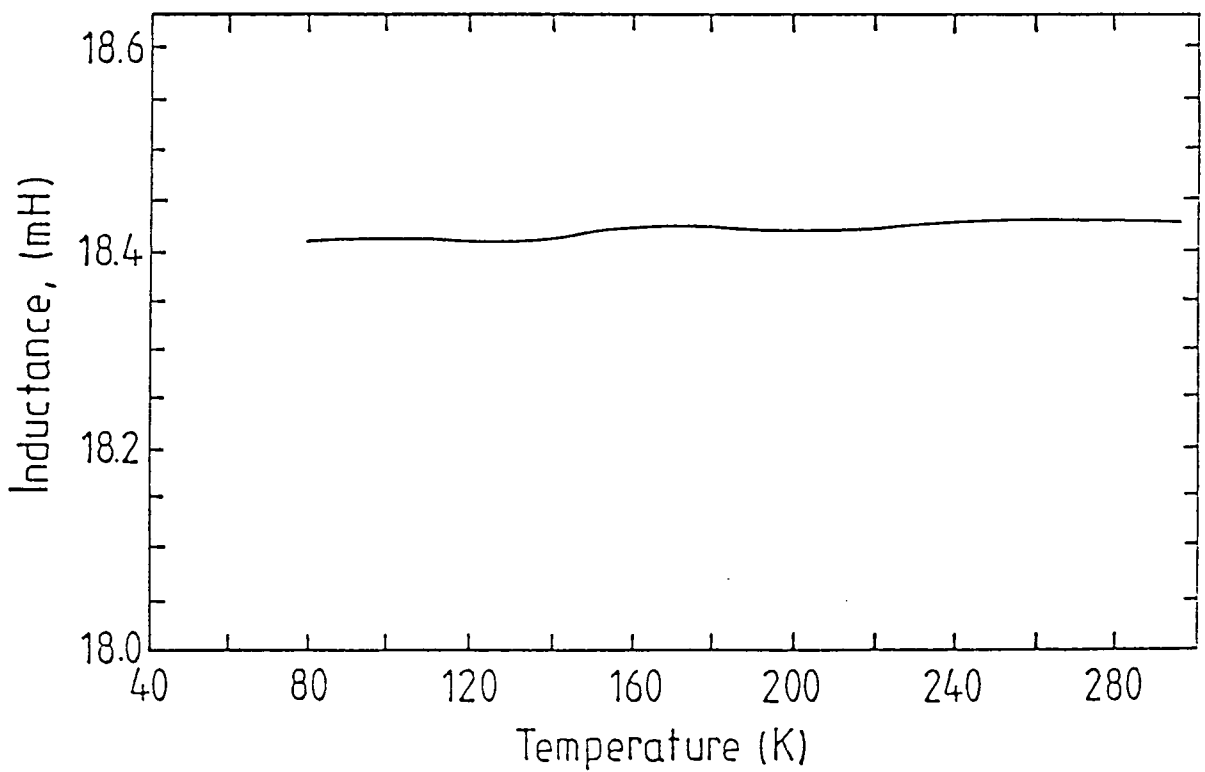Figure 3.3: Inductance probe data; empty coil, (coil 1)

Figure 3.4: Inductance probe data; specimen, pure Al_2O_3, coil 2.
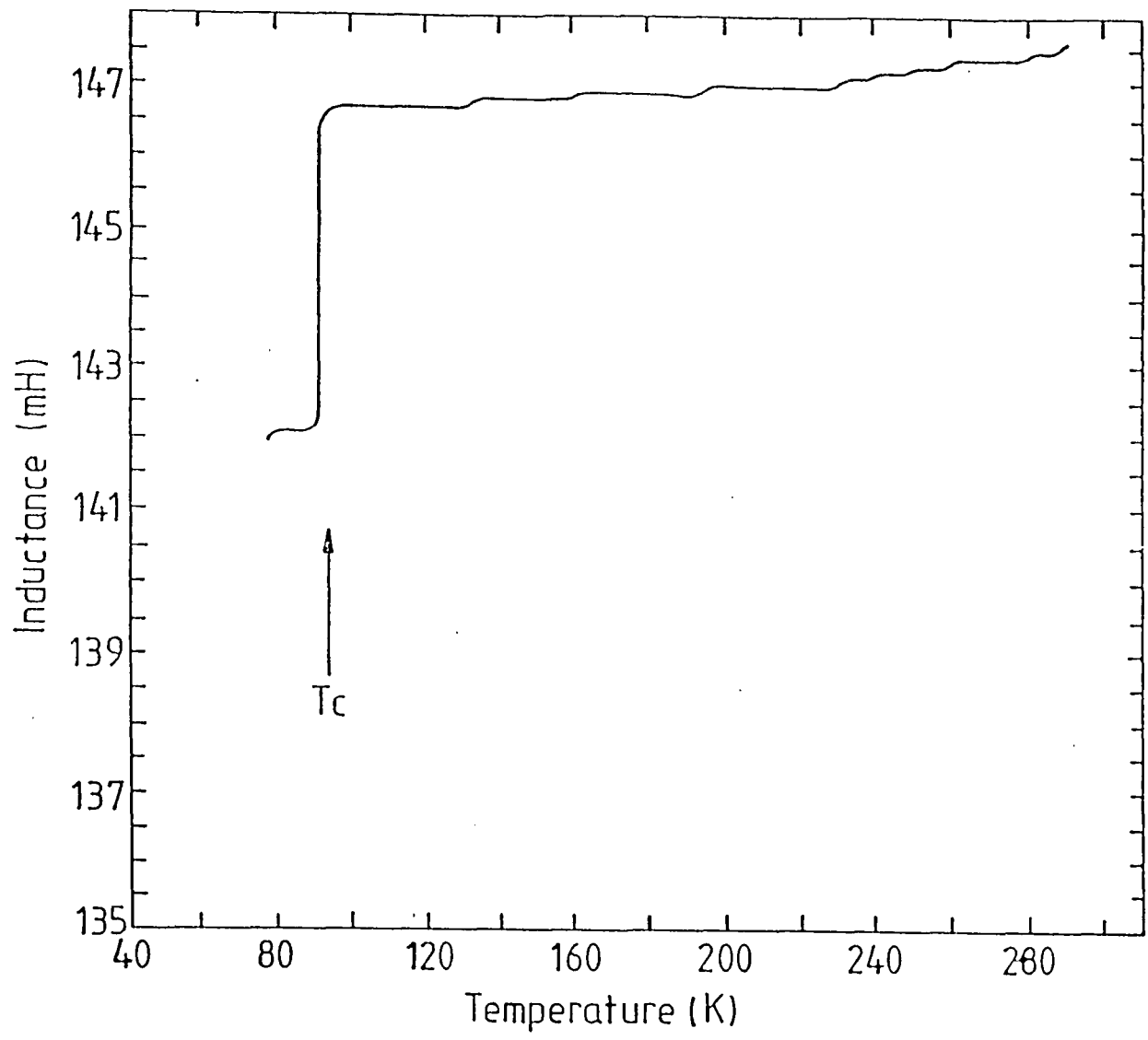
Figure 3.5: Indutance probe data; specimen 1A (coil 1).

very narrow, certainly not exceeding 2 K. Above (T_c) there is a small positive linear temperature dependence of inductance , which is of the same order of magnitude as was found for the empty coil. Correspondingly, below (T_c) the inductance remains sensibly constant.

In order to determine the effect of different preparation techniques and different starting materials on (T_c), several other specimens were examined. These were also of nominal composition $YBa_2Cu_3O_{7-x}$ and were obtained from several sources. Different quality starting materials and different preparation routes were used. The results for specimens 2A and 3A are shown in Figures (3.6) and (3.7) respectively. For specimen 2A there is a drop in the inductance , which starts at 110 K. The drop however is not sudden but extends over a very wide temperature range of nearly 30 K. In this specimen (2A) superconductivity starts at a considerably higher temperature than in specimen (1A) but the gradual fall in the inductance suggests that more than one phase is present, each phase having a different value of (T_c). By comparison with Figure (3.1), a further difference is illustrated by Figure (3.7) which gives a very small drop in inductance. Another example, for specimen 4A, is given in Figure (3.8) which does not give any evidence for a superconducting transition at temperatures above 77K.

Inspection of the inductance versus temperature data given by this method, (used here at 10 KHz), proves that a good method for measuring (T_c) with an accuracy of ± 1K has been developed. The method also has several attractive features in that
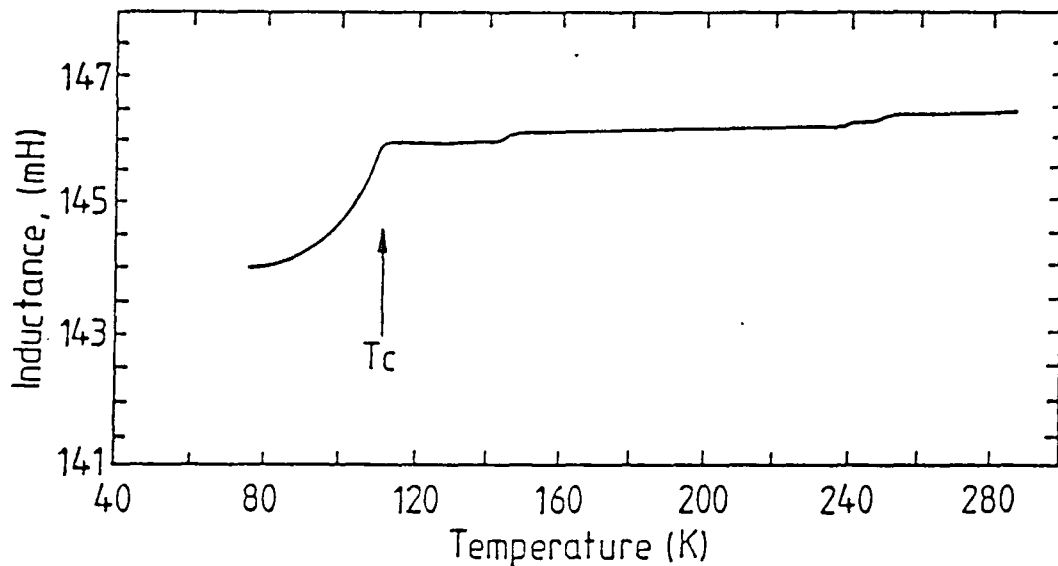
Figure 3.6: Inductance probe data; specimen 2A, (coil 1).
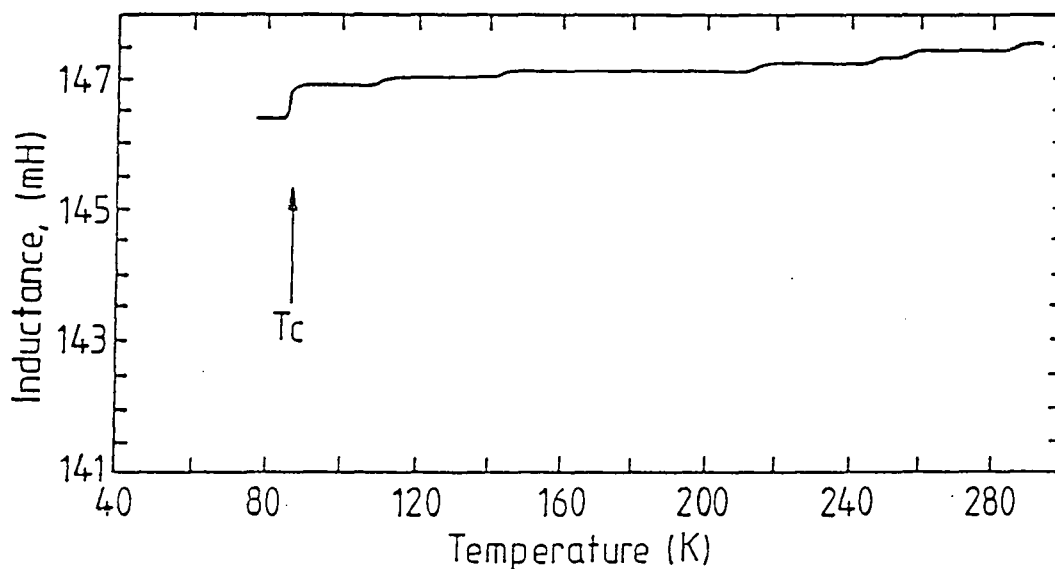
Figure 3.7: Inductance probe data; specimen 3A, (coil 1).
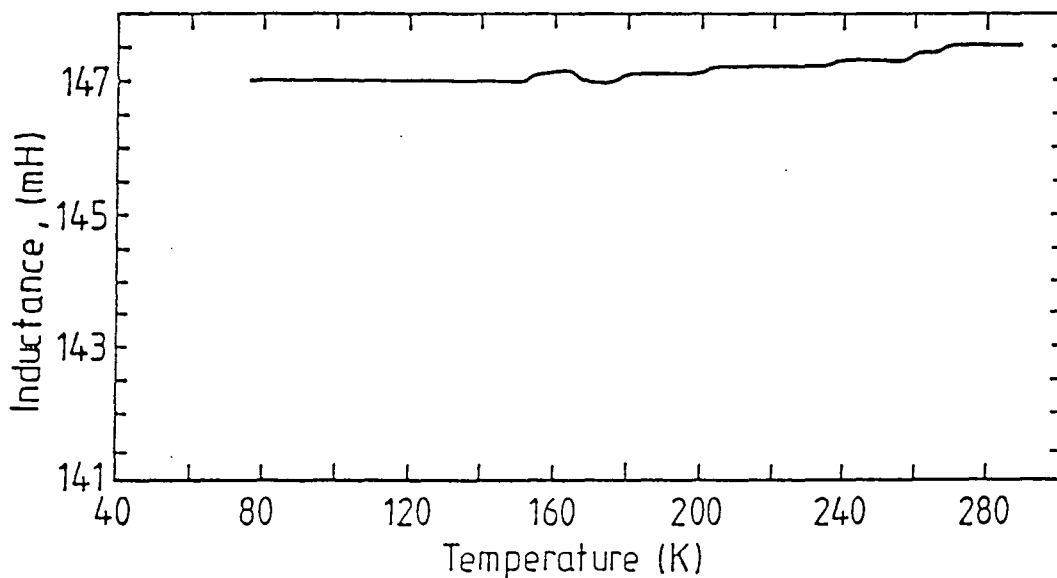
Figure 3.8: Inductance probe data; specimen 4A, (coil 1).

specimens can either be in the form of solids (i.e pellets), tapes or, as here, powders. For the determination of (T_c) only it is not necessary that the whole volume of the coil is filled with the superconductor. Furthermore, there is no requirement for electrical contacts, which cause a considerable problem in the resistance-temperature method for finding (T_c) [3.3,3.12].

3.4 Determination of Percentage of Superconducting Material

The experiment used to measure (T_c) can also be used to estimate the percentage amount of superconducting phase present in the specimen used by monitoring the change in the absolute value of inductance with temperature. As we have seen in section 3.2 there should be no change in the inductance for an empty coil between room temperature and low temperature. According to the basic definition the inductance of a coil is given by

$$L = \frac{\mu N^2 A}{l} \qquad (3.1)$$

where L is the inductance (H), A is the cross-sectional area (m^2), l is the length (m), N is the number of turns and μ is the permeability (Hm^{-1}) of the material which filled the coil. Tests were made to confirm that there is a good agreement between theoretical and experimental values for several standard instances. For one air filled coil with $N = 1000$ turns, $A = 7.85 \times 10^{-5} m^2$, $l = 5.2 \times 10^{-3} m$, $\mu = 4\pi \times 10^{-7} Hm^{-1}$, the theoretical inductance was 0.0189 H as compared with the experimental value of 0.0184 H . For another air filled coil with $N = 3010$ turns , $A = 9.50 \times 10^{-5} m^2$, $l = 7.2 \times 10^{-3} m$, $\mu = 4\pi \times 10^{-7} Hm^{-1}$, the theoretical inductance was 0.150 H, as

compared with the experimental value of 0.1463 H.

For coils completely filled with superconducting materials however we can estimate the percentage of superconductor inside the coil as follows: For any superconducting material the percentage is

$$\frac{L_{\text{room temperature (293 K)}} - L_{\text{low temperature (77 K)}}}{L_{\text{room temperature (293 K)}}} \times 100 \qquad (3.2)$$

In practice all the measurements made here used powders and so allowance must be made for the packing fraction. The definition of the packing fraction is as follows. The mass m of powder which fills the known volume V of the bore of the coil is found by weighing the empty and filled coil. If the true (x-ray) density of the material is ρ_x the mass will occupy a volume V_1 given by

$$V_1 = \frac{m}{\rho_x}$$

so

$$P = \frac{V_1}{V} = \frac{m}{\rho_x V}$$

The effect of the packing fraction on the L-T plot is shown in Figure (3.9). If it is assumed that all the material is superconducting the inductance should fall from room temperature value to zero below T_c, Figure (3.9a), if the coil was completely filled i.e with $P = 100\%$. For a partially filled coil (i.g $P = 50\%$, Figure (3.9b)) the inductance below T_c will fall to a value such that the drop from the room temperature inductance $\triangle L_2$ is given by

$$\triangle L_2 = PL_{RT}$$
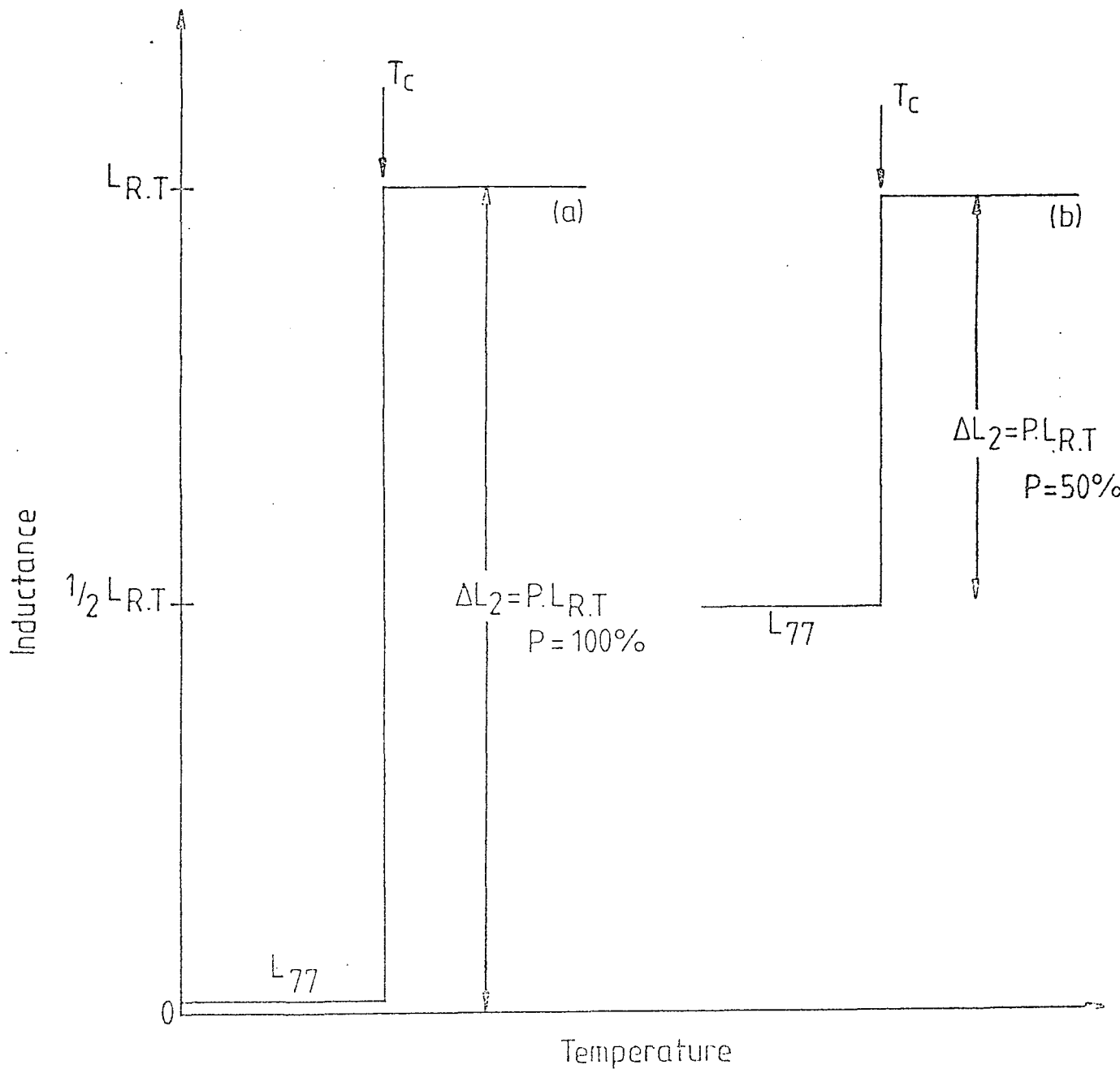
Figure 3.9: The effect of packing fraction on L-T plot; all material superconducting, (a) p = 100 %, (b) p = 50 %.

However if the material contains both superconducting and non-superconducting components the fall in the inductance will not be as great; this is illustrated in Figure (3.10) which compares the behaviour of a fully superconducting powder with that of a partially superconducting powder having the same packing fraction. For a packing fraction P the residual inductance at 77K (i.e below T_c) would be

$$L_{77(Th)} = L_{RT} - PL_{RT}$$

where $L_{77(Th)}$ is the theoretical value expected if the field is fully expelled from all the powder, and L_{RT} is the inductance above T_c , which is taken at room temperature. The fall in inductance $\triangle L_1$ on cooling below T_c should therefore be PL_{RT}. The percentage of superconductor present S% is given by

$$S = \frac{\triangle L_1}{\triangle L_2} = \frac{L_{RT} - L_{77(exp)}}{PL_{RT}} \times 100 \qquad (3.3)$$

It can be seen that for a completely filled coil (i.e P = 1) equation (3.3) gives the same result as equation (3.2). In practice it was found that using modest pressures when filling the coil with a powder packing fractions of about 50% were obtained.

The values of $S\%$ were calculated on this basis for each powder. The results are shown in Table 3.1 from which is seen that the sample Durham 1A, which gave the most pronounced drop in the L-T curve, only contains 7% of superconducting material; the other samples gave smaller percentages. These were much smaller than expected, since the x-ray diffraction data (which is discussed in detail in Chapter Two) shows that over about 95% of the material is single phase YBCO. Because of

Specimen	1A	2A	3A	4A	Niobium
P%	55	54	55	57	50
L_{RT} (mH)	147.20	146.50	147.20	147.20	0.487
$\triangle L_1$ (mH)	5.52	2.60	1.05	0.51	0.123
$\triangle L_2$ (mH)	81.10	79.60	81.10	84.10	0.244
S%	7	3.2	1.2	0.6	50
T_c (K)	90	86-105	86	86	9.2

Table 3.1: Percentages of superconducting material in different YBCO powder specimens compared with niobium powder.
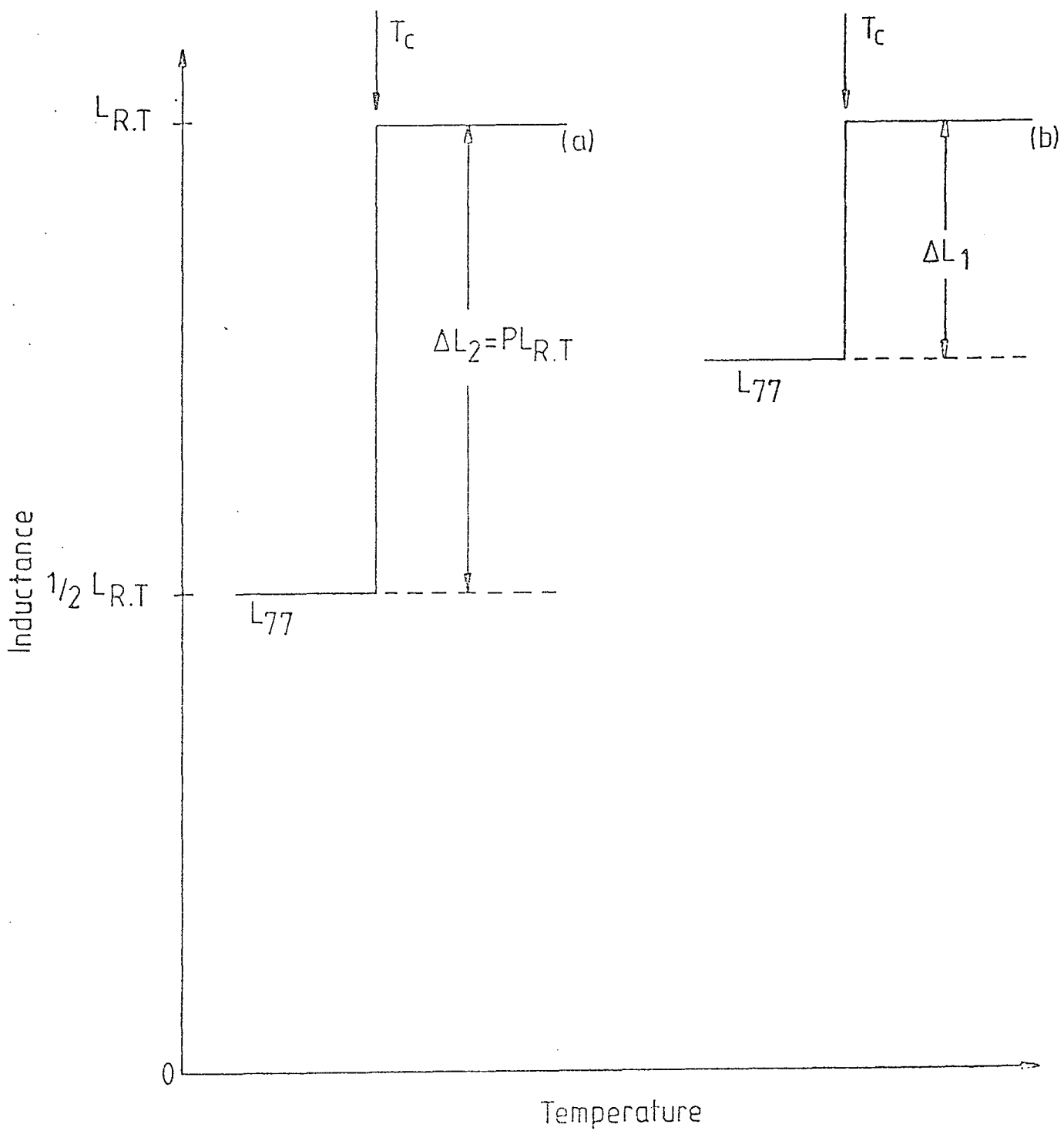
Figure 3.10: Effect of the percentage of superconducting powder
(a) $s = 100\%, p = 50\%$
(b) $s = 100\%, p = 50\%$

this two experiments were performed with the object of testing the general validity of the method. The first of these involved filling the coil with increasing amounts of a ferromagnetic material, iron powder, which should have had the effect of increasing the inductance in proportion to the volume of the coil filled by the ferromagnetic. The second experiment used another superconductor, niobium powder, with which a drop to zero inductance was expected on cooling below the critical temperature of 9.3 K. [3.12].

3.4.1 Calibration Experiments: Ferromagnetic Material

To ensure that at all times the coil was completely filled with powder it was decided to used iron loaded aluminium oxide powder rather than a smaller volume of iron by itself. By this means the iron concentration could easily be varied from 1% to 100% by weight by altering the proportions of the two constituents. The volume fraction of iron used at a particular concentration was obtained knowing the weight fraction and the density. For all the mixtures, the inductance increased with increasing amount of iron; the coil was always completely filled using the same packing fraction. Figure (3.11) gives the variation of inductance with the volume fraction of iron present. The plot shows that the variation is approximately linear giving values of inductance which vary from 18.40 mH for the empty coil to 25.70 mH for the coil completely filled with iron powder. The magnitude of the increase to be expected for the 100% Fe filling is

$$L = \frac{\mu N^2 A}{l}$$
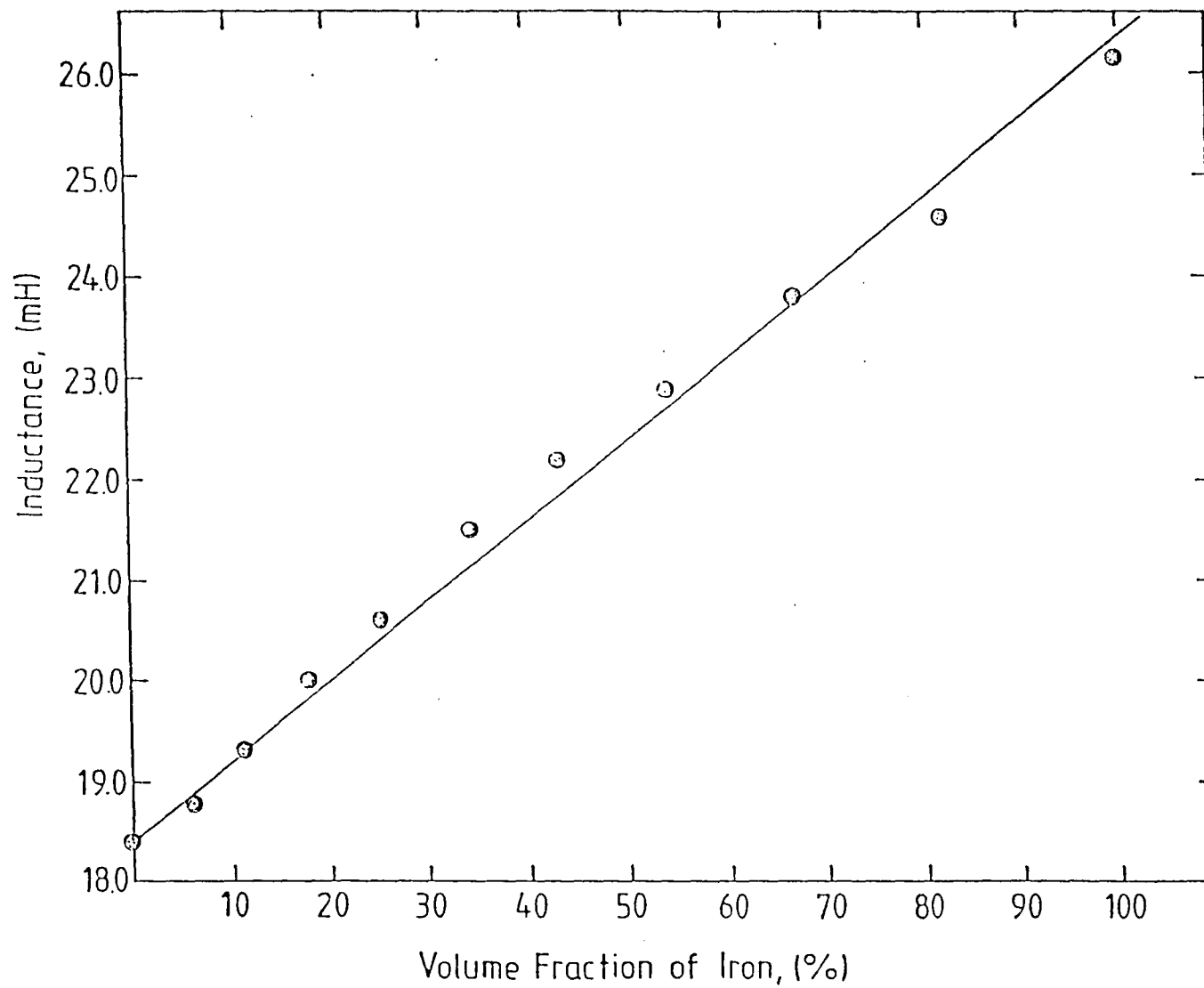
Figure 3.11: Variation of inductance with volume fraction of iron filling.

where here μ is the permeability of Fe given as

$$\mu = \mu_0 \, \mu_r. \tag{3.4}$$

The relative permeability μ_r for Fe is field dependent, the variation being shown in Figure (3.12). The low field value of permeability must be used here because the magnitude of the flux density (B_2) generated by the current passing through the coil during measurement is only about $1.04 \times 10^{-4} T$. This value was obtained from the expression

$$B_2 = \mu_0 N I = \frac{\mu_0 N V}{l\sqrt{(R)^2 + (2\pi f L)^2}} \tag{3.5}$$

by substituting the values of the parameters, (the number of turns N=1000, the voltage V=0.5 volt, the length $l = 5.2 \times 10^{-7} m$, the resistance R=186 Ω, the inductance $L = 18.42 \times 10^{-3} H$ and the frequency $f = 10 \times 10^3 \mathrm{Hz}$). In order to calculate μ_r in the low field region the curve of relative permeability μ_r against flux density B for iron given by Bleaney [3.11] was used. From Figure 3.12, at the magnetic field value $B_1 = 0.125T$, the relative permeability is $\mu_{r1} = 2000$ and the variation of μ_r with B is linear at fields below (B_1). Thus the value of relative permeability , μ_{r2} at the field B_2 due to the coil is

$$\mu_{r2} = \frac{B_2 \mu_{r1}}{B_1} = 1.65$$

Using equation 3.2 gives the permeability μ as

$$\mu = 2.1 \times 10^{-6} H m^{-1}$$

Inserting this value for μ in equation 3.1 gives a theoretical value for the completely
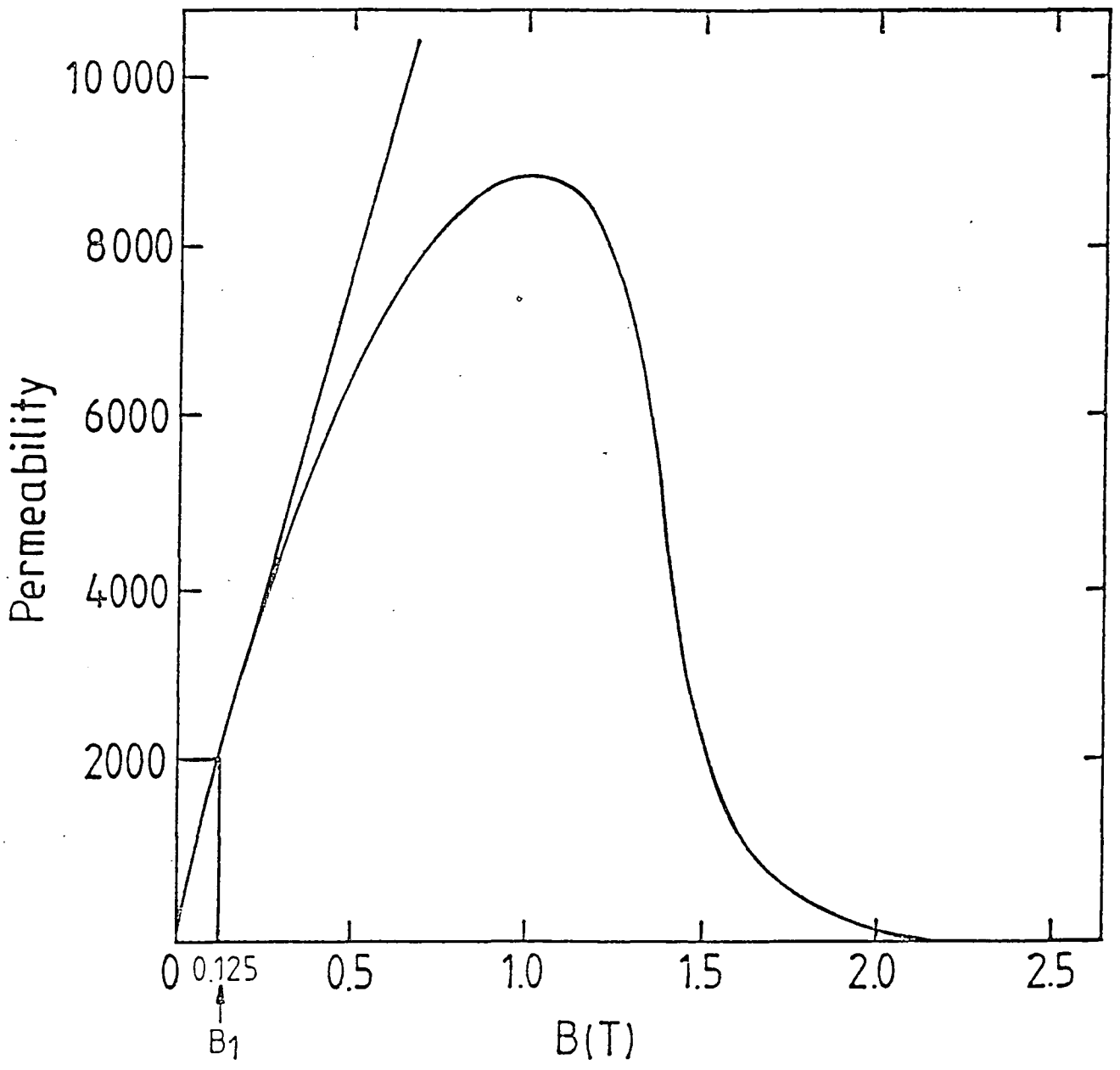
Figure 3.12: Dependence of relative permeability μ_r on flux density (B) for iron.

iron filled coil of

$$L_{FeTheory} = 31.71 mH$$

Care needs to be taken, however, because we should allow for the packing fraction, because Fe powder was used. The packing fraction was estimated as follows. The volume of the bore of the coil (which corresponds to the volume of powder) was $0.584 \, cm^3$. The weight of iron powder needed to fill this volume was determined directly as 3.0012 grams. Thus the density of the powder in the coil is given by the ratio 3.0012/0.589, i.e 5.095 $g.cm^{-3}$. The true (x-ray) density is 7.86 $g.cm^{-3}$, and hence the packing density, defined as the ratio of the powder density to the true density, is 5.095/7.86 or 65%. Consequently, the predicted inductance allowing for the packing fraction will be

$$L_{FeTheory} = 31.71 \times 0.65 = 20.62 \, mH$$

This is in a good agreement with the inductance value observed experimentally which was

$$L_{FeExperimental} = 25.70 \, mH$$

This shows that, for a ferromagnetic material, the inductance L does change in proportional to the volume of the coil filled by the ferromagnetic material.

3.4.2 Calibration Experiments: The Behaviour of Niobium

It was decided to complement the previous experiment with one in which the coil was filled with a material known to be a good superconductor. For this purpose

niobium was choosen because its superconducting propertes are well known [3.11-3.13]. It has a transition temperature of 9.3K and it is a Type II material. Because a liquid helium temperature experiment was necessary a special coil was made which could fit down the constricted diameter of the neck of the the transport dewar used to contain the liquid helium, Figure 3.13. Because it was easily available niobium powder was used to fill the coil (as distinct from a solid piece of niobium, which would have had to be specially shaped to fit the bore). Under the experimental conditions used the packing fraction was 51.3 %. This was calculated by methods similar to those used previously. Here however the coil radius was 4.5 mm and it's length was 4.00mm. The weight of the volume of the powder used, ($0.19cm^3$), was 0.84 gram. The x-ray density of niobium is 8.57 g.cm^{-3} and so the packing fraction was 51.3 %. Measurements were made firstly at room temperature and then at 4.2 K with the coil completely immersed in the liquid helium. The results were $L = 487.40 \pm 0.20 \mu H$, at 293 K and $L = 364.90 \pm 0.10 \mu H$, at 4.2 K. The drop in inductance was about 25% rather than the 50% predicted in the basis of the known packing fraction. This gave a percentage of superconductor of about 50%. There does not seem to be any report of inductance probe measurement of (T_c) for niobium in the literature. However there are several reports of the determination of T_c by the resistance temperature method. One of the earliest of these was by Von Minnigerode [3.12] and Figure (3.14) reproduces his data for pure niobium. From this it can be seen that the transition is very sudden extending only over about 0.1K. These results were confirmed by similar data obtained by Desorbo [3.13]. Both these authors give results showing that the

43
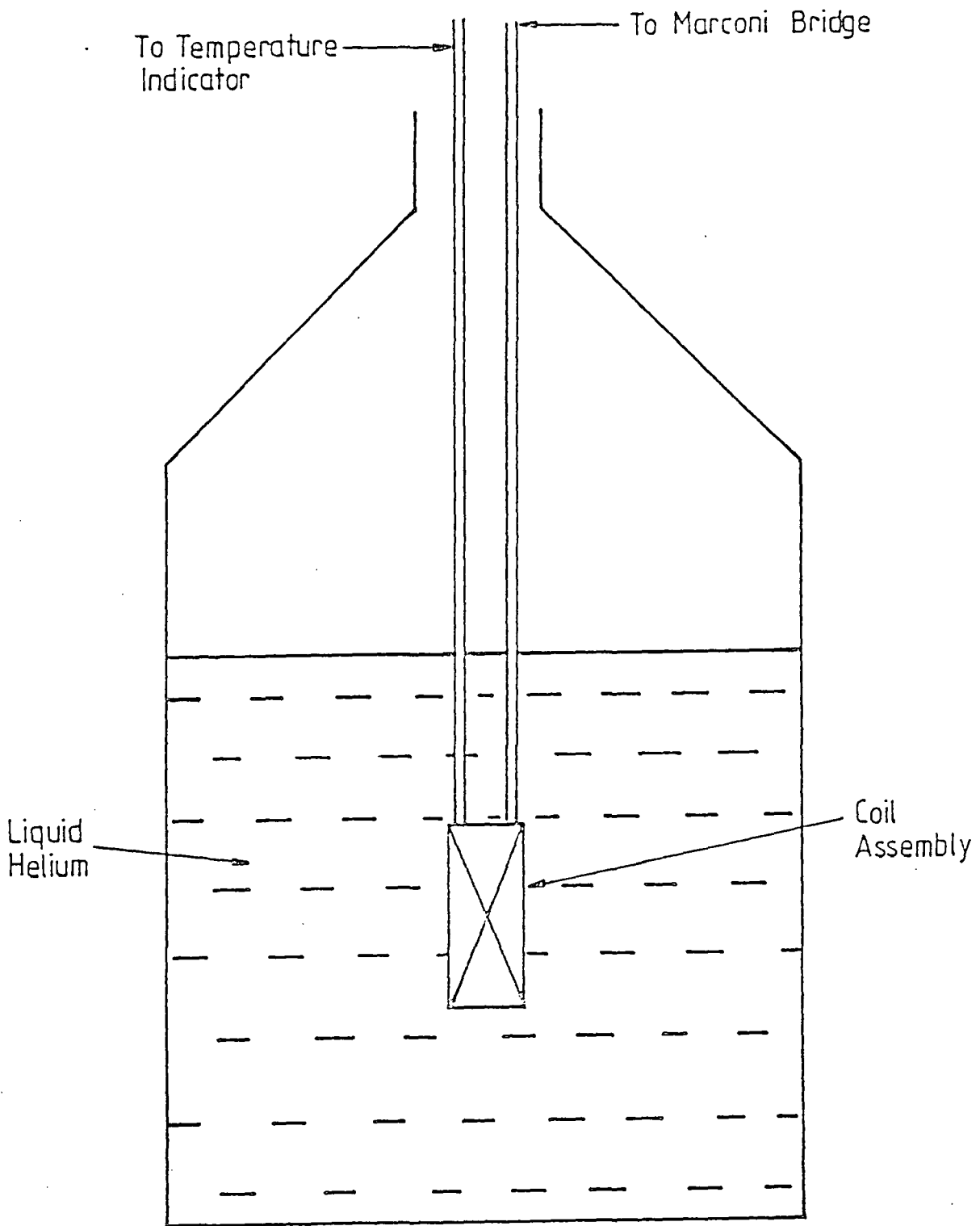
Figure 3.13: Arrangement used for 4.2K experiment.
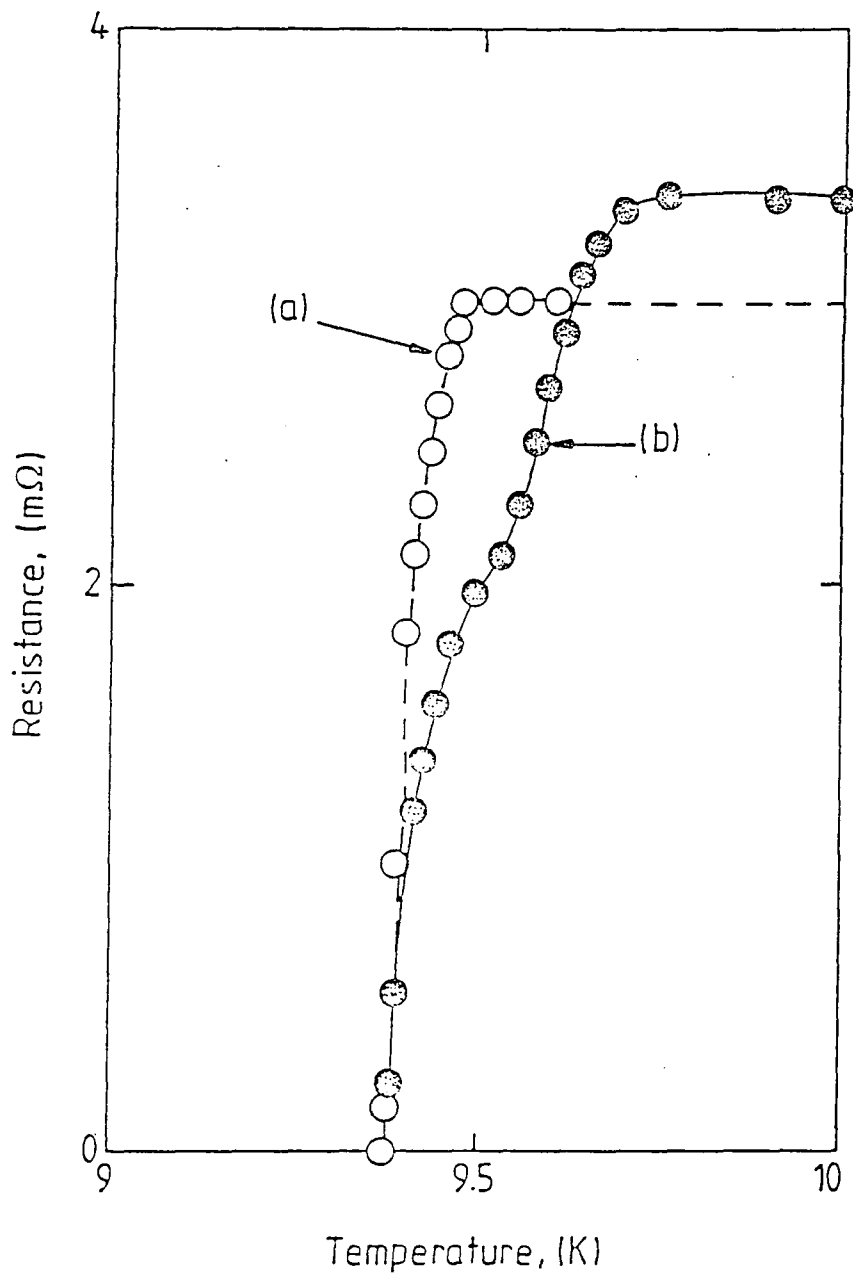
Figure 3.14: Resistance - temperature characteristics for niobium; (a) before and (b) after cold working.

superconducting transition is complete at temperatures very closely below T_c, even if the material contains some impurity (i.e oxygen , nitrogen or hydrogen). The latter author also gave the value of magnetic field at which penetration began at 4.2 K as 1.32 m T.

The experimental result from the inductance versus temperature data that only 50% of the magnetic field is expelled is rather suprising. If the sharpness of the transition seen in the resistance versus temperature measurement holds also in the inductance versus temperature measurement there can be no increase in the percentage because of a long tail giving increased superconductivity at temperatures considerably below the 4.2 K used for the measurement. The magnetic field generated by the current passing through the coil during measurement was between about 1-2mT, which is of the same order of magnitude as than the penetration field value of 1.3 mT. (The field generated was obtained from the relations

$$B = \mu_0 H = \frac{\mu_0 N V}{l\sqrt{(R^2) + (2\pi f L)^2}}$$

where the current was determined by knowing the voltage applied to the particular coil whose impedence was known). Thus is quite probable that there is some field penetration which of course would reduce the effective packing fraction. A second possibility is that some effective loss of volume might be expected with niobium powder because niobium is a reactive element and consequently each niobium grain may   have a surface covering of niobium oxide. Furthermore the niobium grains may not be initially strain free.

44

The importance of these two calibration experiments is that the actual data given in Table 3.1 must be taken as substantially correct for all the YBCO powders. The implication is that only a small fraction is superconducting. This may be due either to field penetration (which would reduce the effective volume of superconducting material) or to the presence of phases which were closely similar crystallographically to $YBa_2Cu_3O_7$ but were oxygen deficient and so were not superconducting.

3.5 The Effects Of Annealing In Oxygen.

It is very well established in the literature e.g. West [3.14], Specht [3.15], that heat-treatment in oxygen effects the oxygen concentration. West's data shows that to obtain the stoichiometric ratio $Y_1Ba_2Cu_3O_7$ the sample should not be heated above 450°C. The superconducting phase has this composition and according to West is best obtained by continuing the heat-treatment until no further weight gain is observed. This superconducting phase is not stable under ordinary laboratory conditions because it absorbs water vapour from the atmosphere; this degrades the material because it tends to form hydroxide with corresponding changes in the Y:Ba:Cu:O ratios; several workers state that a degraded material can be restored by heat-treatment in flowing oxygen. This was attempted for three powders using temperatures between 300°C and 450°C. The first powder examined, 2A, initially showed the very wide superconducting transition given in Figure 3.6. After as little as 6 hours treatment a marked difference was observed; the transition became much sharper with a T_c value of 86K and width reduced from 30K to about 10K. There was a corresponding small

45

increase in the value of S (the fraction of superconducting material) which increase from 3.2% to 3.8%. Further heat-treatment up to 38 hours did not produce any significant change in the shape of the transition but caused a further small increase in S to 4.3%. Continuing heating for 86 hours, Figure 3.15, did not produce further increase in S% which remained at 4.3%.

The next sample examined, 3A, which had only given a small amplitude transition originally (Figure 3.7) showed very little change after heating for periods up to 48 hours at 300°C, the temperature recommended by West [3.14] although the S value increased very slightly from 1.2% to 1.8%. For the third sample, 5A, which contained considerably less iron than 3A no superconducting transition was observed either in the as received state or after a heat-treatment of 36 hours at 400°C.

3.6 Measurements On Sintered Pellets.

Inductance-probe measurements were also made on several polycrystalline sintered pellets whose microstructure has been discussed in Chapter Two. Each of these had been made from the corresponding powder by sintering at 950°C in air followed by slow cooling. In the measurement the coil was filled as completely as possible with large pieces of the sintered pellet. For 3A (sintered pellet) there is a sharp transition at 90K, Figure 3.16, and it is immediately evident that there is a much more marked drop in inductance than with the 3A powder shown in Figure 3.7. The percentage of superconducting material, derived from Figure 3.16, now is 15% which was the
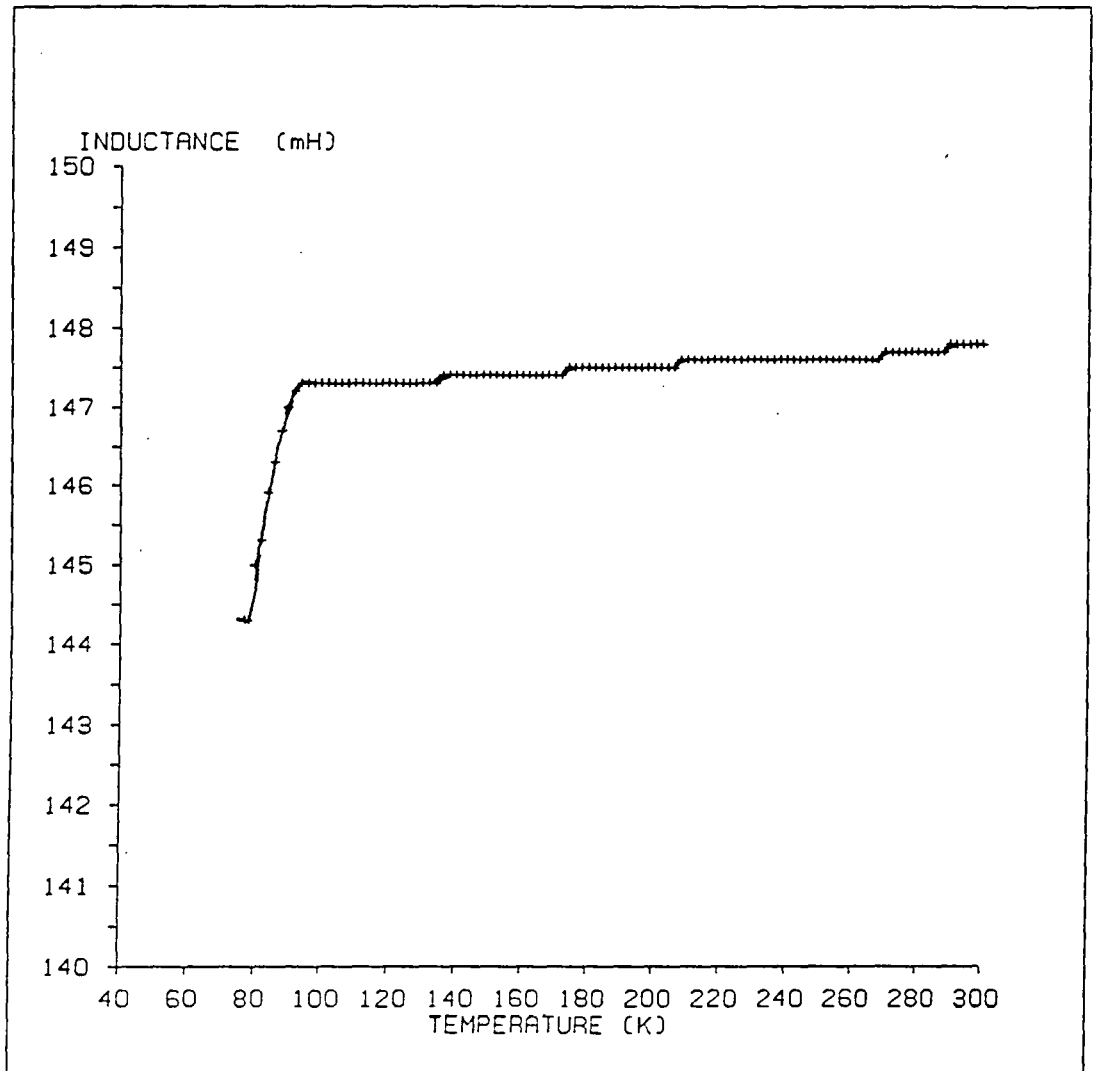
Figure 3.15: Inductance probe data; specimen 2A after 86h heat treatment in oxygen (coil 1).
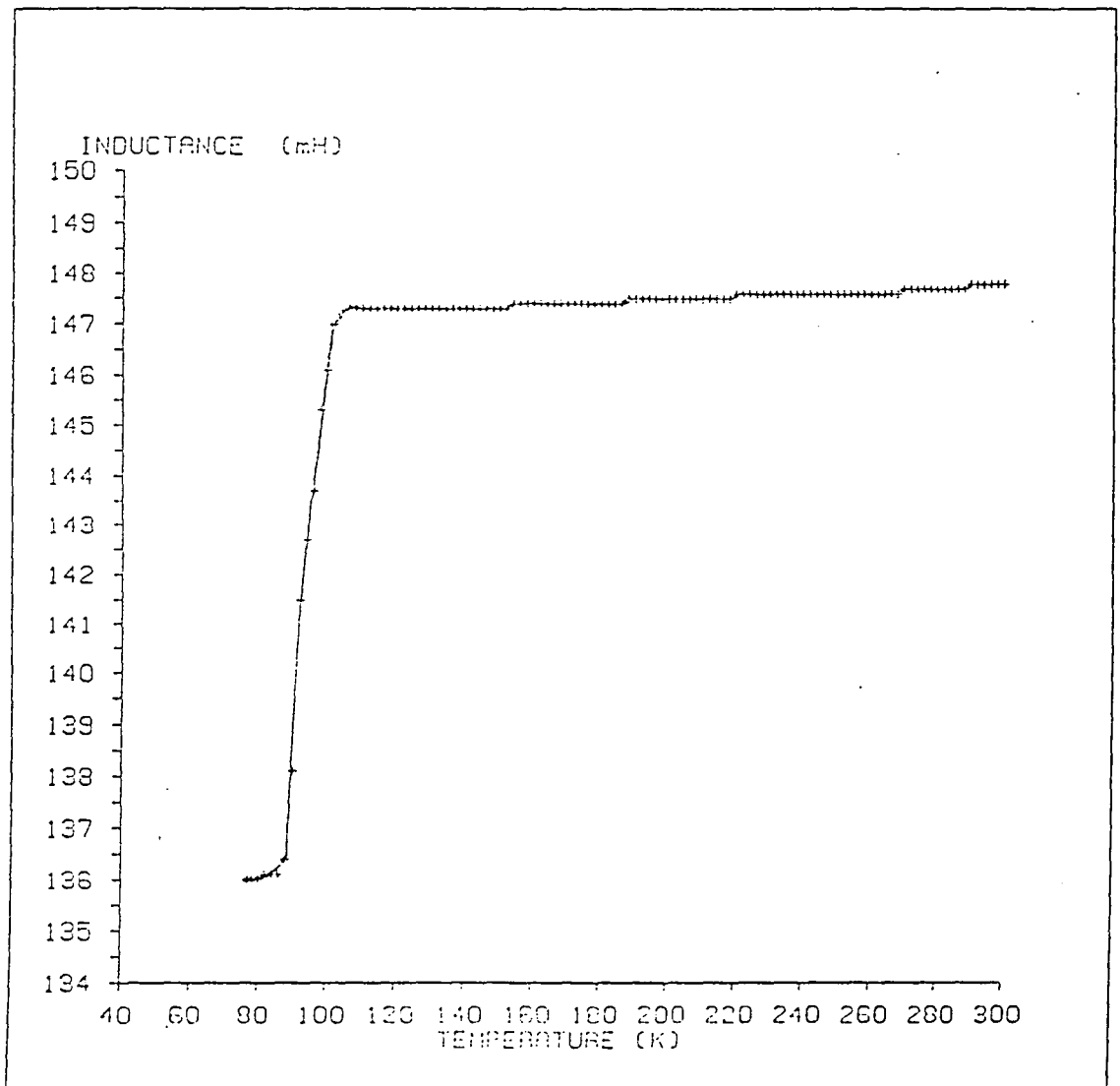
Figure 3.16: Inductance probe data: specimen 3A, sintered pellet, (coil 1).

largest value observed apart from that for niobium. The effects of sintering in altering the behaviour of the material are again emphasised by the result obtained for the sintered pellet 5A. The comparison given in Figure 3.17 shows that as powder there was no evidence at all for superconductivity at temperatures above 77K; however, after the production of the sintered pellet, there is a sharp and well defined transition at 86K. The S value for this sintered pellet is about 11%, again much larger than the value in the powder from which it originated. These results show that the sintering conditions radically influence the superconducting behaviour and suggest that further optimisation of the sintering conditions could lead to further increase in the percentage of superconducting material obtained. Further measurements were made on sintered pellet 7A which had been heat treated to promote grain growth; the L-T plot is shown in Figure 3.18. This shows a very clean and sudden transition at 124K considerably higher than observed for any other sample; the width of the superconducting transition is only about 3K. Calculation of the percentage of superconducting material gave the value of $S = 25\%$ which is the largest value observed for any sample examined.
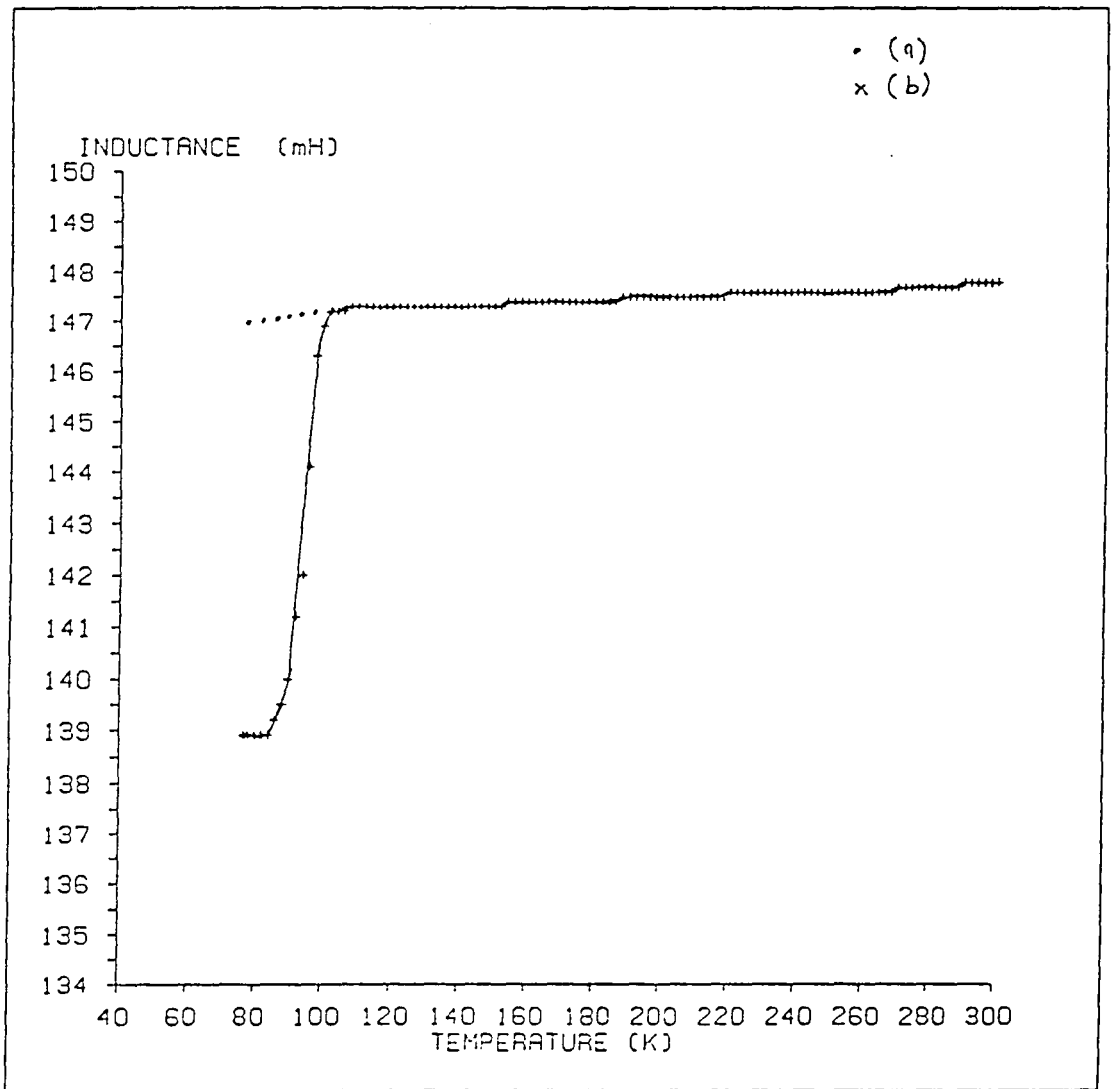
Figure 3.17: Comparison of inductance probe data; for a) 5A powder, and b) 5A sintered pellet (coil 1).
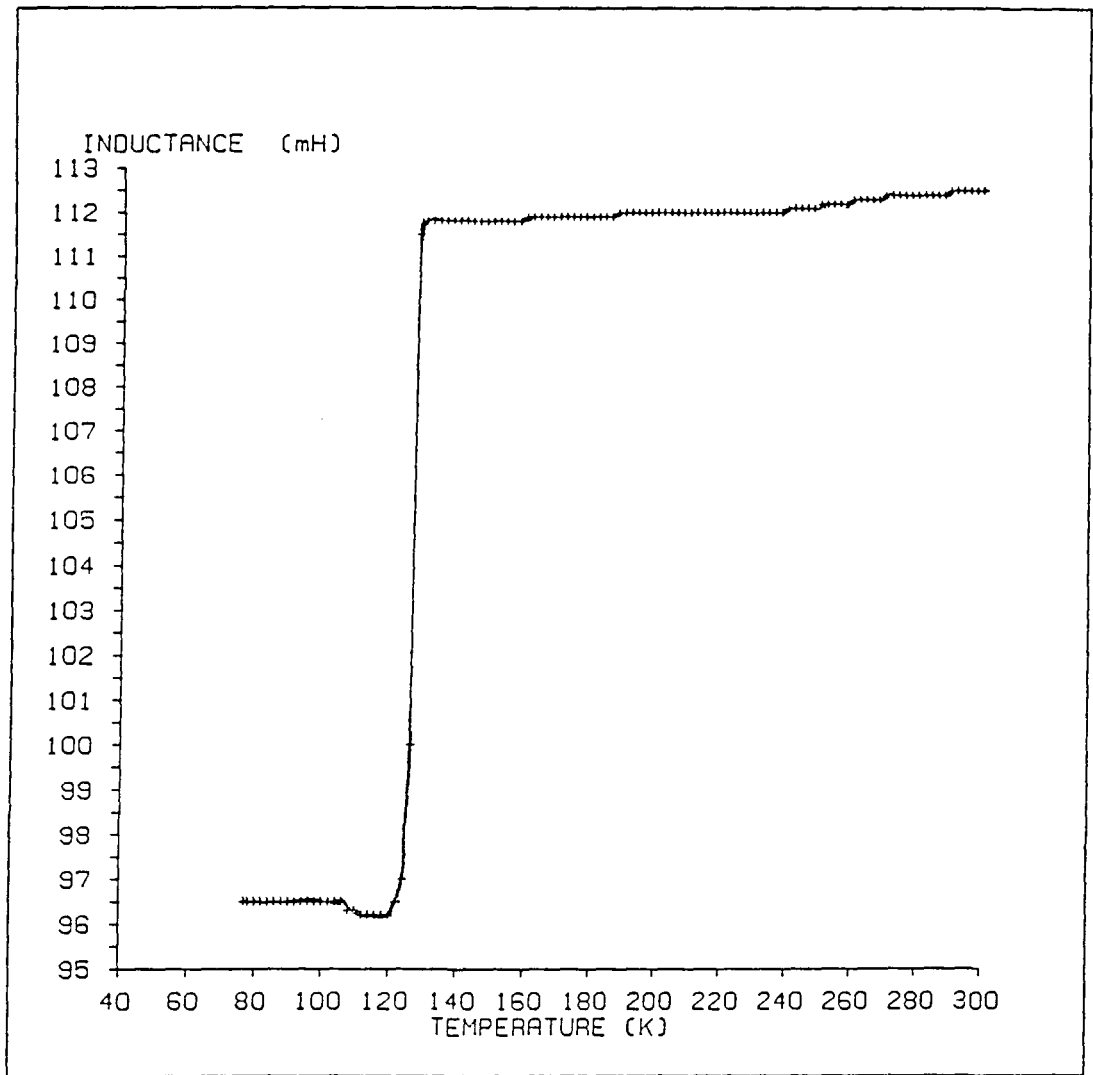
Figure 3.18: Inductance probe data; specimen 7A, sintered pellet.

REFERENCES

3.1 W.Meissner and R.Ochsenfeld, Naturwiss ,21 , 787 , (1933).

3.2 M.K.Wu, J.R.Ashburn, C.J.Torng, P.H.Hor, R.L.Meng, L.Gao,

Z.J.Huang, Y.Q.Wang, and C.W.Chu, Phys. Rev. Lett. 58,908,(1987).

3.3 P.H.Hor, L.Gao, R.L.Meng, Z.J.Huang, Y.Q.Wang, K.Forster,

J.Vassilious, C.W.Chu, M.K.Wu, J.R.Ashburn, and C.J.Torng,

Phys. Rev. Lett. 58,911 , (1987) .

3.4 T.R.McGuire,T.R.Dinger,P.J.P.Freitas, W.J.Gallagher,

T.S.Plaskett, R.L.Sandstrom and T.M.Shaw, Phys. Rev. B.36,4032, (1987).

3.5 R.J.Cava,B.Battlogg,R.B.van Dover,D.W.Murphy,S.Sunshine,T.Siegrist,

J.P.Remeika, E.A.Reitman, S.Zahurak and G.P.Espinosa,

Phys. Rev. Lett. 58 , 1676 (1987).

3.6 C.Politis, J.Geerk, M.Dietrich, B.Obst and H.L.Luo, Z. Phys.

B- Cond. Matt. 66 , 279 , (1987).

3.7 H.Kupfer,I.Apfelstedt, W.Schauer, R.Fluxkiger, R.Meier-Hirmer and

H.Wuhl, Z. Phys. B- Cond. Matt. 69 , 159 , (1987) .

3.8 E.Greedan. A.O'Reilly and C.V.Stager,

Phys. Rev. B 35 , 8778 , (1987) .

3.9 T.Siegrist, S.Sunshine, D.W.Murphy, R.J.Cava and

S.M.Zahurak, Phys. Rev. B 35 , 7137 , (1987) .

3.10 H.Takagi, S.Uchida, H.Sato, H.Ishll, K.Kishio, itazawa, K.Fueki,

and S.Tanaka, Jpn. J.Appl. Phys. 26 , L601 , (1987) .

3.11 B.I.Bleaney and B.Bleaney " Electricity and Magnetism " ,

3rd Ed , Oxford University Press .UK. (1976) .

3.12 Gunther Von Minnigerode , Z . Phys. 154 , 442 , (1959) .

3.13 Warren Desorbo , Phys. Rev. 132 , 107 , (1963) .

3.14 J.T.S.Irvine, J.H.Binks and A.R.West. Proc. Europ. Workshop on

High T_c superconductors and potential applications, 297 (1987).

3.15 E.D.Specht, C.J.Sparks, A.G.Dhere, J.Brynestad, O.B.Cavin,

D.M.Kroeger and H.A.Oye, Phys. Rev. B37, 7426, (1988).

CHAPTER FOUR

INDUCTANCE-PROBE TECHNIQUES; MEASUREMENTS

OF H_{c_1} AND HYSTERESIS

4.1 Introduction

It is important to know the value of H_{c_1}-the lower critical field- for the material because this is the field at which field penetration becomes important. As shown in the previous Chapter the percentages of superconducting volume were all found to be much lower than expected, being typically about 10% at most. As pointed out earlier several factors may be responsible for this, the principal two being that not all the material is in the correct phase or that, although all the material is the correct phase, the measurements have been made above the critical field H_{c_1} so that, because of field penetration, the volume of genuinely superconducting material is less than the geometrical volume of the material.

Many workers have reported H_{c_1} measurements in the literature [4.1-4.9]. Most of these measurements have been made by magnetization curve methods and a selection of their results is given in Table 4.1(a). From this it can be seen that the reported values of H_{c_1} vary over a considerable range. The highest value is 750 gauss [4.3] and the lowest value is 70 gauss [4.4]. Most of the measurements were made at or near 77K but not all the authors gave precise details of stoichiometric ratios in their materials, particularly as regards the oxygen content. Insufficient information is given

Author	Chemical formulae	Form of specimen	Methods of measurements	H_{c_1} gauss	Temperature of measurements
S.N.Song et al. [4.1]	$YBa_2Cu_3O_{7-x}$	sintered pellet	magnetization curve	700	4.2K
T.R.McGuire et al. [4.2]	$YBa_2Cu_3O_{7-x}$	polycrystalline	SQUID	500	20K
J.G.Perez-Ramirez. et al. [4.3]	$YBa_2Cu_3O_{7-x}$ x=0.2	-	magnetization curve	750	4.2K
Cao Xiaowen et al. [4.4]	$YBa_2Cu_3O_{7-x}$	sintered pellet	magnetization curve	70	77K
R.S.Rubins et al. [4.5]	$YBa_2Cu_3O_{7-x}$	sintered pellet	magnetization curve	100-300	77K
Kobayashi [4.6]	-	polycrystalline	-	80 330	77K 4.2K

Table 4.1(a): Reported values for H_{c_1} in polycrystalline YBCO.

for the value of H_{c_1} to be correlated with the oxygen content. From the present point of view it is noteworthy that none of these authors used an inductance probe for their H_{c_1} determination.

Another widely used magnetic technique for characterizing the superconducting material is to observe the hysteresis loops [4.10]. These are usually obtained from magnetometers (e.g a Vibrating Sample Magnetoremter, VSM) which produce a plot of magnetization versus applied field. Below the transition temperature the super-conductor should behave as a perfect diamagnetic so that the susceptibility should be negative and have the value of $-\frac{1}{\mu_0} = -798000$ J.T^{-2}.m^{-3}. The initial slope of the hysteresis loop can be used to estimate the magnetic susceptibility at low fields and the change in shape of the hysteresis loop indicates the departure from purely dia-magnetic behaviour. An example of a hysteresis curve for YBCO is shown in Figure 4.1 [4.10]. The sample used in this experiment had been made by reacting Y_2O_3, $BaCO_3$ and CuO powders at 1000°C for 6 h in flowing oxygen in a platinum crucible; the powder was subsequently pressed into a disc and sintered at 1000°C for 16h in flowing oxygen. The magnetic measurements were made with a magnetometer with sensitivity of 10^{-4} emu in field up to 0.8T; to minimize the demagnetising effect the field was kept parallel to the plane of the sample. In Figure 4.1 the data marked ZFC corresponds to Zero Field Cooling while FC corresponds to Field Cooling. Ob-servations from the hysteresis curve also enable values of the critical current J_c to be estimated (the critical current J_c is the limiting current which can be passed, at a given temperature, through a superconductor without causing it to become normal).
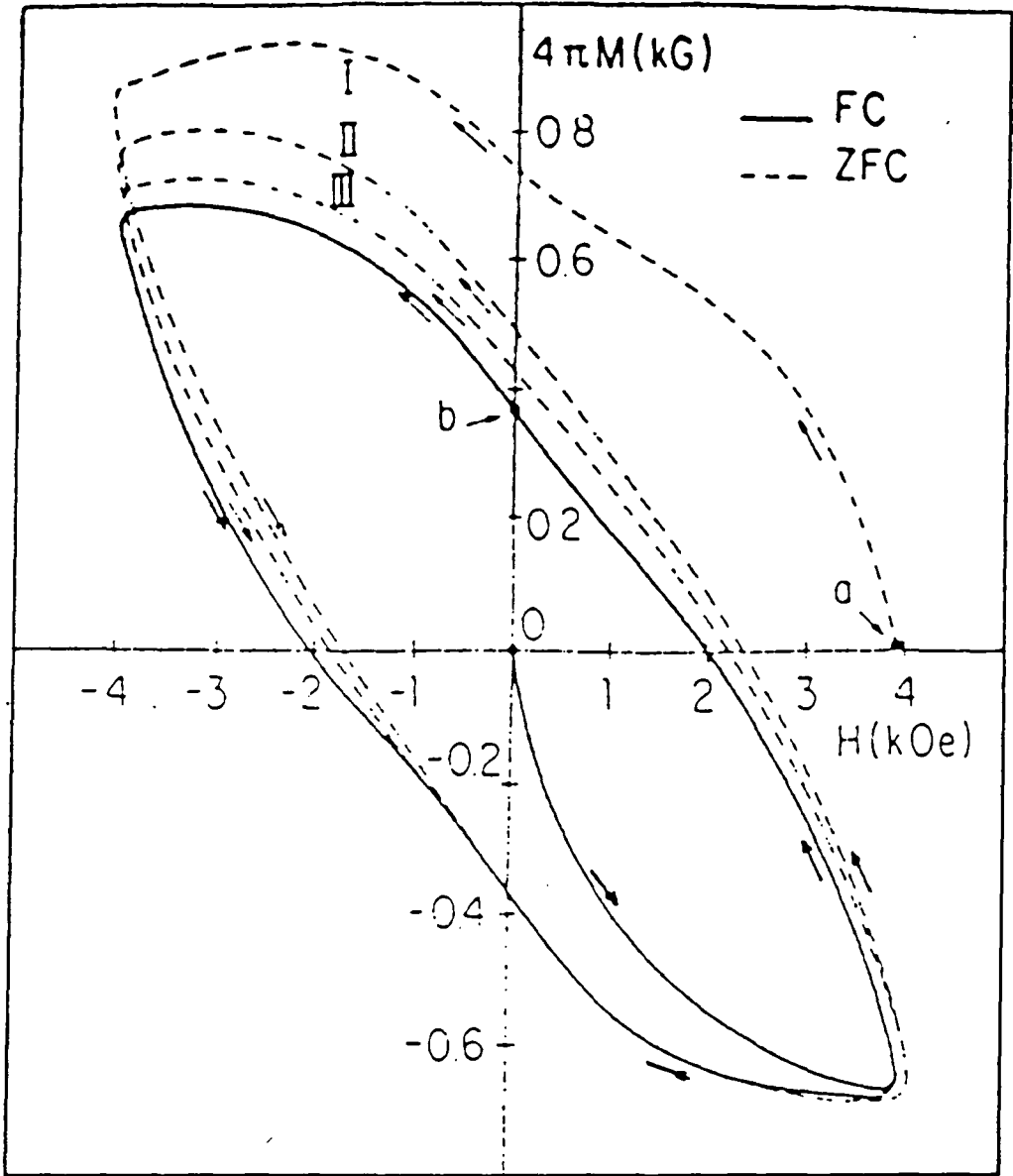
Figure 4.1: Low field hysteresis cycles for $YBa_2Cu_3O_{7-x}$. The solid line represents the cycle obtained after ZFC procedure whereas dashed lines represent cycles obtained after cooling the sample in 4 kOe.

The critical current J_c depends on the temperature and magnetic field surrounding the sample. The reason for a critical current is because the current flowing through a superconductor generates a magnetic field and if this exceeds H_{c_1} field penetration can cause the return to normal resistance. The most usual model used for the derivation of the critical current from the hysteresis plot is the Bean model [4.11]. According to this model the intra-granular critical current density J_c is related to the change in the magnetization $\triangle M$ observed from the hysteresis loop, the density ρ of the material and the dimension R of the individual grains by

$$J_c(A/cm^2) = \frac{30\triangle M(J/T/Kg).\rho(g/cm^3)}{R(cm)}$$

As might be expected the critical current depends on the external field, decreasing as the external field is increased. It has also been found that the J_c values observed vary very considerably according to the different methods of preparation and form (thin film, solid sintered pellet or single crystal) of the sample. For YBCO most authors have quoted values of J_c of about 10^5 A/cm^2 in low fields falling to about 10^3 A/cm^2 in fields of 1 Tesla.

In this work an attempt has been made assess the extent to which similar information can be obtained by the simpler inductance probe technique.

4.2 Experimental techniques

The major addition to the inductance probe technique described in Chapter Three and used for the determination of transition temperature (T_c) and percent-

age of superconducting volume (S) was the provision of an external magnetic field surrounding the measurements coil. This necessitated the use of a specially shaped cryostat to which reference has been made in Chapter Three Figure 3.2. For the present measurement however the coil had to be located at position B corresponding to the centerline of either the electromagnet or solenoid used. For medium and high field examination a Newport Type A magnet was used; this had a pole diameter of 6 cm; a pole separation of 6 cm and gave fields from 30 gauss to 4000 gauss. This electromagnet was not suitable for the precise control of very low fields because of the residual magnetization of the pole piece. Because of this a solenoid system (a Helmholtz pair) was used. The diameter of each solenoid was 12 cm and the separation between the two coils was 7.5 cm so as to produce a uniform field over a volume of about (3 cm^3). This was consideriably larger than the volume of the measurement coil, 1.4 cm^3. With the Helmholtz pair a field of between zero and 170 gauss could be obtained. With either these arrangements the inductance of the probe coil could be measured as a function of magnetic field at different temperatures. Further, by steadily increasing the magnetic field to a certain value and then decreasing it again to zero the hysteresis characterictics could be explored.

4.3 Results and Discussion.

For the measurement of critical field the technique adopted was firstly to cool the inductance probe (filled with superconducting specimen) to 77K. This normally pro-

duced (if the sample were superconducting) a drop in inductance of the form described in Chapter Three. In the second stage of the experiment the sample temperature was kept constant, e.g at 77K and the inductance was monitored as the magnetic field was increased from zero upwards. The first result is shown in Figure 4.2. which refers to specimen 5A, a sintered pellet. This shows a very marked rise from the initial 77K value of 107.60mH at zero field to about 110.70mH for a field of only 100 gauss. It must be remembered here that the room temperature value of the inductance of the coil with superconductor was 112.60mH. The main features revealed are that: there is a substantial rise at low field followed by a steady slow rise to the maximum field (4000 gauss). At this maximum field the inductance is still significantly less than the room temperature value. This shows that there is a critical field H_{c_1} which can be observed but which would require provision of controlled low fields in order to examine it in detail. By recording the inductance values with successively increasing and decreasing magnetic field values hysteresis effects were observed. Starting at zero field the plot followed the line 1 and on reversing the field direction followed the line 2 which, for fields between about 3500 gauss to 100 gauss, gave slightly smaller values of inductance. On repeating the field cycling, lines 3 and 4, no further hysteresis was detected which this magnet system. At low fields i.e below about 100 gauss, all the lines appear to be superimposed but the resolution was not good because of the difficulty of obtaining low fields.

In the next series of experiments the same general technique was adopted but the electromagnet was replaced by the Helmholtz pair and attention was concentrated on

ROOM TEMPERATURE VALUE

INDUCTANCE (mH)

+ —>	1
x <—	2
. —>	3
o <—	4

MAGNETIC FIELD (G)
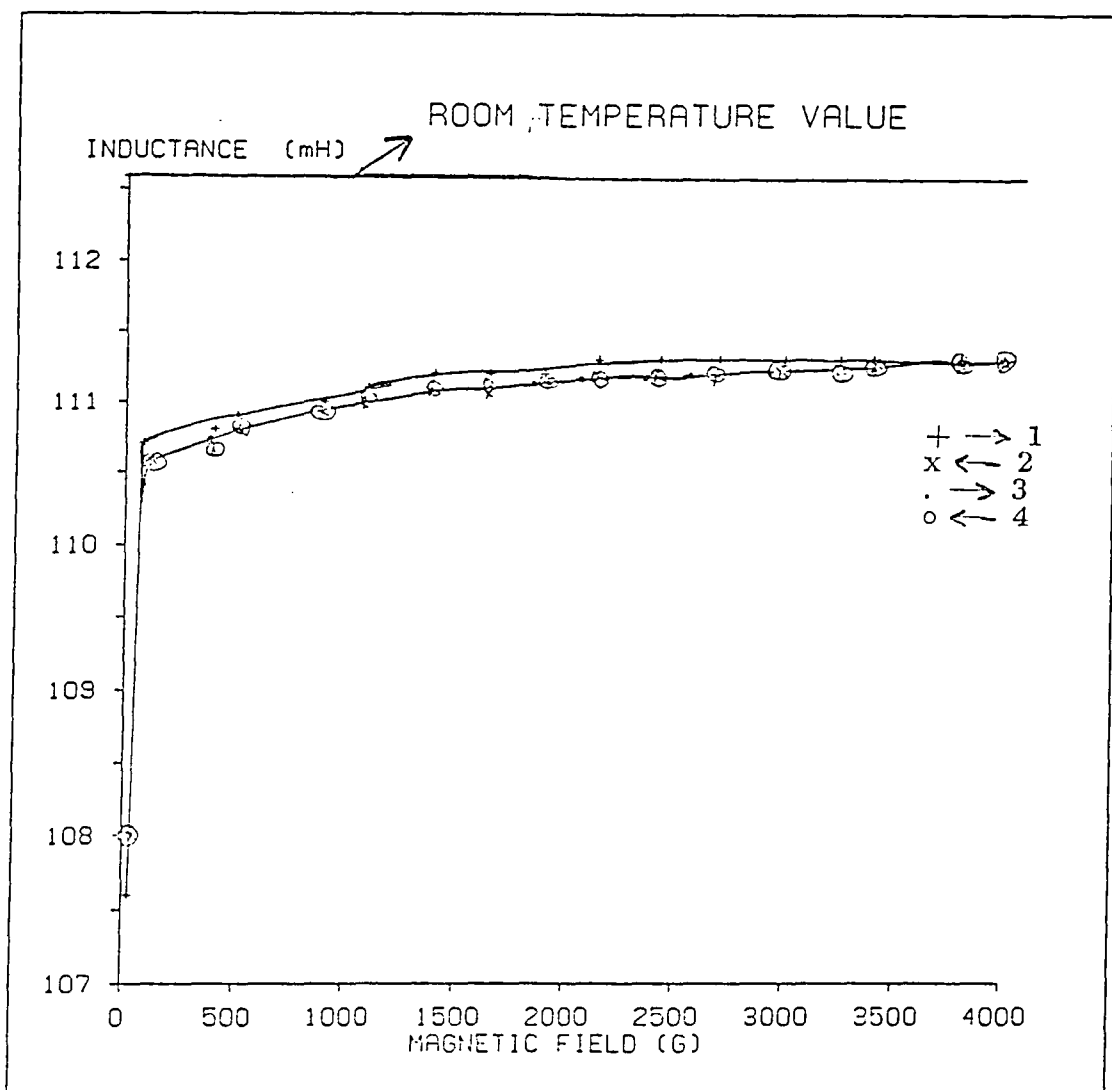
Figure 4.2: Variation of inductance with field for specimen 5A sintered pellet; 77K

the low field region only. Figure 4.3 gives data, also at 77K, for the same sample, 5A

sintered pellet. The general features seen in Figure 4.2 are repeated but here with

much greater resolution. Thus on the initial plot, line 1, the initial rise is complete

at 18 gauss which suggests that H_{c_1}=18 gauss. The initial hysteresis is very evident

because line 1 and line 2 are well separated, even in the low field region between 100

gauss and zero gauss which could not be resolved using the larger magnet. Again the

hysteresis is lessened by field cycling, lines 3 and 4. The evidence from Figure 4.2

suggests that the variation of inductance with field above about 1500 gauss is small.

This would indicate a value of H_{c_2} far in excess of the 4000 gauss obtainable here

because at 4000 gauss the inductance is still much below the room temperature value.

Two other sintered pellets 3A and 7A were also examined in a similar manuer.

Specimen 3A was a sintered pellet of the same nominal composition as 5A but con-

taining a larger amount of iron impurity. In specimen 5A on other hand attempts

had been made to promote grain growth. As regards 3A the low field data is shown

in Figure 4.4. Although the general features are very similar to those found in Figure

4.2. there are some noticable differences. Starting from zero field there is again, line

1, a rapid rise to point A which suggests an H_{c_1} value of 15 gauss. This is followed

by a region extending to point B at 50 gauss where the rate of increase of induc-

tance with field is lower though still marked. After point B there is a small rise in

inductance similar to that observed over the corresponding field range with sample

5A. After field reversal, line 2, hysteresis is observed and this is more pronunced than

for 5A. Further field cycling, line 3 and line 4, also shows the discontinuities at the
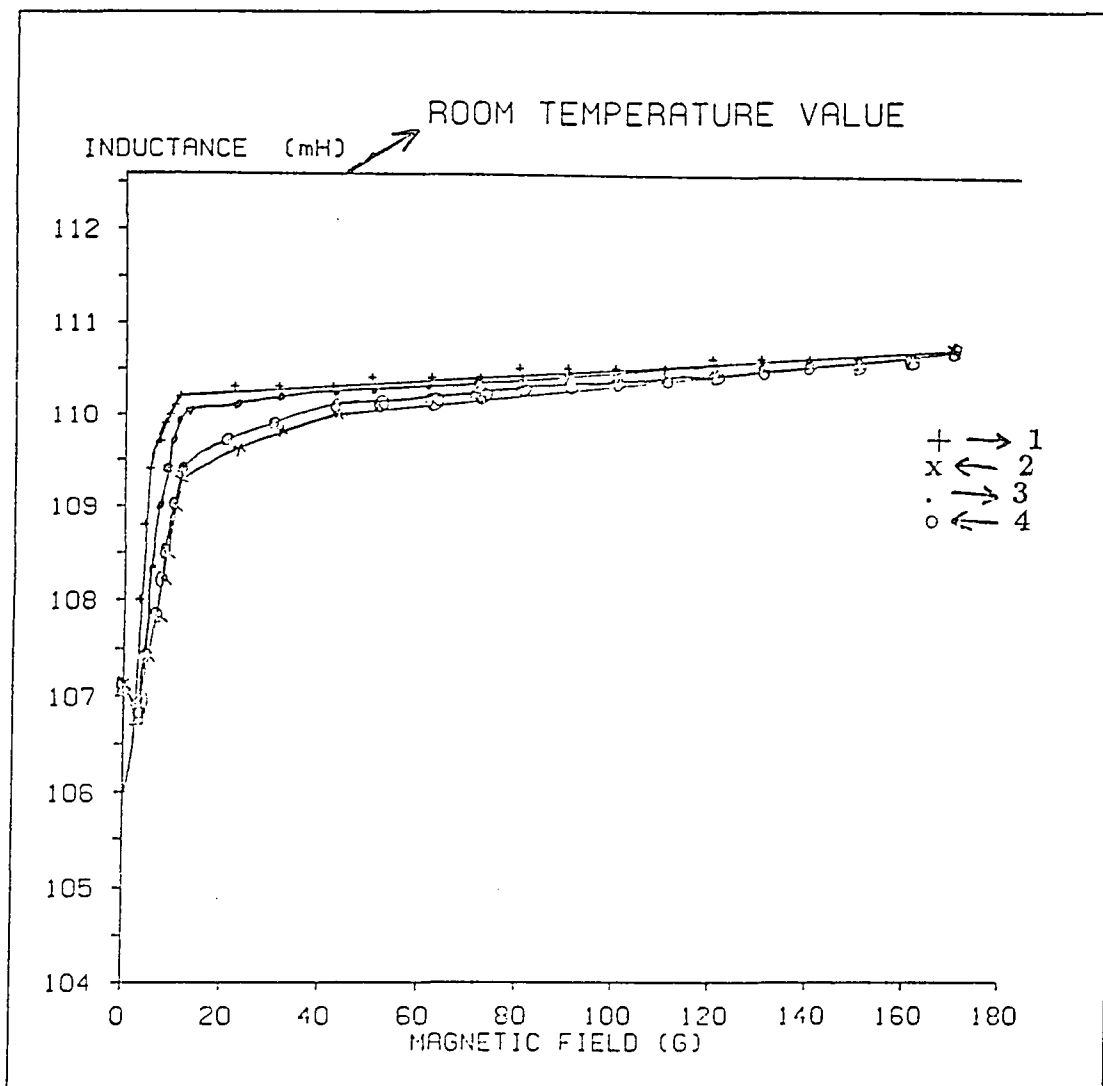
Figure 4.3: Low field variation of inductance with field for specimen 5A sintered pellet; 77K
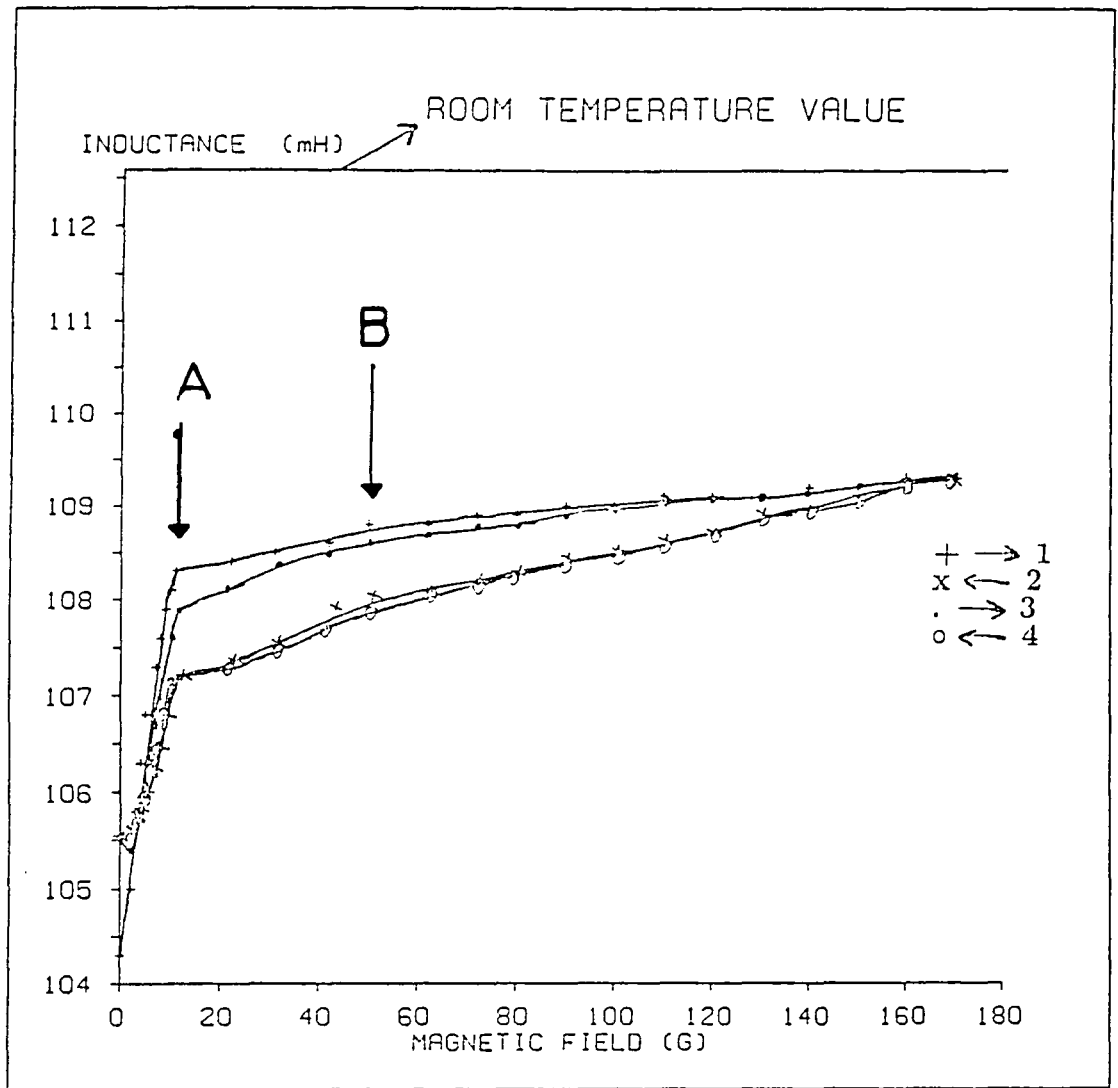
Figure 4.4: Low field variation of inductance with field for specimen 3A sintered pellet; 77K

fields corresponding to point A and point B but gives about the same amount of hysteresis. All the low field inductance-field plots show that at fields greater than 200 gauss the inductance is nearly constant with increasing magnetic field, indicating a very large value of the upper critical field, H_{c_2}. An estimate of H_{c_2} may be obtained from the higher field plot of Figure 4.2. Over the range 1000 gauss to 4000 gauss the inductance changes by at most 0.15 mH given a value of $\frac{dL}{dH}$ of about 5×10^{-5} mH.gauss^{-1}. If the line continued with the same slope until the inductance reached the room temperature value the field required would be about 3×10^4 gauss. This suggests that $H_{c_2} > 3T$. This may be compared with the values quoted by Kobayashi [4.6] of 40T at 77K for sintered pellet and with the values of 60 T at 77K [4.9], Table 4.1(b), for a single crystal.

A possible reason for the occurrence of the two discontinuities at points A and B is that the sample in fact contains two superconducting phases which have different values of H_{c_1}, of 15 gauss and 50 gauss respectively. If this is correct it might be expected that the two phases would also have slightly different values of T_c and hence corresponding discontinuities should be seen in the L-T plot; the temperature resolution in the present L-T technique was insufficient for these to be revealed.

The L-H plot for sample 7A taken at 77K is shown in Figure 4.5. With increasing field the inductance rises very rapidly, line 1, from 97 mH at zero field to 107.50 mH at 14 gauss (i.e $H_{c_1}=14$ gauss) and thereafter increases uniformly and very slowly to the maximum field of 180 gauss. On reversal of the field, line2, no hysteresis is

Author	Form of specimen	parallel to a-b plane	perpendicular to a-b plane	Temperature of measurements
Worthengton et al. [4.7]	single crystal	$H_{c_1} = {} < 50$ gauss	$H_{c_1} = 5000$ gauss	4.2K
Senoussi et al. [4.8]	single crystal	$H_{c_1} = 180$ gauss	$H_{c_1} = 2000$ gauss	77K
Worthengton et al. [4.7]	single crystal	$H_{c_2} = 140$ Tesla	$H_{c_2} = 29$ Tesla	0K
Moodera et al. [4.9]	single crystal	$H_{c_2} = 60$ Tesla	$H_{c_2} = 13$ Tesla	77K

Table 4.1(b): Reported values for H_{c_1} and H_{c_2} in single crystal YBCO.
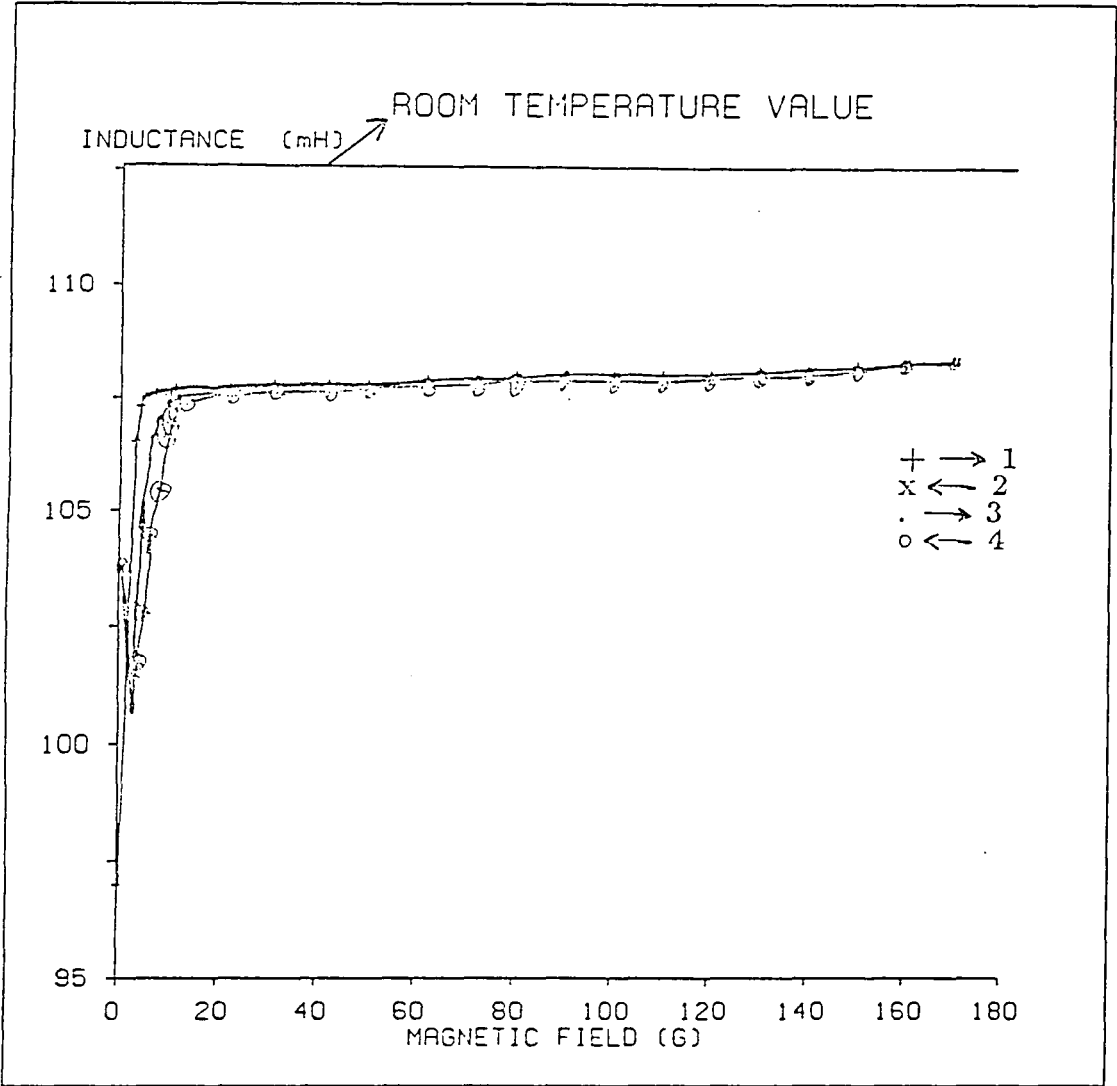
Figure 4.5: Low field variation of inductance with field for specimen 7A sintered pellet; 77K

observed until the field is reduced to below 20 gauss. This is in marked contrast to the large degree of hysteresis seen in the previous sample 3A, Figure 4.4. Further cycling of the field, line 3 and 4, produced substantially the same variation.

Among the specimens examined sample 7A was exceptional in that it had the highest observed critical temperature of T_c=124K. It was thus possible, even with the restriction of the 77K cryostat, to make L-H measurements at different temperatures below T_c. One such result, taken at 90K, is shown in Figure 4.6. Here again the mean feature is the rapid rise in inductance between about 5 gauss and 14 gauss followed by an extended very slow rise to the maximum field of 180 gauss. This gaves a lower critical field value of H_{c_1}=14 gauss. However in the very low field region below 10 gauss the inductance falls to a minimum value of 101mH and rises to 104mH at zero magnetic field. Comparison of Figure 4.5 (taken at 77K) and Figure 4.6 (taken at 90K) for the same sample shows that the zero field values of inductance at the two temperature are different. At 77K the inductance is L=97 mH giving a percentage of superconductor S of $S_{77} = 25\%$; at the higher temperature of 90K the inductance has increased to 104 mH showing that S has now decreased to $S_{90} = 18\%$. The rise in temperature of 13K from 77K towards T_c has thus produced a decrease in the percentage of superconducting volume of the specimen of about 7%. Since both measurement temperatures were well below the critical temperature of 124K it seems likely that this corresponds to changes in penetration depth. This hypothesis was examined as follows. For a conventional Type II superconductor, as described in Chapter One, the penetration depth λ varies with temperature according to the
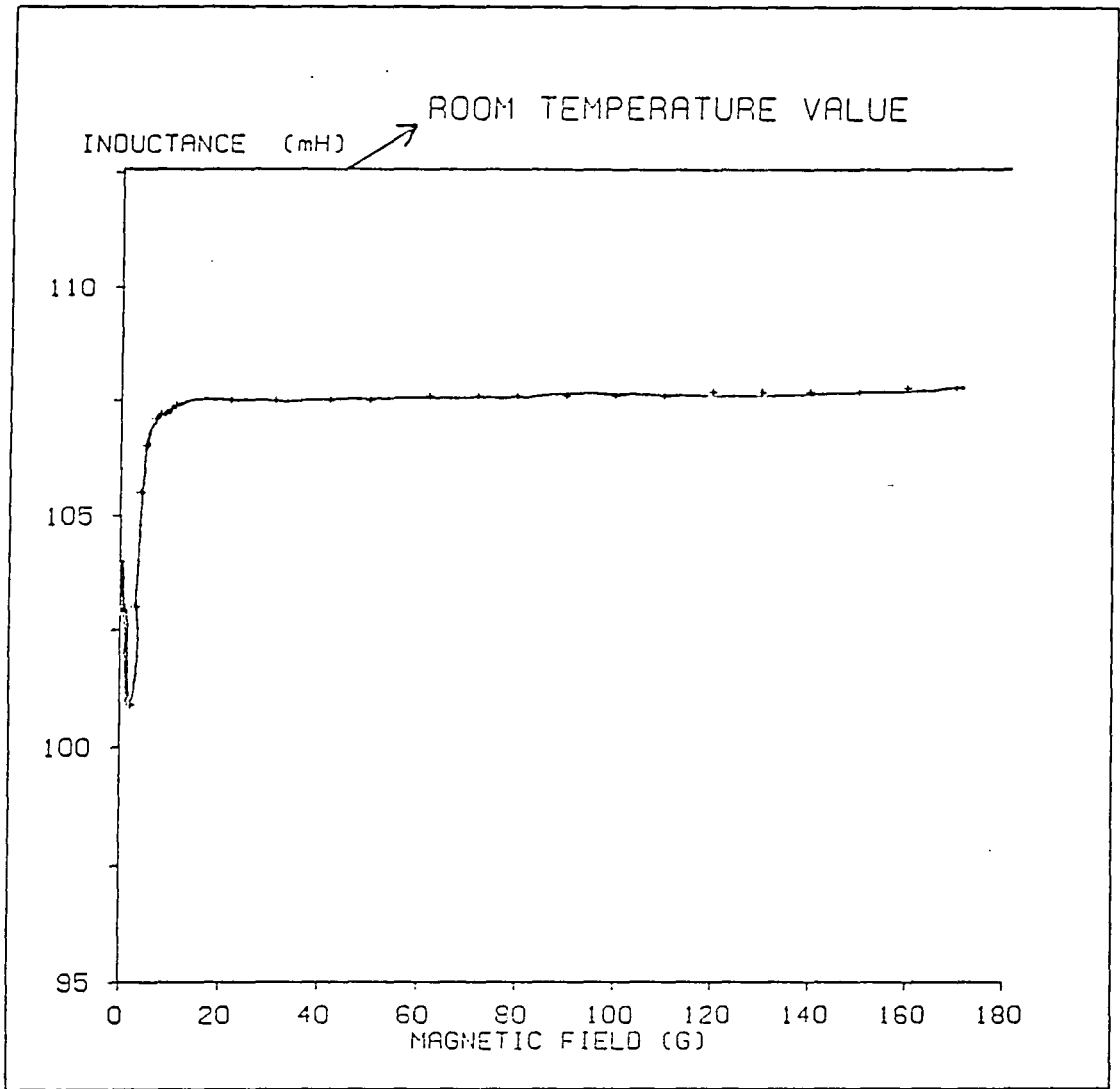
Figure 4.6: Low field variation of inductance with field for specimen 7A sintered pellet; 90K

relation

$$\frac{\lambda(T)}{\lambda(0)} = \left[1 - \left(\frac{T}{T_c}\right)^4\right]^{-\frac{1}{2}} \tag{4.1}$$

Assuming that this expression also holds for YBCO the variation of λ with tempera-

ture can be estimated by inserting the appropriate values of T and T_c. This gave at

77K

$$\lambda_{(77)} = 1.08\lambda_{(0)}$$

and at 90K

$$\lambda_{(90)} = 1.17\lambda_{(0)}$$

where $\lambda_{(0)}$ is the value of the penetration depth at absolute zero. The percentage

change in penetration depth in going from 77K to 90K is thus 7.5%. This is in

excellent agreement with the observed changes in inductance and in superconducting

volume.

REFERENCES

4.1. S.N.Song, Q.Robinson, D.I.Johnson and J.B.Ketterson. Solid State Commu. 68, 391, (1988).

4.2. T.R.McGuire, T.R.Dinger, P.J.P.Freitas, W.J.Gallagher, T.S.Plaskett, R.L.Sandstrom and T.M.Shaw. Phys. Rev. B36, 4032, (1987).

4.3. J.G.Perez-Ramirez, K.Baberschke and W.G.Clark. Solid State Commu. 65, 845, (1988).

4.4. Cao Xiaowen, Zhang Tingyu and Han Guchang. Solid State Commu. 68, 1091, (1988).

4.5. R.S.Rubins, John E.Drumheller, Stuart L. Hutton, Gerald V. Rubenacker, D.Y.Jeong and T.D.Black. J. Appl. Phys. 64, 1312, (1988).

4.6. Kobayashi High Temperature superconductors: Conference Proceedings. Feb. (1988)

4.7. T.K.Worthington, W.J.Gallagher and T.R.Dinger. Phys. Rev. Lett. 59, 1160, (1987).

4.8. S.Senoussi, M.Oussena, G.Collin and I.A.Campbell. Phys. Rev. B 37, 9792, (1988).

4.9. J.S.Moodera, R.Meservey, J.E.Tkaczyk, C.X.Hao, G.A.Gibson and P.M.Tedrow. Phys. Rev. B 37, 619, (1988).

4.10. P.Pureur and J.Schaf. J. Magn. Magn. Mate. 69, 215, (1987).

4.11. C.P.Bean Rev. Mod. Phys. 31, 36, (1964).

CHAPTER FIVE

E.P.R STUDIES ON YBCO

E.P.R forms a very powerful technique for the study of the local environment of particular atoms in a unit cell. In this respect it is complimentary to x-ray diffraction and has often been used in this way in the detailed study of many materials. In x-ray diffraction the basic mechanism is that x-rays interact with the electrons surrounding the atoms; thus some interaction would be expected with every type of atom though the magnitude of the interaction depends on the atomic scattering factor. In e.p.r on the other the interaction is of a different kind. The electromagnetic wave (often in the microwave frequency region) interacts with the magnetic moment generated by the electrons in a particular atom. The technique can therefore only detect ions which have a magnetic moment but despite this limitation the technique it is applicable to many species. The ability of e.p.r to provide information on local atomic environments arises because the energy levels formed by the particular ion, when placed in magnetic field, are determined by the crystal field generated by the surrounding ions which in turn depends on the charges and positions of these surrounding ions.

5.1. Principles of Electron Paramagnetic Resonance

5.1.1. General

Electron Paramagnetic Resonance (EPR) is a technique employing electromagnetic radiation to determine the separation of energy levels in atoms and ions. If energy equal to the separation energy is supplied to the atoms then their electrons absorb it and are excited from a lower to a higher level. Thus observation of the resonant frequencies at which absorption occurs yields information about the energy levels of the atoms and ions.

In EPR the energy is supplied in the form of microwave radiation of frequency often about 9GHz; this does not necessarily correspond to the energy separation of neighbouring levels, but rather to the energies by which a single degenerate level may be split. The application of a strong external d.c magnetic field (Zeeman splitting), the interactions of electrons with nuclear spin magnetic moments and the crystalline electric field due to surrounding atoms are all causes of such splitting. Hence evaluation of splitting energies may yield information about the local environment of the ion.

Electrons in all materials may be considered as possessing two types of motion: motion around the nucleus of the atom giving rise to orbital angular momentum and motion of the electron spinning about its own axis giving rise to intrinsic spin angular momentum. Since electrons have charge, both these angular momenta produce mag-

netic moments, so a free electron will behave like a magnetic dipole with a tendency to align with the direction of an applied field.

However, in some materials all the electrons are arranged in pairs of opposing spins so there is no net magnetic moment to interact with an applied field or with the incident electromagnetic radiation. Thus useful information can be gained only from ions where there is an unpaired electron giving rise to a residual magnetic dipole moment, i.e. from paramagnetics or the exchange coupled systems found in ferromagnetic materials. In these atoms the dipole moment interacts with the magnetic component of the electromagnetic radiation absorbing energy.

There are several classes of materials in which unpaired electrons may exist: some transition metals and rare earth compounds have an unpaired electron in the incomplete d or f orbital; free radicals leave a bonding electron associated with only one atom; F-centres have electrons or holes trapped at point defects; some atoms and molecules possess an odd number of electrons and in metals and semiconductors the conduction electrons can cause paramagnetism. In such materials the allowed energy level of the unpaired electron may be shifted and split by its interaction with electric and magnetic fields.

For paramagnetic ions distributed substitutionally in a diamagnetic host lattice the magnetic properties of the material are essentially those of the paramagnetic ions, modified from the free ion situation by the influence of the crystalline electric field arising from the host lattice. The resultant splitting is known in the absence of an ex-

ternal magnetic field as the zero field splitting. However the application of a magnetic field produces Zeeman splitting of each of the Kramers doublets. An example is given in Figure 5.1 which refers to the Fe/MgO system; (this example has been chosen because some e.p.r studies on doped MgO are discussed in later Chapters of the Thesis). In the doped MgO system at room temperature fields of about 400mT cause splitting by energy separations comparable to that of the microwave radiation. Iron enters the MgO lattice as Fe^{3+} which has a spin of S=5/2. Consequently the multiplicity (2S+1) is six giving the six levels shown in the Figure 5.1; there is some curvature of the levels in low fields but then they diverge almost linearly. The transitions observed at 9GHz are indicated by the vertical lines. The experimental spectrum, i.e. a plot of absorption versus magnetic field consists of a series of lines, each at a characteristic field value and having different intensities which depend on the quantum numbers of the levels from which the particular transition originated. While many e.p.r spectra are observable at room temperature, some signals (e.g. Fe^{2+}) may be detected only at liquid nitrogen (77K) or even liquid helium (4K) temperatures. The materials may be in single crystal, sintered polycrystalline or powder form, but the two latter groups require much more complex interpretation and also present difficulties in experimental handling, particularly at low temperatures.

For power absorption to occur the energy of the incident radiation must exactly match that of the energy separation of the split level, i.e., in classical terms, resonance occurs. To achieve this condition experimentally, it is more convenient to keep the microwave frequency fixed and to vary the energy level separations by variation of
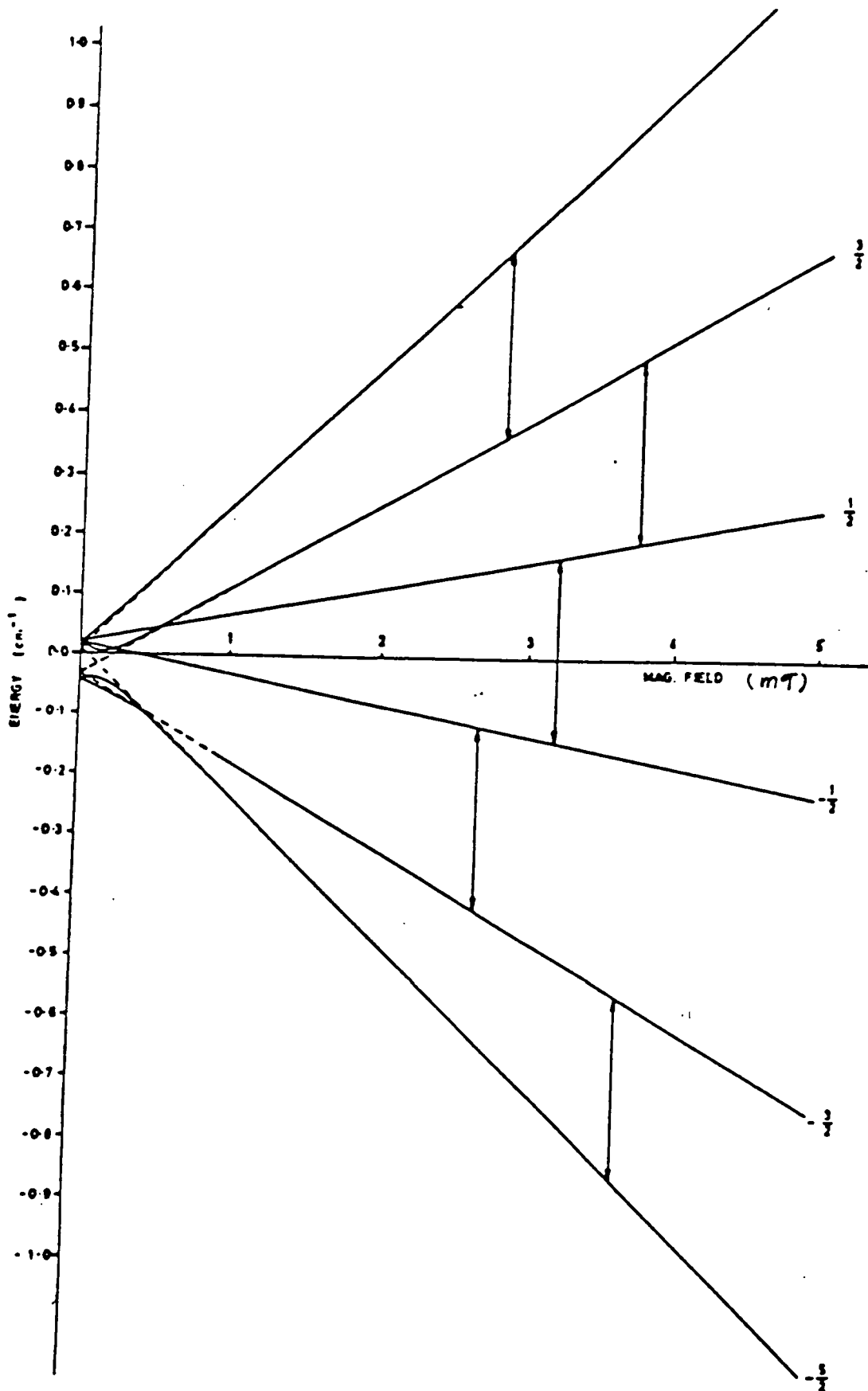
Figure 5.1: Energy levels in the Fe^{3+} ion in MgO.

$$P_s = \frac{1}{2}\frac{h}{2\pi}$$

the external magnetic field.

Thus e.p.r sepctra may contain information about the charge state, type of binding, the symmetry of the enviroment of the paramagnetic centres present in the material and, if present, the amount of hyperfine interaction with surrounding nuclei. Additionally comparison with theoretical free electron behaviour gives an indication of crystal field strength and degree of spin-orbit coupling. Finally, since the area under an absorption line is proportional to the number of unpaired spins, EPR can be used as a method of determining paramagnetic ion concentrations.

Overall, EPR is a powerful tool for the study of paramagnetic centres and can detect very low concentrations.

5.2 Theory Of The Single Free Electron.

All signals detected by e.p.r must have an unpaired electron whose particular environment is determined by its difference from the theoretical single free electron as defined below.

Quantum Theory states that the angular momenta and hence magnetic moment of an electron may hold only certain discrete values. In the simplest case of a single free electron there can be no orbital angular momentum, and the only allowed value of spin angular momentum is given by:

$$P_s = \frac{1}{2}\frac{h}{2\pi} \qquad (5.1)$$

and the corresponding magnetic moment by:

$$\mu_s = \frac{eh}{4\pi mc} = \beta \tag{5.2}$$

where e and m are charge and mass of the electron and h and c are Planck's constant and the speed of light respectively. β is the Bohr magneton, the unit of magnetic moment.

If an external magnetic field, H_o, is applied the electron experiences a torque which tries to align its magnetic moment vector, $\underline{M}$, with the direction of the field. However, quantisation restricts the possible orientations of the vector, so the torque forces the magnetic moment to precess around the field at an angular frequency, ω_o, independent of orientation and given by:

$$\omega_o = \gamma H_o \tag{5.3}$$

where γ is the gyromagnetic ratio (the ratio of magnetic moment to angular momenta) and has the value 17.6×10^{10} s$^{-1}T^{-1}$ for a free electron. This is illustrated in Figure 5.2

The energy (E) of the magnetic dipole moment(μ) is dependent on orientation with respect to the applied field and is given by:

$$E = \mu H_o cos\theta \tag{5.4}$$

where θ is the angle between the magnetic field and the axis of the dipole. In the case of the free electron there are only two allowed orientations of the magnetic moment
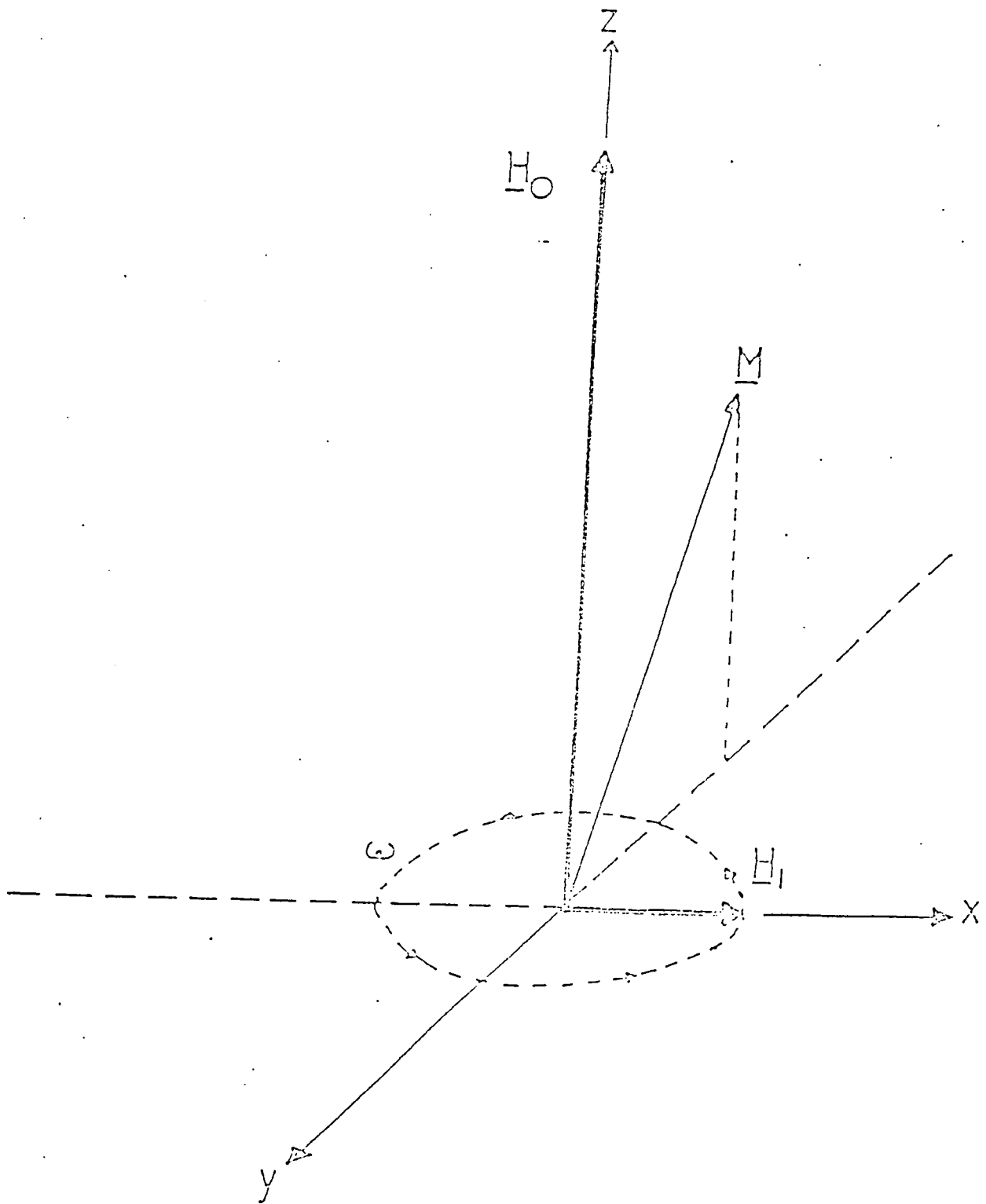
Figure 5.2. Precessing electron moment.

corresponding to spin-up and spin-down (there being no orbital magnetic moment) and thus equation 5.4 becomes:

$$E = M_s \beta H_\circ \qquad\qquad (5.5)$$

where M_s are the magnetic quantum numbers of the allowed energies, i.e. $M_s = \pm 1/2$. Thus the applied field has split the energy level into two levels separated by energy $2\beta H_\circ$, i.e. the ground state has a two-fold degeneracy lifted by $H_\circ$. In general, i.e. for all systems, equation 5.5 becomes:

$$E = g \beta H_\circ \qquad\qquad (5.6)$$

where g is a numerical factor determined experimentally. Making relativistic corrections to the above theory g for a single free electron is 2.0023.

5.3 The Paramagnetic Ion In The Crystalline Environment.

A free ion has spin and orbital angular momenta assigned by quantum numbers S and L respectively. The total angular momentum has a quantum number J which is the vector sum of L and S. Quantum theory states that the ground state of such an ion has degeneracy of $(2J+1)$ in the absence of an applied magnetic field.

However, the strong crystalline electric fields may modify the quantum state by breaking the coupling between L and S, i.e. quenching, thus causing ground state degeneracy due to S alone of $(2S+1)$. The higher orbital states are usually

far removed from the ground state by energies corresponding to quanta of optical frequency radiation.

The crystal field also causes a lifting of the degeneracy of the ground state by energies corresponding to microwave quanta (or less). This lifting is limited by Kramer's Theorem which states that an ion with an odd number of unpaired electrons must retain two-fold degeneracy of these levels.

In reality the spin-orbit coupling is not completely broken and so the degeneracy of the ground state does not correspond to the true spin quantum number of the free ion, but to an effective spin quantum number, S', corresponding to an observed degeneracy of $(2S'+1)$. The application of a magnetic field causes further lifting (see Figure 5.1 and equation number 5.6):

$$E = g\beta H_\mathrm{o} M \qquad (5.7)$$

where M is the quantum number (between S and S') and g is the spectroscopic splitting factor. The deviatation of this quantity from the free electron value of 2.0023 is a measure of orbit quenching (i.e. spin-orbit coupling).

Similarly elementary theory also suggests that only transitions for spin state separations of $\triangle M = 1$ may be seen. Since the crystalline field breaks down the pure spin states, this rule may be broken and so-called "forbidden transitions" may be seen, e.g. for an ion of $S'=3/2$ (e.g. Cr^{3+}) an energy level, $|i>$, may be described with eigenvectors a_i, b_i etc.:

$$|i>= a_i|3/2> +b_i|1/2> +c_i|-1/2> +d_i|-3/2> \qquad (5.8)$$

68

where the eigenvectors are normalised by:

$$|a_i|^2 + |b_i|^2 + |c_i|^2 + |d_i|^2 = 1 \qquad (5.9)$$

5.4. The Spin Hamiltonian and Energy Levels.

The Hamiltonian Operator is a convenient description of the energy of an atom containing unpaired electrons and nuclei with non- zero spins.

$$H = H_{el} + H_{CF} + H_{LS} + H_{SS} + H_{Ze} + H_{Zn} + H_{II} + H_{HF} \qquad (5.10)$$

The first three terms comprise the atomic Hamiltonian and the last six form the spin Hamiltonian. The operator H_{el} accounts for electron kinetic and potential energy and electron-electron repulsion, and is not seen in microwave spectroscopy. The crystalline field operator H_{CF} is also too great to be detected directly by microwave frequencies, but represents energies which have a strong influence on the magnitude of spin Hamiltonian parameters. It has the general form:

$$H_{CF} = -eV(x_i, y_i, z_i) \qquad (5.11)$$

where V is the potential of the crystalline field and x_i, y_i, z_i are the co-ordinates of the ith electron of the unfilled shell.

The spin -orbit operator H_{LS} is proportional to the dot-product of the spin and orbit vectors, and forms part of both the atomic and the spin Hamiltonian:

$$H_{LS} = \lambda \underline{L}.\underline{S} \qquad (5.12)$$

where λ is the spin-orbit coupling constant.

These energies are much smaller than the H_{CF} energies, and may be seen in microwave spectroscopy. However, if the resultant angular momentum of the ion is zero (i.e. S ground state as opposed to S' ground state) then H_{LS}=0.

The general spin-spin operator H_{SS} is given by:

$$H_{SS} = -\rho(\underline{L} - \underline{S})^2 + 1/2(\underline{L}.\underline{S}) - 1/3L(L + 1)S(S + 1) \qquad (5.13)$$

and represents energies of magnitude similar to the electronic Zeeman (magnetic field splitting) operator, H_{Ze}, which is given by equations 5.6 and 5.7 or:

$$H_{Ze} = g\beta_n\underline{H}.\underline{S} \qquad (5.14)$$

The equivalent nuclear Zeeman term H_{Zn} is given by:

$$H_{Zn} = g\beta_n\underline{H}.\underline{I} \qquad (5.15)$$

where β_n is the nuclear Bohr magneton and I the nuclear spin quantum number. The nuclear spin-spin interaction takes the same form as the spin-orbit coupling operator:

$$H_{II} = J\underline{I}.\underline{I} \qquad (5.16)$$

and similarly for the hyperfine operator:

$$H_{HF} = A\underline{S}.\underline{I} \qquad (5.17)$$

However the microwave spectroscopy terms can be collected together in the spin Hamiltonian if the effect of H_{CF} (equation 5.11) is taken into account using the

70

effective spin S':

$$H_s = g\underline{\text{H}}.\underline{S}' + D(S')^2 + S'(S'+1) + H_{Zn} + H_{II} + H_{HF} \qquad (5.18)$$

Thus, using the spin Hamiltonian, the solutions of:

$$H_S|i> = E_i|i> \qquad (5.19)$$

(see equations 5.8, 5.9) may be derived in terms of E_i, the eigenvalues (energies) of

the states $|i>$. (see equations 5.8, 5.9). Further treatments of e.p.r theory are given

in [5.1-5.3].

5.5. Microwave Power Absorption.

To detect the splitting of the electron energy levels, transitions must be excited

between two levels by electromagnetic radiation of frequency, v, such that:

$$hv = g\beta H_{\text{o}} \qquad (5.20)$$

The transition is induced by the oscillating magnetic field component exerting a

torque on the electronic magnetic moment and thus altering its energy. There is

an equal probability of absorption and emission of power on interaction between the

microwave beam and electron; the net absorption relies on there being an excess

population of electrons in the lower level. The relative populations are given by

Boltzmann statistics:

$$\frac{n_1}{n_2} = exp^{-\frac{g\beta H_{\text{o}}}{kT}} \qquad (5.21)$$

71

where n_1 and n_2 are the populations in the upper and lower levels respectively. Power absorption is temperature sensitive and increases as temperature decreases, improving the EPR signal-to-noise ratio. To a first approximation the population difference $n = n_2 - n_1$ between the levels may be expressed as:

$$n = N \frac{g H_o}{2KT} \qquad (5.22)$$

where N is the total population of unpaired spins. Integration of the detected absorption intensity with respect to the varying applied magnetic field gives a measure of the total net power absorbed, P,:

$$P = \frac{2\pi^2 v^2 H_o S(S+1) N g^2 \beta}{3kT} \qquad (5.23)$$

This shows that the power absorbed is proportional to the number of unpaired electrons present in the sample. In practice the levels have a narrow but finite band of energies, and excitations occur over a range of magnetic field values giving an absorption line of finite width.

5.6 Experimental.

Most e.p.r spectrometers operate on similar principles, and here all the measurements were made using a Varian V4502-15 spectrometer in the 9GHz frequency [5.4] region. The block diagram of Figure 5.3 identifies the main components of an e.p.r spectrometer. The physical and engineering principles have been extensively covered by Poole [5.5].
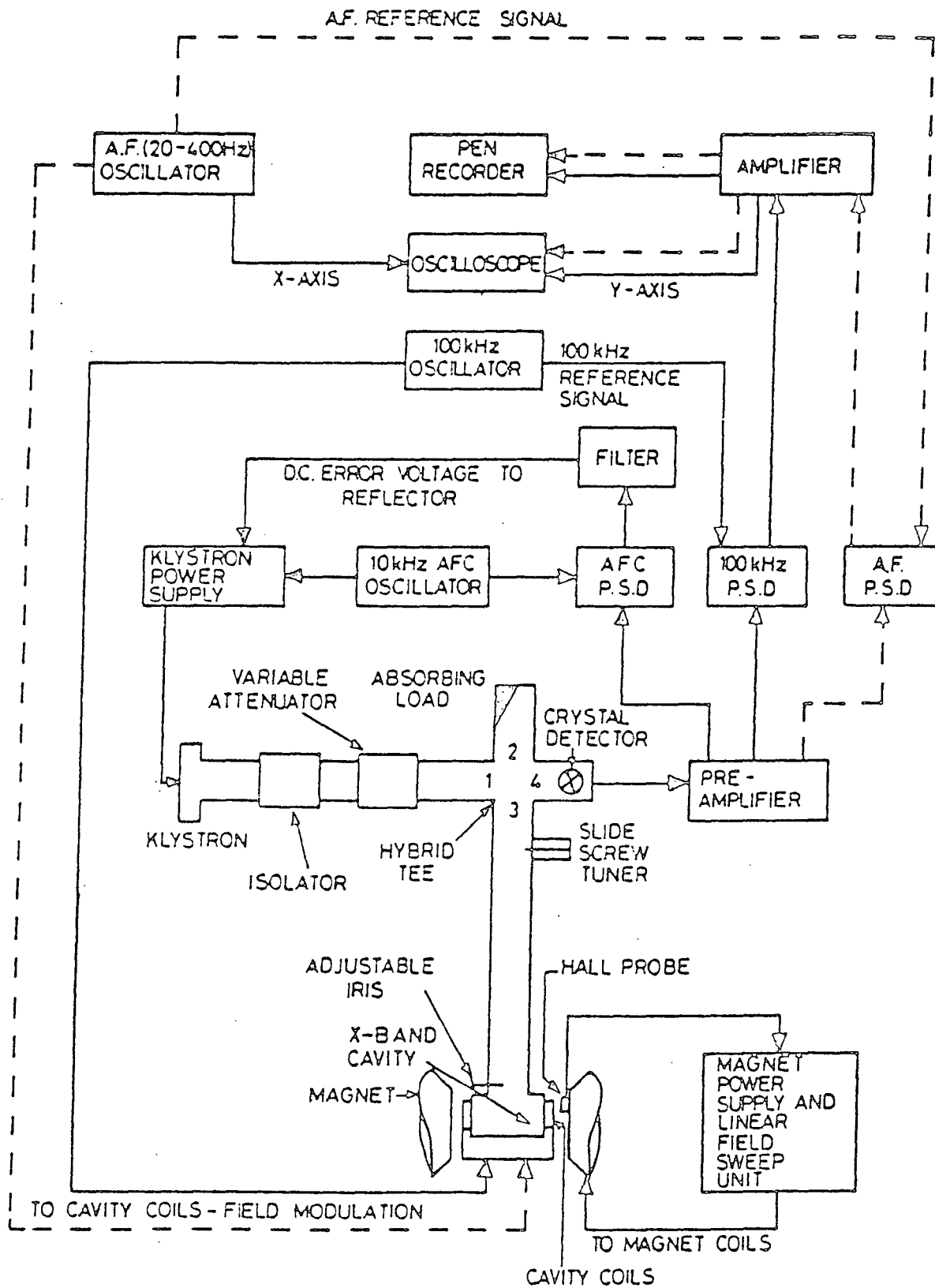
Figure 5.3: General arrangement of EPR spectrometer.

The source of 9GHz microwaves was a klystron. The microwaves passed through an isolater and a variable attenuator to a hybrid-tee (microwave bridge) which has the ability to divide the power equally between arms 2 and 3. Arm 3 is terminated by the microwave cavity and arm 2 is terminated by a matched load.

The e.p.r spectra reported in this work were recorded with samples positioned at the centre of a V4531 cavity operating in the TE_{102} mode. In this mode of operation, the field patterns produced by standing electromagnetic waves in the cavity give the optimum conditions for observing magnetic resonance. The introduction of a dielectric sample, which causes absorption of power, changes the impedance of the cavity, so the microwave circuit must be retuned each time that a new sample is inserted into the cavity.

The klystron frequency is adjusted mechanically and electronically to match the cavity resonance with the sample in position by positioning the cavity absorption dip in the centre of the klystron mode pattern which is displayed on CRO. The cavity resonance frequency was measured with a Hewlett-Packard X532B frequency meter. The crystal detector is located in arm 4. In fact a small amount of current is needed to bias the detector. To provide a bias current, a small probe (called a slide screw tuner) is positioned in arm 2 to reflect a small amount of microwave power to the detector, which causes a current to flow in it.

There is also an automatic frequency control system (AFC) which is shown in the block diagram of Figure 5.3. The AFC phase detector and the klystron reflector

voltage are provided by an oscillator modulated at 10KHz. When the klystron centre frequency (f_o) corresponds to the resonance frequency of the sample cavity (f_r) a 10KHz signal is reflected from the cavity and appears at the crystal detector (see Figure 5.4a). If the centre frequency of the klystron shifted from that of the resonant cavity, a 10KHz voltage appears at the crystal detector. The amplitude of this reflected 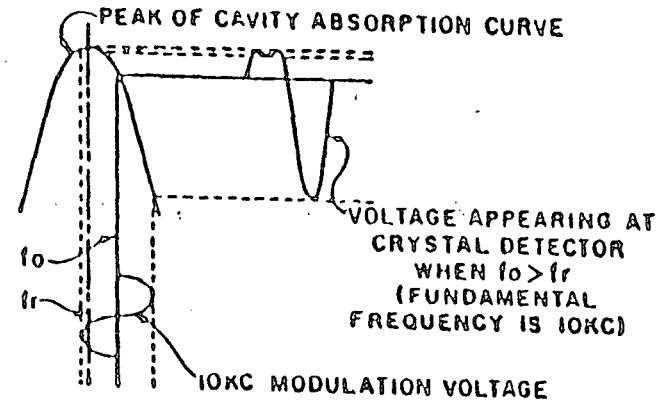10KHz signal will depend on the relative difference between f_o and f_r (see Figure 5.4b and 5.4c). This 10KHz error voltage (it may be considered as an error voltage since its phase and amplitude are dependent on the relationship between f_o and f_r) is phase detected, and filtered to produce a d.c. output voltage which is used to control the klystron reflector voltage.

The d.c. magnetic field was provided by a $'V - 3603 - 12'$ electromagnet. The field in the magnet gap was recorded by a Hall probe attached to one pole face which supplies a control voltage to the magnet's power supply. The magnetic field sweep was calibrated with a Newport Instruments P2 proton magnetometer. The spectra were recorded as first derivatives. To obtain this a 100kHz sine wave modulation was superimposed on the static magnetic field using a pair of small modulation coils. The microwave energy reflected from the cavity while the field is swept through the resonance position is therefore modulated at the same frequency. The phase and amplitude of this modulation is dependent upon the characteristics of the EPR resonance line and the value of the static magnetic field relative to the centre of the resonance line (see Figure 5.5). The microwave energy which is modulated by 100kHz and which contains the EPR signal information falls on the crystal detector.

74

PEAK OF CAVITY ABSORPTION CURVE

VOLTAGE APPEARING AT
CRYSTAL DETECTOR
WHEN fo = fr
(FUNDAMENTAL
FREQUENCY IS 20KC)

fo AND fr

10KC MODULATION VOLTAGE

(a)

PEAK OF CAVITY ABSORPTION CURVE

VOLTAGE APPEARING AT
CRYSTAL DETECTOR
WHEN fo > fr
(FUNDAMENTAL
FREQUENCY IS 10KC)

fo

fr

10KC MODULATION VOLTAGE

(b)

PEAK OF CAVITY ABSORPTION CURVE

VOLTAGE APPEARING AT
CRYSTAL DETECTOR
WHEN fo < fr
(FUNDAMENTAL
FREQUENCY IS 10KC)

fo

fr

10KC MODULATION VOLTAGE

(c)

Figure 5.4: Principle of automatic frequency control system.

EPR RESONANCE LINE

SIGNAL VOLTAGE TO
CRYSTAL DETECTOR
& AMPLIFIER

MODULATION AMPLITUDE

POSITION OF STATIC
MAGNETIC FIELD

Figure 5.5: The 100 kHz modulation technique.

The signal information is carried to the input of the phase sensitive detector. The first derivative EPR signal can be integrated over a long time period in comparison with the time periods of the random input signals (noise) to the phase sensitive detector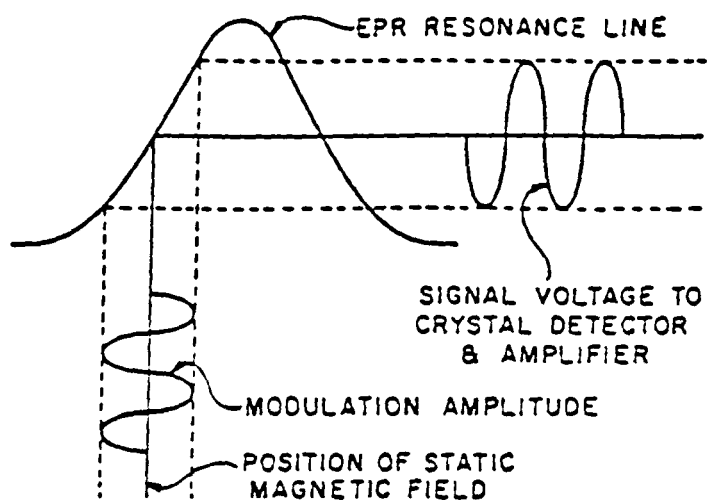. Thus averages can be produced having eliminated almost all of the random (noise) signals, so that only the EPR signal information is recorded with a very high signal to noise- ratio. The signal is traced out on a chart recorder, the trace being a first derivative representation of the original EPR absorption line.

Spectra from both powder and single crystal samples could be obtained with the spectrometer. In the former case the powder samples were contained in spectro-scopically pure quartz tubes, sealed at one end, with internal diameters of 2mm and external diameters of 4mm; typically the sample length would be about 5mm so that the whole of the sample was in a region of the cavity in which the E-H field pattern was constant. For solid or single crystal samples a piece of solid, usually of dimensions about 1mm x 1mm x 5mm was mounted on the flattened end of a silica rod whose position could be raised or lowered to bring the sample to the centre of the cavity. Further discussion of the detailed experimental technique is given in reference [5.6].

5.7 Results.

A number of Yttrium-Barium-Copper Oxide superconducting powders have been examined in the Varian 9GHz e.p.r spectrometer, described above, at room temper-ature. The first group of samples examined were those which had previously been

examined in the inductance probe. These were samples 1A, 2A and 4A. Of these samples 1A showed superconductivity with a sharp transition near 88K, 2A also showed some superconductivity but with a broad transition extending from 100K to 77K but sample 4A did not show any superconducting transition above 77K. The pure YBCO sample 1A was made from spectroscopically pure BaO, Y_2O_3, and CuO; it was a powder. The spectrum is shown in Figure 5.6. It can be seen that there is a large intensity room temperature signal. It extends over a very wide field range from about 275.0mT to about 350.0mT; the line not symmetrical but gave evidence for peaks near 300.0mT with a minimum at 325.0mT (at frequency of 9.334GHz).

The second superconducting sample 2A gave a very different pattern, Figure 5.7. Here only a large intensity symmetrical single line was observed and this was centred at g-value of g=2.5 (i.e. resonance occurred at 300.0mT at a frequency of 9.44GHz); the overall linewidth extended from about 250.0mT to 370.0mT.

The third sample 4A gave a spectrum, Figure 5.8, more similar to that of Figure 5.6. The features (peaks at 300.0mT and 320.0mT) were pronounced and there is also the minimum at 325.0mT. However there is in addition a shoulder near 315.0mT which was not present in either the spectrum of sample 1A or of sample 2A. The overall width of the spectrum was from 280.0mT to 340.0mT.
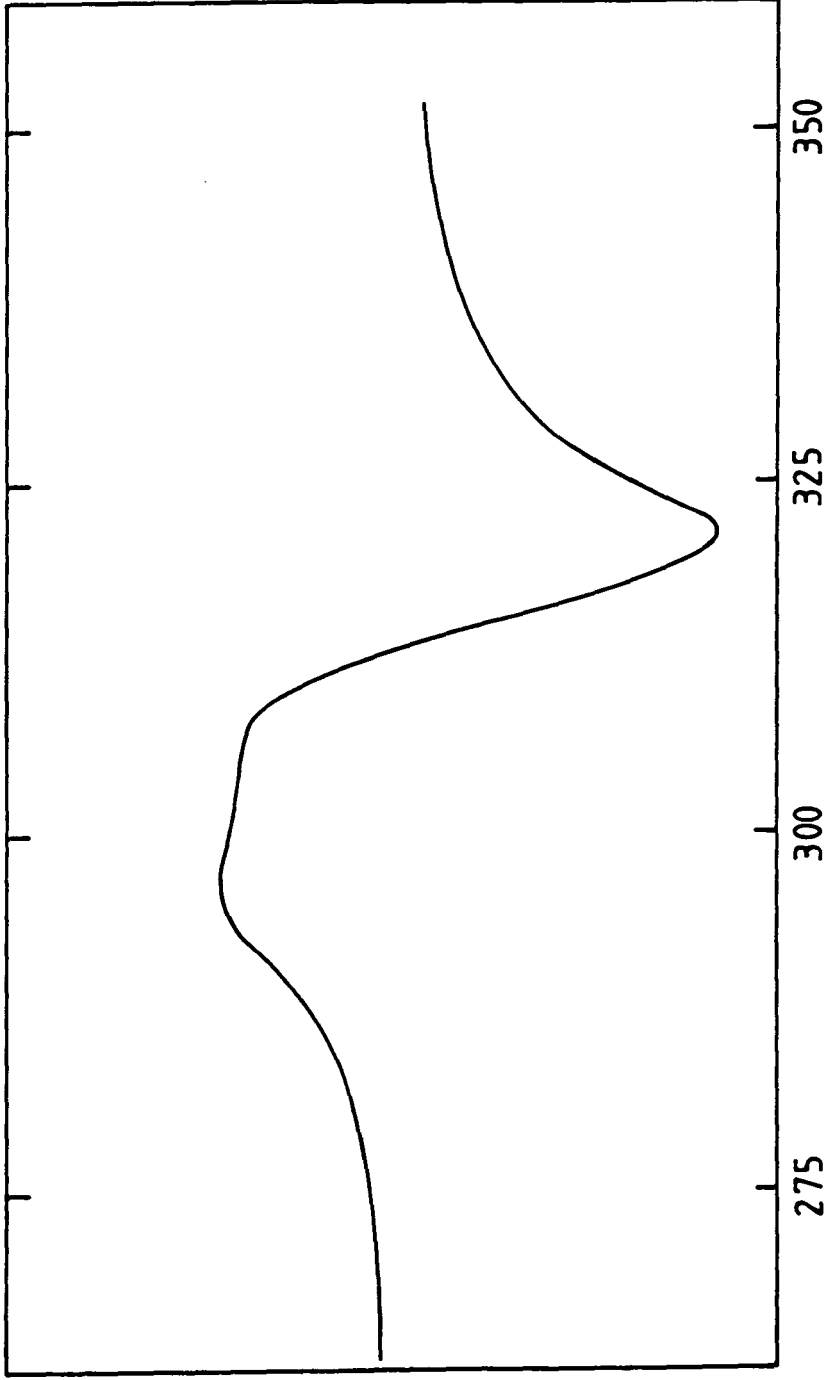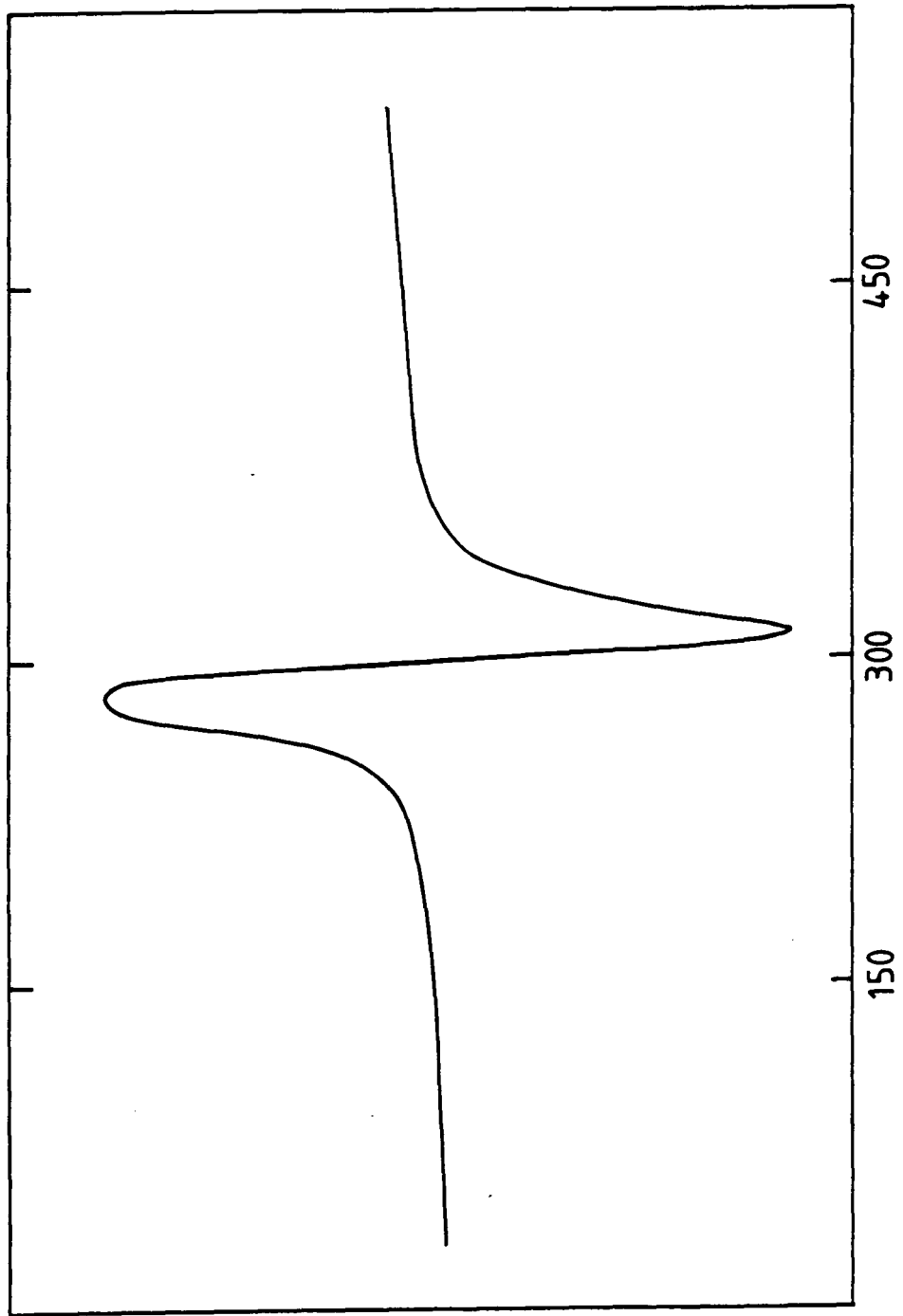
Magnetic Field, (mT)

Figure 5.6. EPR spectrum of specimen 1A; 293K, 9.334 GHz

Magnetic Field, (mT)

Figure 5.7 EPR spectrum of specimen 2A; 293K, 9.440 GHz
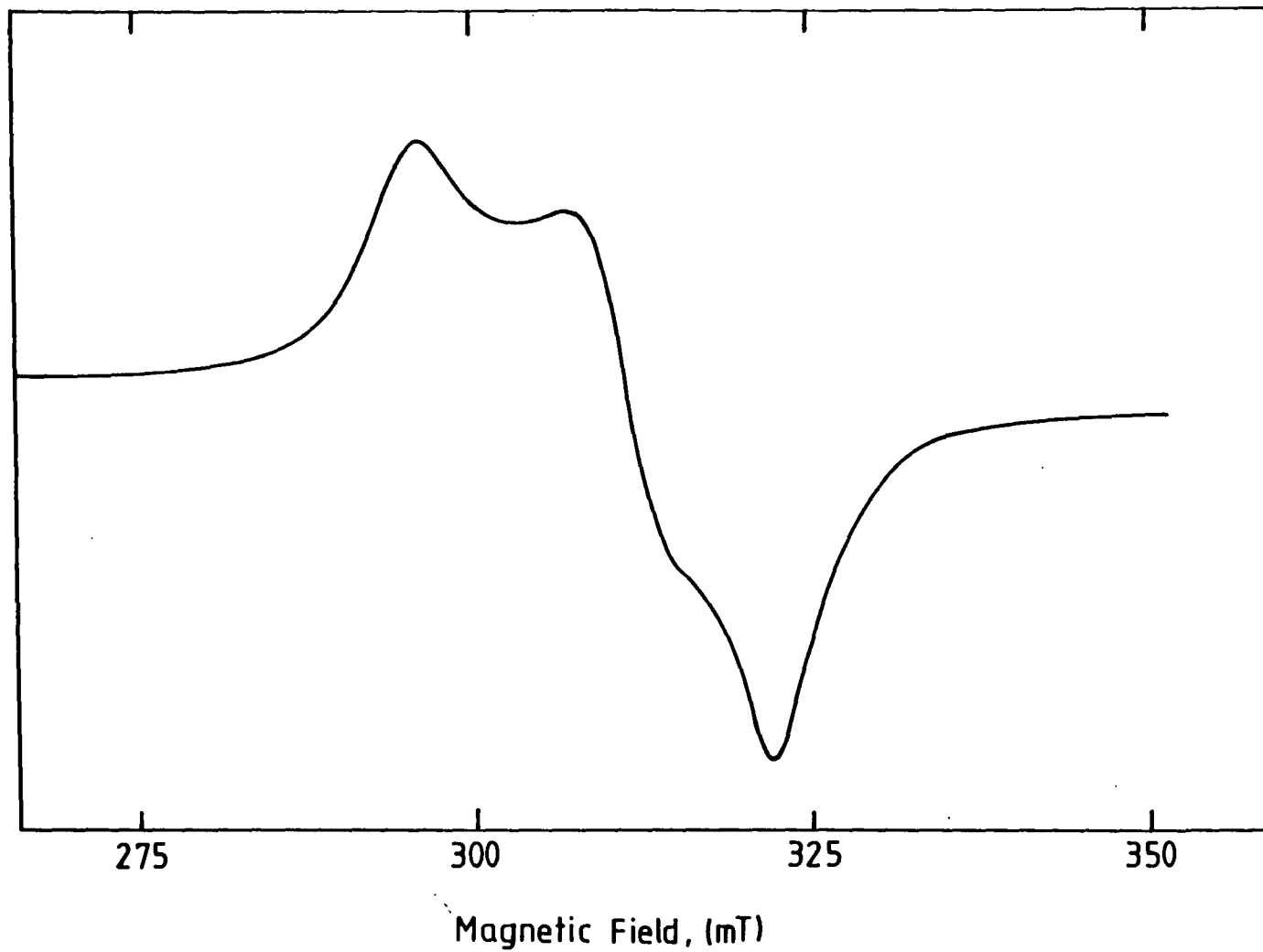
Figure 5.8. EPR spectrum of specimen 4A; 293K, 9.335 GHz

5.8 Discussion.

Electron Paramagnetic Resonance in the high T_c superconductor $YBa_2Cu_3O_{7-x}$ has been studied by several authors, in particular by R.Bartucci et al.[5.7] and G.Amoretti [5.8], who used spectrometers working in the 9GHz region. Further e.p.r examinations in the same frequency range were made by Castillo [5.9], Durny [5.10], Stankowski [5.11] and Mehran [5.12]. In addition some high resolution spectra obtained at Q-band (35GHz) have been reported by Blank [5.13]. Reference is first made to Bartucci et al's work. In this polycrystalline $YBa_2Cu_3O_{7-x}$ samples were prepared and carefully characterized at Istituto di Elettronica dello State Solido del Consiglio Nazionale delle Ricerche. A mixture of Y_2O_3, $BaCO_3$, and CuO in the nominal molar ratio Y:2Ba:3Cu was ground and reacted for 12h in an alumina crucible in flowing O_2 at 900°C. A final heat treatment at 650°C in oxygen atmosphere was given for 12h; thus the specimen was a sintered pellet. Their samples were first characterised by x-ray diffraction which showed that all the peaks in the pattern belong to the orthorhombic phase $YBa_2Cu_3O_{7-x}$. In addition the d.c. resistance versus temperature was measured by the four-probe method. The superconducting transition temperature T_c was 92±0.5K (midpoint of the resistive transition). Above T_c the behaviour of the resistance was metal-like. Bartucci's experimental techniques were very similar to those used here, thus his e.p.r measurements were performed using a Bruker Model ER-200D-SRC X-band spectrometer equipped with an ER4111VT temperature control unit (accuracy ±0.3K). The pellet was inserted in an e.p.r quartz tube which in

turn was placed in a quartz Dewar centred in a TE_{102} cavity. The microwave power was fixed well below the value causing signal saturation. The spectra were taken in the first-derivative mode with a modulation frequency of 100kHz. 1,1-diphenyl-2-picrylhydrazyl (DPPH, g=2.0037) was used as a reference for the g-value and the magnetic field calibration was done by a Magnon precision N.M.R gauss meter.

Several spectra were taken from just below the transition temperature up to room temperature and no change of the line shape or its magnetic field position was ever recorded. A further test was performed dipping the sample in liquid nitrogen and the main e.p.r features were not only still observable but even clearer. The intensity of the resonant signal was certainly changing under temperature increases although at different rates.

Bartucci et al's e.p.r spectra of polycrystalline $YBa_2Cu_3O_{7-x}$ superconductive pellets at 77,90,107,128, and 298K, are reproduced in Figure 5.9. Four equally separated absorption bands can be resolved as is expected when the unpaired electron of the Cu^{2+} ion interacts with the spin I=1/2 of its own nucleus. Although a theoretical simulation would better clarify the experimental line shape, the dip at 3100G may be interpreted as the superposition of two adjacent hyperfine features. The Cu^{2+} hole is in the $d_{x^2-y^2}$ orbital with lowest energy because of tetragonal distortions from octahedral symmetry. The spectrum at 77K is by far the most intense and shows very clearly the shoulder at g_1 while the last two hyperfine features merge together.

Since the spectrum is the envelope of line shapes from all possible orientations
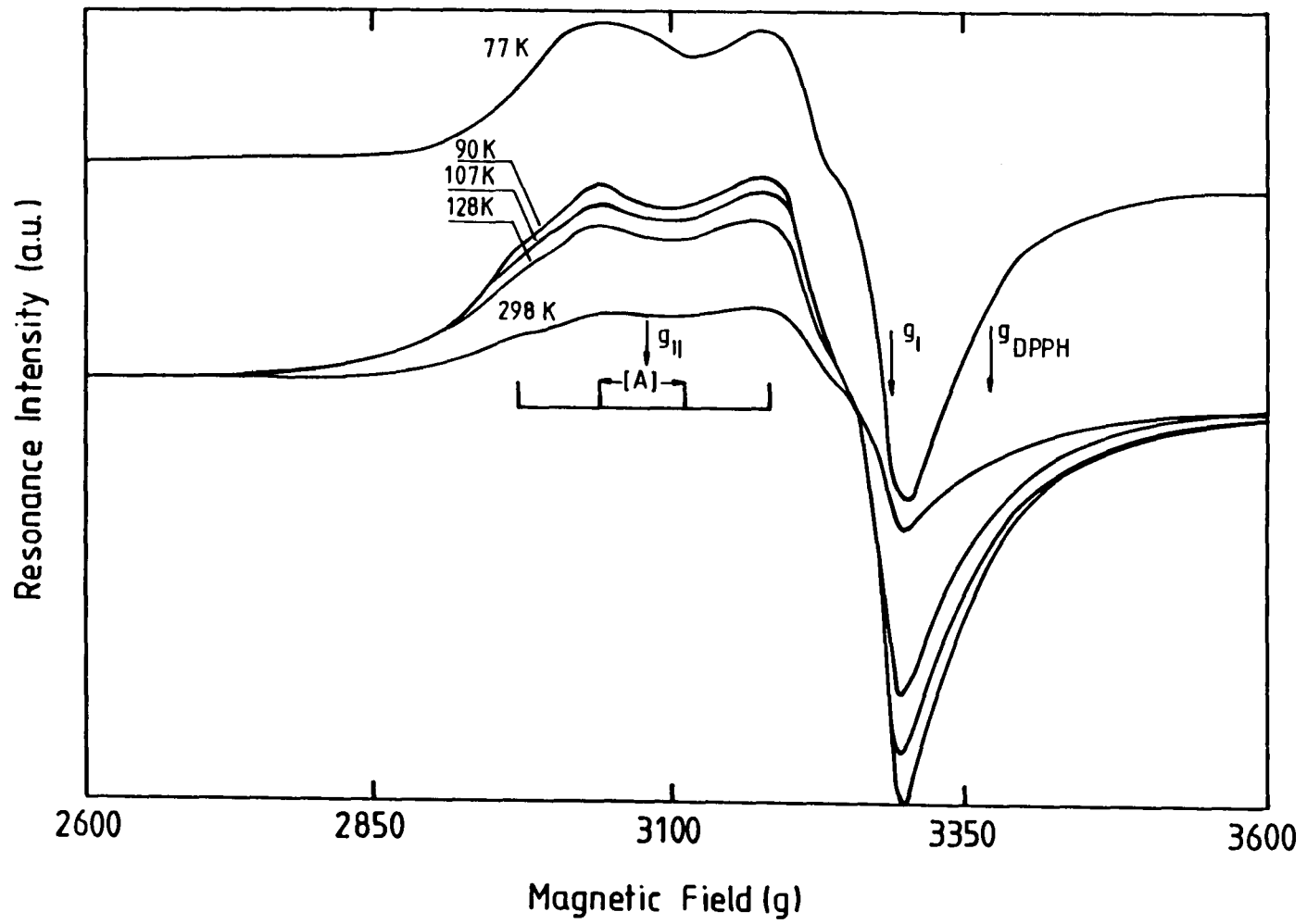
Figure 5.9 EPR spectra of Y13CO powder; (after Bartucci et al)

of the z axis of the paramagnetic microcrystal with respect to the magnetic field, the orientation of the metal-ligand complex in the crystal cannot be determined. Only the mean g splitting and $|A|$ hyperfine factors with respect to the same crystal principal axes can be found. Nevertheless, a large number of bondings is expected to lie in the plane perpendicular to the z axis of the single cupric complex either for the pyramidal or square planar ligand environment and actually a large absorption is observed at higher magnetic fields. The corresponding g–value is about 2.069 which approaches fairly closely the free-electron g value of 2.0023 while the g_{11} value (2.194) is quite different being $g_{11} > g_1$. No hyperfine structure can be resolved in the high magnetic field region while the $|A_{11}|$ component can be estimated to be 72 ± 2G.

A careful inspection of Bartucci et al's measurements shows that the intense negative wing is more symmetric at 77K, the shoulder around g_1 is sharper, and moreover the last two hyperfine features merge together in one broad feature. These are the signs of two different E.P.R signals and of a slight shift towards lower magnetic fields of one of the two distinct absorptions overlapping all over the experimental range.The comparison between these and previous [5.14, 5.15] results gives evidence of these two contributions. The spectra do illustrate the point that, for all the powdered samples, the e.p.r linewidth increases significantly below T_c.

Several other workers have reported spectra similar to those of Bartucci et al. on powdered or sintered polycrystalline solids of $YBa_2Cu_3O_{7-x}$. For example Castillo [5.9] gave the result reproduced in Figure 5.10a, and Durny et al. [5.10] gave a selec-
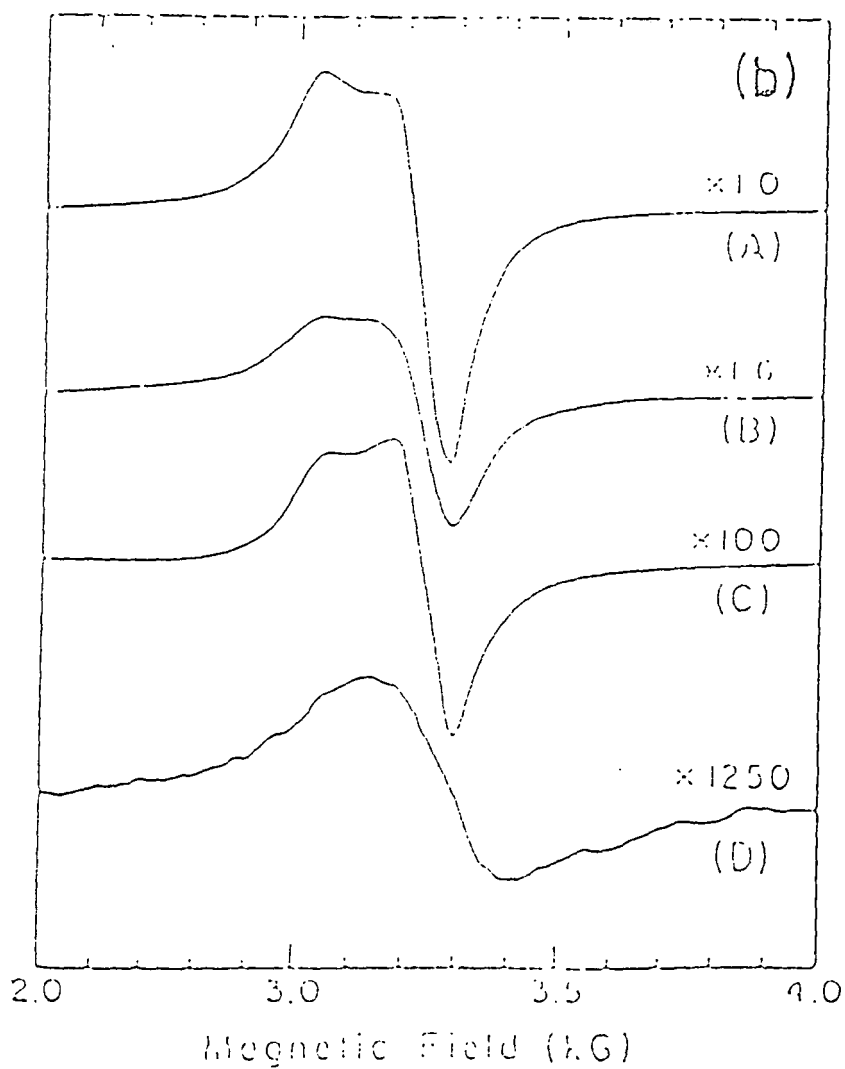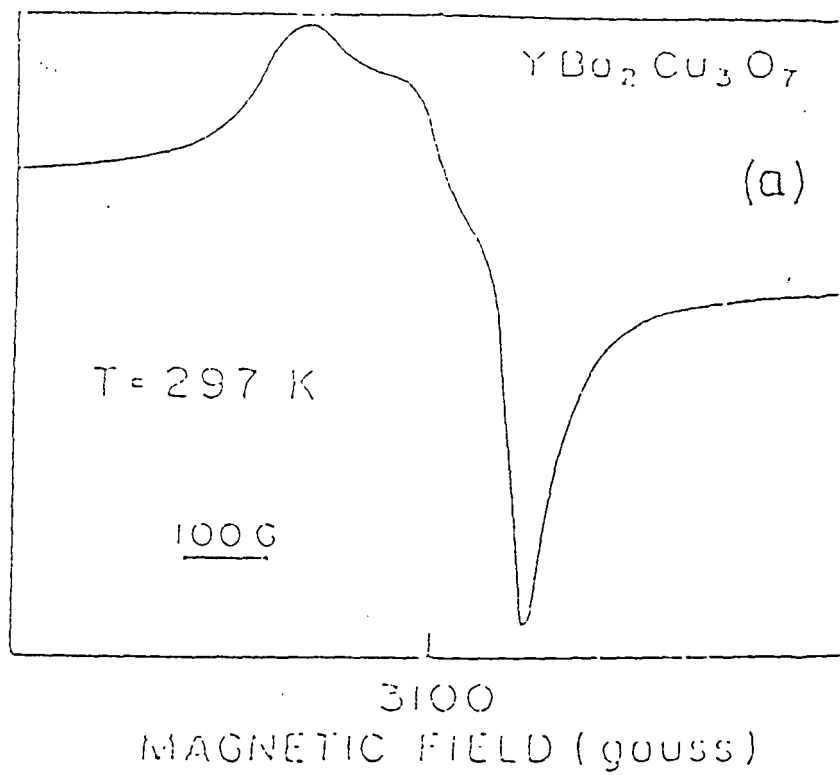
Figure 5.10. EPR Spectra of polycrystalline YBCO;

(a) after Castello et al. (b) after Durny et al.

tion of spectra shown in Figure 5.10(b). In Figure 5.10(b) (B) was a superconducting multiphase system prepared according to Chu et al. [5.16], and (C) was prepared according to Cava [5.17] and Hinks [5.18]; for both of these samples the measurements were made at room temperature. A further examination of the g- 2 E.P.R resonance in $YBa_2Cu_3O_{7-x}$ was made by Amoretti et al. [5.8] who also made the measurement at X-band. Their room temperature spectra are shown in Figure 5.11. These refer to both sintered and powdered samples prepared from fine pure Y_2O_3, $BaCO_3$ and CuO (99.99 % purity) powders which were first mixed and heated for 16h at 950°C and subsequently pressed into pellets and heat-treated for 12h in flowing oxygen at 950°C. These authors also selected small single crystals of about 0.15mm size and observed the E.P.R spectrum of the powder obtained by grinding up these single crystals. The temperature variation of the spectrum has been studied by Stanskowski et al.[5.11] using standard ceramic polycrystalline $YBa_2Cu_3O_{7-x}$ is shown in Figure 5.12. Single crystals of the high T_c superconductor $YBa_2Cu_3O_{7-x}$ have also been examined by e.p.r by Mehran et al. [5.12]. Figure 5.13 shows the single crystal e.p.r spectra observed by Mehran with the magnetic field applied either parallel or perpendicular to the plane of the crystal.

It can be seen that the features revealed in the experimental spectra observed here, Figures 5.6, 5.7 and 5.8, show many similarities with those reported by the authors referred to above for samples of similar composition and form. In summary two distinctive types of spectrum are observed. The first of these e.g. Figures 5.6,5.8,5.9,5.10,5.11(a),5.11(b) and 5.12 shows four features and the overall linewidth

Magnetic Field (G)
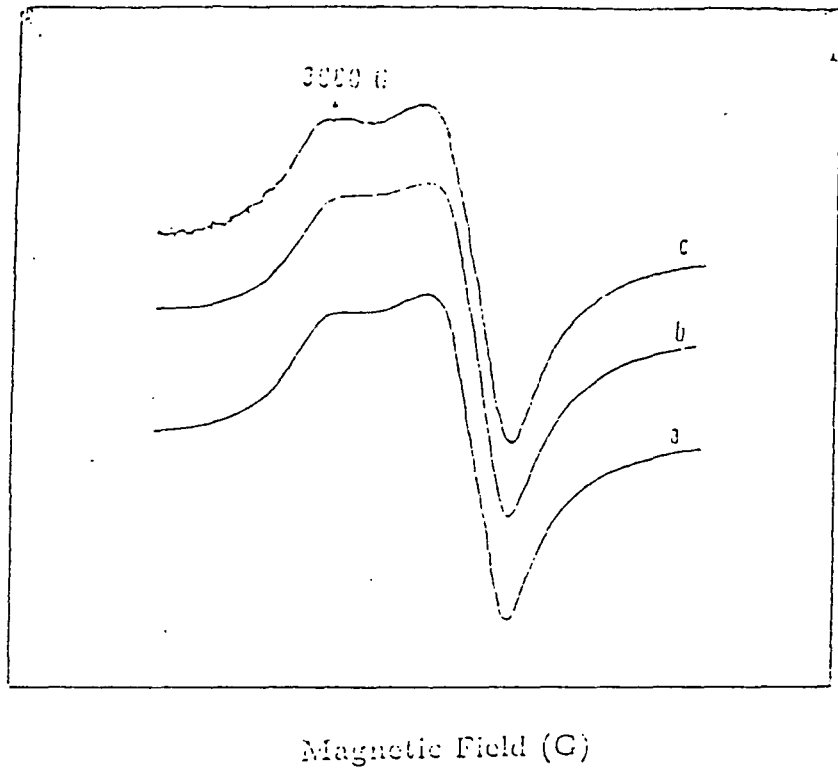
Figure 5.12. EPR Spectra of YBCO powder

(Stankowski et al); (a) 100K, (b) 87K, (c) 80K.

MAGNETIC FIELD (G)

MAGNETIC FIELD (G)
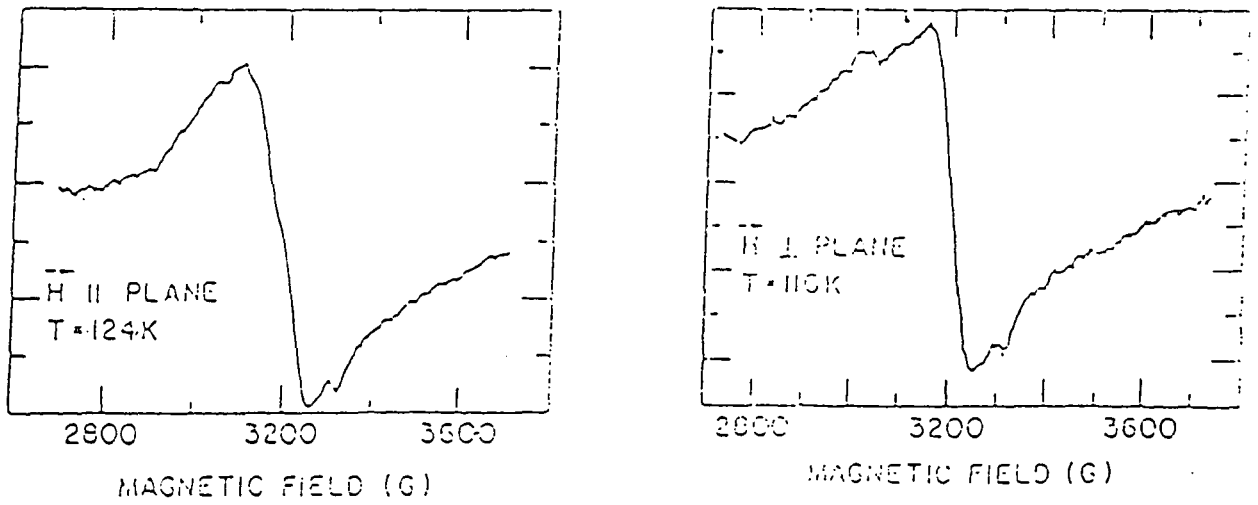
Figure 5.13. EPR Spectra of YBCO single crystal

(Mehran et al):

is large; by contrast the second type of spectrum consistes essentially of a single, nearly symmetrical line, Figure 5.7 and 5.11(b). The single crystal data, Figure 5.13 gives some evidence for fine structure but is dominated by a nearly symmetrical high intensity feature centered near a g-value of 2.086. In general it is found that materials which give the broad asymmetrical spectrum do not exhibit superconductivity (at least above 77K) whereas the materials which gave the narrower symmetrical spectrum are superconducting with T_c of the order of 90K. It is evident from the work undertaken here that e.p.r. will form a very useful technique by which to relate detailed structural information to the occurrence of superconductivity. This however would require careful and systematic study of several samples and much more detailed analyses of the e.p.r. spectra.

REFERENCES

5.1. N.M.R and E.S.R Spectroscopy, (Varian Associates) Pergamon, London,(1964).

5.2. A.Abraham and B.Bleaney. Electron Paramagnetic Resonance of Transition Ions. Clarendon Press, Oxford, (1970).

5.3. W.Low. Paramagnetic Resonance in Solids, Solid State Physics, Supplement 2; Academic Press, N.Y. (1960).

5.4. H.M.Assenheim "Introduction to Electron Spin Resonance" Hilger and Watts, (1966).

5.5. C.P.Poole "Electron Spin Resonance", Wiley-interscience, N.Y. (1967).

5.6. A.R.Skinner, Ph. D. Thesis, Durham University (1986).

5.7. R.Bartucci, E.Colavita, and L.Sportelli, G.Balestrino and S.Barbanera. Phys. Rev. B 37, 2313, (1988).

5.8. G.Amoretti, E.Bluluggiu, A.Vera, G.Calestani and F.C.Matacotta. Z.Phys. B-Cond. Matt. 72, 17 (1988).

5.9. J.H.Castilho, P.A.Venegas, G.E.Bareris, C.Rettori, R.F.Jardim and S.Gama. Solid Stat Commu. 64, 1043 (1987).

5.10. R.Durny, J.Hautala, S.Ducharme, B.Lee, O.G.Symko, P.C.Taylor, D.J.Zheng and J.A.Xu. Phys. Rev. B 36, 2361 (1987).

5.11. J.Stankowski, P.K.Kahol, N.S.Dalal and J.S.Moodera. Phys. Rev. B 36, 7126 (1987).

5.12. F.Mehran, S.E.Barnes, T.R.McGuire, T.R.Dinger, D.L.Kaiser and F.Holtzberg. Solid State Commu. 66, 299 (1988).

5.13. D.H.A.Blank, J.Flokstra, G.J.Gerritsma, L.J.M.VAN DE Klundert and G.J.M.Velders. Physica 145B, 222, (1987).

5.14. D.Shaltiel, J.Genossar, A.Grayevsky, Z.H.Kolman, B.Fisher and N.Kaplan, Solid State Commu. 63, 987, (1987).

5.15. F.Mehran, S.E.Barnes, T.R.McGuire and W.J.Gallagher, Phys. Rev. 36B, 740, (1987).

5.16. C.W.Chu, P.H.Hor, R.L.Meng, L.Gao, Z.I.Huang and Y.Q.Wang, Phys. Rev. Lett. 58, 405, (1987).

5.17. R.J.Cava, B.Batlogg, R.B.van Dover, D.W.Murphy, S.Sunshine, T.Siegrist, J.P.Remeika E.A.Rietman, S.Zahurak, and G.P.Espinosa, Phys. Rev. Lett. 58, 1676, (1987).

5.18. D.G.Hinks, L.Soderholm, D.W.Capone II, J.D.Jorgensen, I.K.Schuller, C.U.Segre, K.Zhang and J.D.Grace, Appl. Phys. Lett. 50, 1688, (1987).

CHAPTER SIX

CONCLUSIONS (Part I)

As regards the structural characterization of the materials it has been shown that relatively simple XRD methods are sufficient to distinguish between the wide variations which occur between batches of the same nominal composition. The 11.50 cm diameter Phillips powder camera used gave an accuracy in lattice parameter determination of $\pm 0.008\overset{\circ}{A}$. One of the difficulties is that small changes in the lattice parameters correspond to variations in oxygen content which, although quite small, determine the crucial difference between superconducting and non-superconducting behaviour. West's paper suggests that departures from x=7.0 to x=6.5 are enough to cause this and this range of x values corresponds to change in c value of only from 11.715 to 11.755$\overset{\circ}{A}$. To follow these changes with precision required more precise techniques. However the present work shows quite definitely that the specimens which showed superconductivity were those with x values nearest to x=7.0. As regards EDAX and SEM the EDAX results do suggest that there may be considerable changes in Y:Ba:Cu ratios between individual grains and although these results may require some correction for self absorption etc. they are larger than would have been expected. The direct SEM micrographs on the other hand do provide useful and reliable information on the microstucture of the ceramic. Any effects due to sample charging can easily be overcome by evaporating a thin layer of gold on the sample. With conventional SEM equipment good contrast can be achieved and detailed in-

formation on the grain sizes and shapes obtained. For the samples examined here significant changes in both particle shape and size were found for the different samples and in particular it was verified that a sintered pellet made from a given powder had a microstucture very different from that of the powder. The pellets which showed most superconductivity were those which had large (order of 10μm), square or rectangular grains closely packed together. The SEM micrographs also showed the presence of smaller grains, which may a second phase, interspersed between the large grains. It would advantageous to be able to obtain diffraction patterns from each grain, a problem which could probably be solved by electron diffraction. EPR has also been shown to be a useful technique for the initial selection of samples. Most of those which showed superconducting behaviour have an epr spectrum which shows two unresolved peaks on the low field side of a symmetric, more intense feature centered near g=2. Some of those which do not show any superconductivity gave a single symmetrical line of high intensity at room temperature which may have been due to the ferromagnetic impurity known to have been present.

The main work has been concerned with the development of the inductance probe technique and its use in establishing important parameters of superconducting material. It is convenient to consider first the use of the probe in the absence of an external applied magnetic field. Under these conditions it has been shown that it gaves a very reliable means of finding T_c and observing the shape of the superconducting transition. One major advantage of the technique in this respect is that no electrical contacts are required (the provision of electrical contacts often causes dificulty in

the alternative resistance versus temperature method of finding T_c). For the various YBCO samples examined the T_c values were mostly near 86K with one exception at 124K. The determination of T_c does not require absolute values of inductance to be known since the position of the superconducting transition is located purely on the temperature axis. The absolute changes in inductance between temperatures above and below T_c can however be used to estimate the percentage of superconducting material in the sample. The relation derived is

$$S = \frac{L_{RT} - L_{77}}{P L_{RT}} \times 100 \qquad (6.1)$$

where P is the packing fraction and this is based on the exclusion of flux by a superconductor below T_c. It should be noted that the technique and the formula 6.1 are applicable to any sample and to any form of sample i.e to powders or to solid sintered pellets. This method for determining the percentage of superconductor is of general application and is not restricted to YBCO material only; thus it could be used as here with conventional superconductors or with other high T_c superconductors of completely different composition such as the Tellurium, Lanthanum or Gadolinium componds. For the range of superconducting powders examined S was generally only a few percent while for sintered pellets it rose to as much as 25% in some cases.

As regards relating the microstucture of a sample to its superconducting behaviour there is some evidence that grain size is an important factor. The larger values of S were obtained with samples in which the grain size was about 10μm and in which the grains were well packed together. There are also noticable differences

in the width of superconducting transition between different specimens but there is insufficient detailed structural information to enable precise correlation to be made. The reasons for the relativly low values of S even in the sintered pellet remain unclear. Most of the structural information, supported by results from other laboratories, suggests that most of the materials examined were mainly single phase. On this basis the low value of S could be attributed to small changes in oxygen content which would not have given sufficiently large changes in lattice parameters or Y:Ba:Cu ratios to be detected. An alternative explanation might be that the magnetic field generated by the current in the probe coil during measurement exceeded H_{c_1}. In the present experiment this was unlikely as care was taken to reduce this field to about 1 gauss which is less than a tenth of the reported literature values of H_{c_1}.

A complete series of measurements were also made with the inductance probe operating in the presence of an external magnetic field. This mode of operation enabled inductance versus magnetic field plots to be obtained. Most of these were taken at 77K and permitted evaluation of the lower critical field H_{c_1} and also approximate estimation of upper critical field H_{c_2}. In contrast with most of the previously reported data (which gave H_{c_1} values ranging from 70 gauss to 750 gauss) all the superconducting YBCO samples examined here had H_{c_1} values near 15 gauss. The L-H plots also demonstrated the occurence of hysteresis.

The inductance probe method has also been used to make a preliminary examination of penetration depth. It was possible with one sample which had an exceptionally

high T_c (124K) to make measurements at several temperatures below T_c. It was observed that the inductance at zero magnetic field varied with temperature in exactly the manner predicted by the known variation of penetration depth with temperature for Type II superconductors.

Part II
Studies on Cr/MgO
single crystals and
powders

CHAPTER SEVEN

STRAIN BROADENING OF EPR LINEWIDTHS
IN Cr/MgO SINGLE CRYSTALS AND POWDERS

7.1 Introduction

In a resent publication Thorp and Skinner discussed the dependence of EPR linewidth on concentration in Mn/MgO single crystals [7.1] and found that the peak-to-peak linewidth was concentration dependent and of the right order of magnitude to be explain adequately in terms of the de Biasi and Fernandes theory of dipolar broadening [7.2]. During the course of that work it was realised that strain, if present in the materials examined, could have caused some line broadening which would have effected the degree of correspondence between the experimental and theoretical results. Consequently, before attempting to make a corresponding study of the EPR linewidth dependence on concentration in Cr/MgO, it was decided to investigate strain effects, so that more reliable data could eventually be used for the linewidth versus concentration examination. Thus in this Chapter we discuss the reduction in linewidth observed in both single crystals and powdered single crystal Cr/MgO specimens which had been subjected to annealing heat treatments in order to remove residual strain arising during the growth by electrofusion [7.3] of the doped crystals.

In real crystals lattice distortions are always present. They may arise from a

variety of causes including strain, such as that created when the dopant ion and the cation of the host lattice differ in size, point defects, such as vacancies and interstitial ions, planar defects such as stacking faults and dislocations. The combined effect of all types of crystal imperfection is to create a strain field, the magnitude of which at a particular point in the crystal is determined by the distribution of defects throughout the crystal. The strain field may either change the point symmetry at the paramagnetic ion or preserve the point symmetry but change the crystal field parameters slightly. In the former situation any change in the symmetry of the site occupied by a paramagnetic ion will dramatically alter its EPR spectrum. In the latter, the strain field changes the values of the crystal field parameters for an individual paramagnetic ion and so the resonant field of that ion will be altered. As the amount of strain to which individual paramagnetic ions are subjected is variable, the resonant fields of the assembly of ions will be distributed over a range of values and hence the absorption lines will be broadened, although the overall form of the spectrum will remain unaltered. The effect of uniaxial stresses on the paramagnetic spectra of doped MgO has been discussed by Feher [7.4]. The most important prediction of this theory is that the strain broadening for a given transition is proportional to $(2M - 1)^2$ where M is the quantum number of the transition. Hence, for any given impurity ion, to first order the $M = 1/2 \leftrightarrow -1/2$ transition is not broadened by strain whereas the broadening observed for the $M = \pm 3/2 \leftrightarrow \pm 1/2$ transition is one quarter of that observed for the $M = \pm 5/2 \leftrightarrow \pm 3/2$ transition.

7.2 Characterization of Cr^{3+} in MgO

For Cr^{3+} in the octahedral crystal field of MgO the $^4A_2$ orbital singlet is responsible for the paramagnetic resonance absorption and for EPR spectroscopy this level may be regarded in isolation, as the next highest triplet (T_2) is separated by about $10^4 cm^{-1}$. Since the $^4A_2$ state acts like a ^4S state it might be expected that the spin Hamiltonian would simply be

$$H_s = g\beta H.S \qquad (7.1)$$

and thus that in the cubic field the three predicted transitions would coincide to give one line with a g-factor corresponding to an orbital singlet, i.e. g=2. However the Cr^{3+} spectrum is complicated since there is a stable isotope $(Cr^{53}$ of about 9.55% abundance with a nuclear spin of 3/2 [7.5,7.6]. This results in a small but detectable hyperfine structure and the complete spin Hamiltonian becomes [7.7]

$$H_s = g\beta H.S + AI.S \qquad (7.2)$$

Including second order effects, the transitions occur at

$$H = H_0 - Am - (A^2/2H_0)[I(I+1) - m^2 + m(2M+1)] \qquad (7.3)$$

where $H_0 = h\upsilon/g\beta$ (υ is the applied field frequence).

Experimentally, the terms in (A^2/H_0) are found to be very small $(A = 1.8mT$, $H_0 = 340mT$ at 9GHz) and the three transitions for each value of m are unresolved to give four hyperfine lines at magnetic field values of:

$$(a)\, m = +3/2, H = H_0 - 3/2A;$$

$$(b)\, m = +1/2,\, H = H_0 - 1/2A;$$

$$(c)\, m = -1/2,\, H = H_0 + 1/2A;$$

$$(d)\, m = -3/2,\, H = H_0 + 3/2A. \tag{7.4}$$

The EPR spectrum of the isotopes of chromium without nuclear spin can be described by the Hamiltonian of equation (7.1) and the spectrum consists of a single line with a g-value of 1.9800 [7.7]. The deviation of the g-value from the spin only value of 2.0023 is caused by a contribution [7.8,7.9] from the triplet T_2 to the orbital moment of the ground state. Since the Cr^{53} isotope is only 9.55% abundant each hyperfine structure line has an intensity of approximately 1/42 [7.6] of that of the main line at g=1.9800. All seven lines of the spectrum are isotropic.

7.3 Experimental Results for Cr/MgO Single Crystals.

7.3.1 As-grown Specimen, spectra parallel to $< 100 >$.

The EPR spectra of the Cr/MgO single crystals were first recorded on a Varian V4205-15 spectrometer at room temperature with the magnetic field parallel to one of the cubic axes. Seven different samples were examined, in which the nominal Cr concentration ranged from 800 ppm to 15100 ppm by weight. Some typical single crystal spectra are given in Figure 7.1 and Figure 7.2. The spectrum shown in Figure 7.1, which refers to a crystal containing 800 ppm Cr, consists of a single, intense line
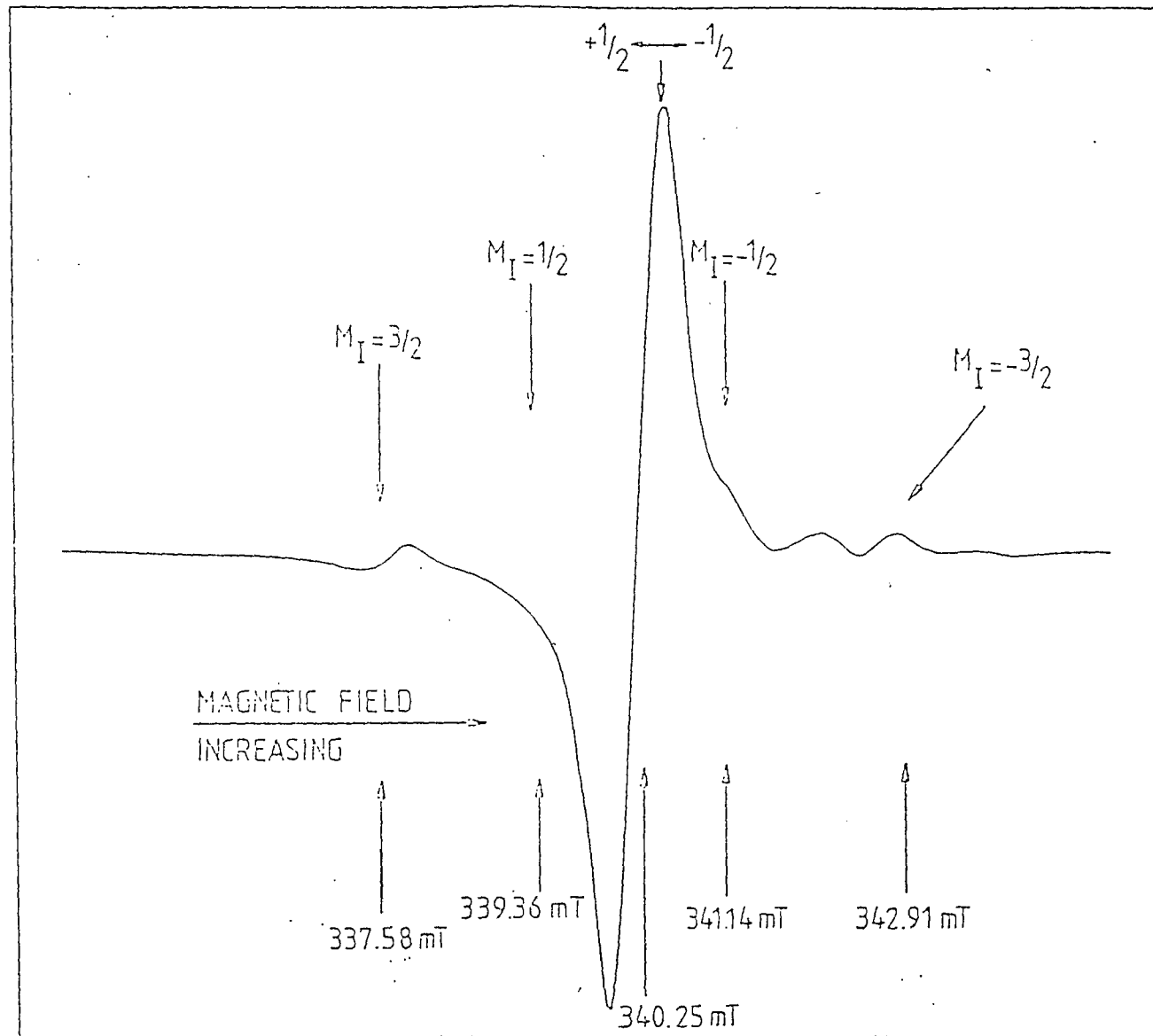
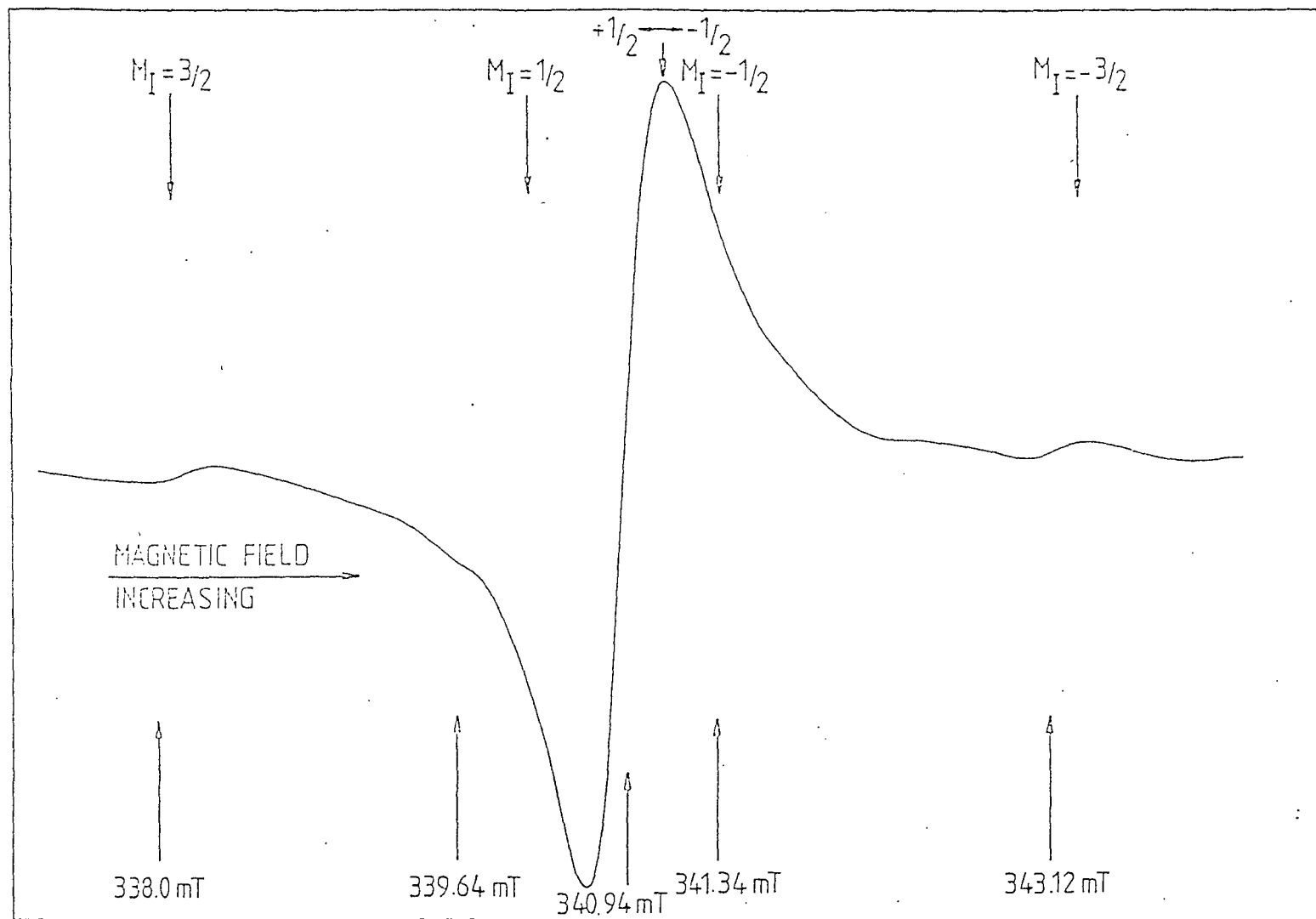Figure 7.1: DETAIL OF E.P.R SPECTRUM OF SINGLE CRYSTAL Cr/MgO; 800 p.p.m Cr, 293K, H//<100>, 9.4273 GHz.

Figure 7.2: DETAIL OF E.P.R SPECTRUM OF SINGLE CRYSTAL Cr/MgO; 5,000 p.p.m Cr, 293 K, H//<100>, 9.4410 GHz.

with a g-factor of approximately 1.9800 and four less intense lines which are centred on the main line and are equally spaced, successive components being separated by approximatelly 1.8 mT. The intensity of each line of the quartet is about one fortieth of that of the main line. Figure 7.2 shows the corresponding spectrum for a crystal containing a much larger chromium concentration of 5000 ppm Cr; this reveals the same general features, except that the linewidths are increased.

This spectrum is well known. It was first reported by Low [7.7] and is due to Cr^{3+}ions occupying sites of octahedral symmetry. The central line arises from the $M = +3/2 \leftrightarrow +1/2, M = +1/2 \leftrightarrow -1/2$ and $M = -1/2 \leftrightarrow -3/2$ transitions of the isotopes of chromium with no nuclear spin $(Cr^{50}, Cr^{52}$ and $Cr^{54})$ which are coincident because the four electronic energy levels of these isotopes are equally spaced and, in strong magnetic fields, diverge linearly as the applied magnetic field increases. The four less intense lines are hyperfine transitions due to chromium, Cr^{53}, which has a nuclear spin, I, of 3/2. The equally spaced hyperfine lines are accurately predicted by equation (7.4) and the separation between successive hyperfine lines is equal to A, the hyperfine structure constant. The natural abundance of the Cr^{53} isotope is 9.55% and since all four hyperfine lines are equally intense, each hyperfine line is expected to have an intensity of about 1/42 of that of the main line. The observed intensity ratio of 1/40 is in close agreement with this prediction.

The parameters characterizing the EPR spectrum of the Cr^{3+}ions in sites of octahedral symmetry (the g-factor, the peak-to-peak linewidth of the central line

and A, the hyperfine structure constant identified with the hyperfine transitions of the Cr^{53} isotope) were measured for each of the chromium doped magnesium oxide single crystals and the values obtained are given in Table 7.1. The g-factors and hyperfine structure constant are in close agreement with each other and also with previously published data [7.7,7.10,7.11].

The Cr^{3+}ions giving rise to the EPR spectrum described occupy sites of octahedral symmetry and it is likely that they substitute for Mg^{2+} ions in the magnesium oxide host lattice. In addition, the spectrum described is characteristic of Cr^{3+}ions that are isolated from each other which implies that the Cr^{3+}ions are not clustered together and do not co-operate magnetically (in contrast, for example, to ions that are exchange coupled which do co-operate in such a way that their spins become partially or fully aligned and the ions so coupled together act as a single unit). The only interactions taking place between the isolated Cr^{3+}ions are dipolar in nature.

7.3.2 As-grown specimens; polar plots.

EPR spectra were recorded at 10° intervals as the crystal doped with 800 ppm of chromium was rotated in a [100] plane. An additional spectrum was recorded when the crystal had been rotated through 45° as at this point the magnetic field was parallel to a < 100 > type direction in the crystal. Figure 7.3 shows the variation of the resonant magnetic fields of three transitions of the cubic Cr^{3+}spectrum with

Chromium concentration (ppm)	Linewidth $\triangle H_{pp}$ (mT)	g-Factor	Hyperfine structure constante A($\times 10^4 cm^{-1}$)	Frequence (GHz)
800	0.506	1.9797	16.44	9.4275
2500	0.547	1.9806	-	9.4200
3600	0.921	1.9799	16.61	9.4295
5000	1.09	1.9797	-	9.4420
7400	0.645	1.9794	16.68	9.4290
9500	0.493	1.9764	-	9.4285
15100	0.564	1.9806	16.48	9.4280

Table 7.1: EPR Parameters for single crystal Cr/MgO samples H// $< 100 >$, 293K.

Concentration (ppm)	α_1 (HRS^{-1})	α_2 (HRS^{-1})
2500 Single crystal	0.038	0.909×10^{-3}
3600 Single crystal	0.038	1.141×10^{-3}
5000 Single crystal	0.040	1.250×10^{-3}
3600 Powder	0.016	1.000×10^{-3}

Table 7.2: Values of first and second decay rates for single crystal and powdered Cr/MgO.
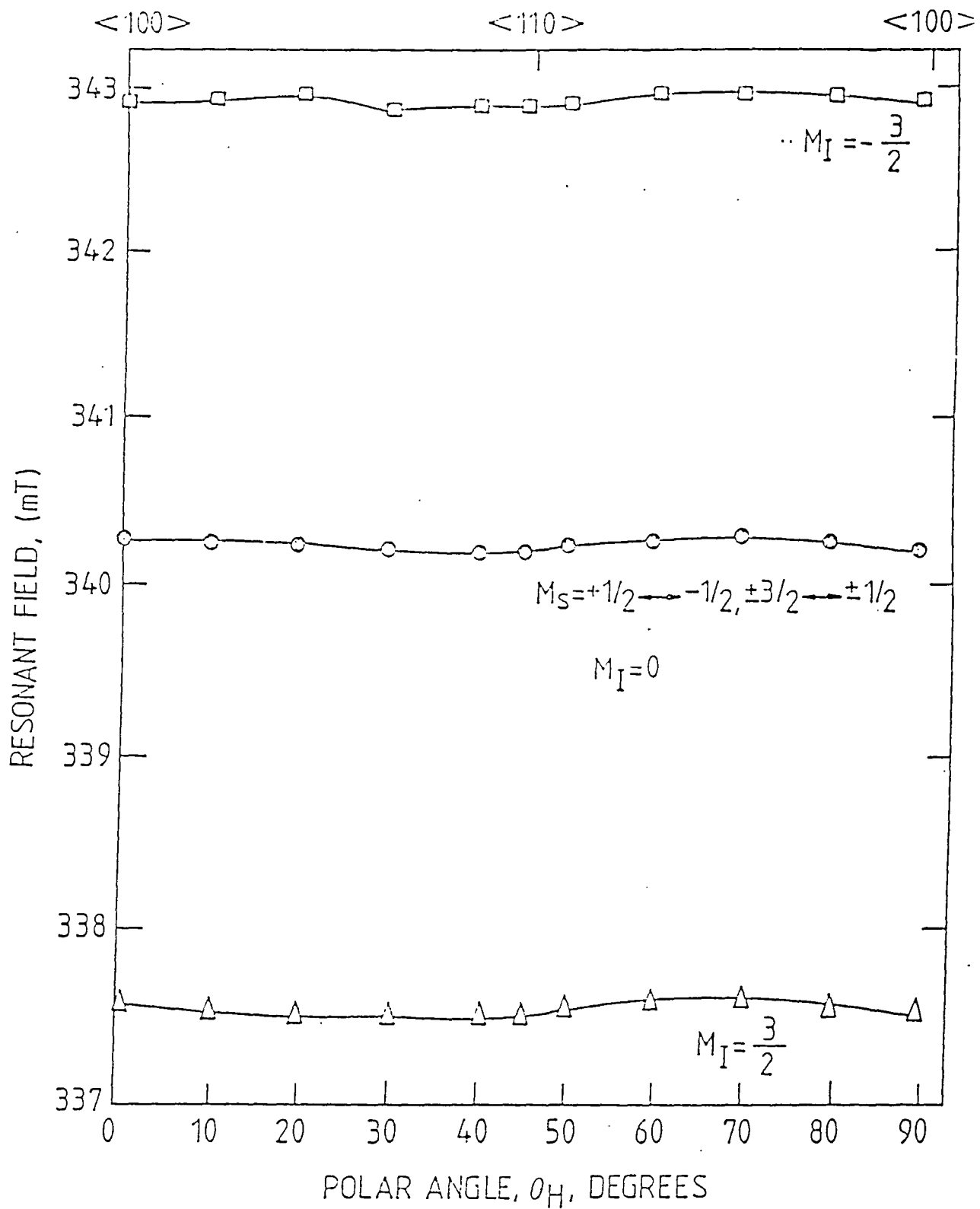
Figure 7.3: VARIATION OF RESONANT FIELD WITH POLAR ANGLE. SINGLE CRYSTAL Cr/MgO, 800p.p.m. Cr, [100] PLANE, 293 K, 9.4275 GHz.

polar angle θ_H (the angle between the $< 100 >$ type direction and the magnetic field). The three transitions are the central one (which arises from superimposed $M = +1/2 \leftrightarrow -1/2$ and $M = \pm 3/2 \leftrightarrow \pm 1/2$ transitions of the isotopes of chromium with no nuclear spin) and the two outermost hyperfine transitions ($M_I = +3/2$ and $M_I = -3/2$ of the Cr^{53} isotope. The resonant magnetic fields of the inner hyperfine transitions ($M_I = +1/2 and M_I = -1/2$) of the Cr^{53} isotope could not be determined because these transitions were not fully resolved from the outer wings of the main line in the spectrum.

Figure 7.3 shows that, in agreement with previously published data, [7.7,7.10,7.11] the cubic Cr^{3+} spectrum is largely isotropic, although the small fluctuations in the resonant magnetic fields of all three transitions follow a similar pattern. It may be deduced that, due to its isotropic nature, the Cr^{3+} spectrum has the same form in both single crystal and powdered magnesium oxide, a feature which will be discussed later.

There was no evidence from the full EPR spectra of any of the chromium doped samples that any fraction of the chromium existed in any valency state other than the trivalent (Cr^{3+}) state. The Cr^{+} ion has a $3d^5$ electronic configuration, but it is not surprising that it is not present in our samples, since it has only been observed (using EPR techniques) in magnesium oxide single crystals which have been subjected to γ-ray irradiation [7.12]. The Cr^{2+} ion presents a more difficult problem. In magnesium oxide, it has not been observed using normal EPR methods, although it has been

detected using acoustic paramagnetic resonance [7.13,7.14,7.15]. It is generally agreed that the Cr^{3+}ion is far more stable than the Cr^{2+} ion at room temperature. The conclusion reached from the characterisation was that all the chromium dopant in the samples existed in the trivalent Cr^{3+}state.

7.3.3 Annealing of Single Crystal Cr/MgO.

For heat treatment, each sample was loaded in a boat and placed in the center of a furnace. A thermocouple was located as close as possible to the sample boat and a temperature controller connected to monitor the required temperature. A steady flow of oxygen gas was passed through the furnace to maintain oxidising conditions.

The heat treatments were completed at 500° C for different lengths of time for samples containing several different levels of chromium, i.e. 5000 ppm, 3600 ppm and 2500 ppm. After each annealing period the samples were allowed to cool down gradually (from 500° C to room temperature through five hours). The g-factor and peak-to-peak linewidth of the central transition, $\triangle H_{pp}$, were measured for each spectrum after each annealing time. There was no change in the g-factor but it was found that there was a decrease in the peak-to-peak linewidth, $\triangle H_{pp}$, with annealing time increasing until a constant value was eventually reached. This is shown graphically in Figure 7.4 which refers to the 3600 ppm Cr crystal. It appears from Figure 7.4a
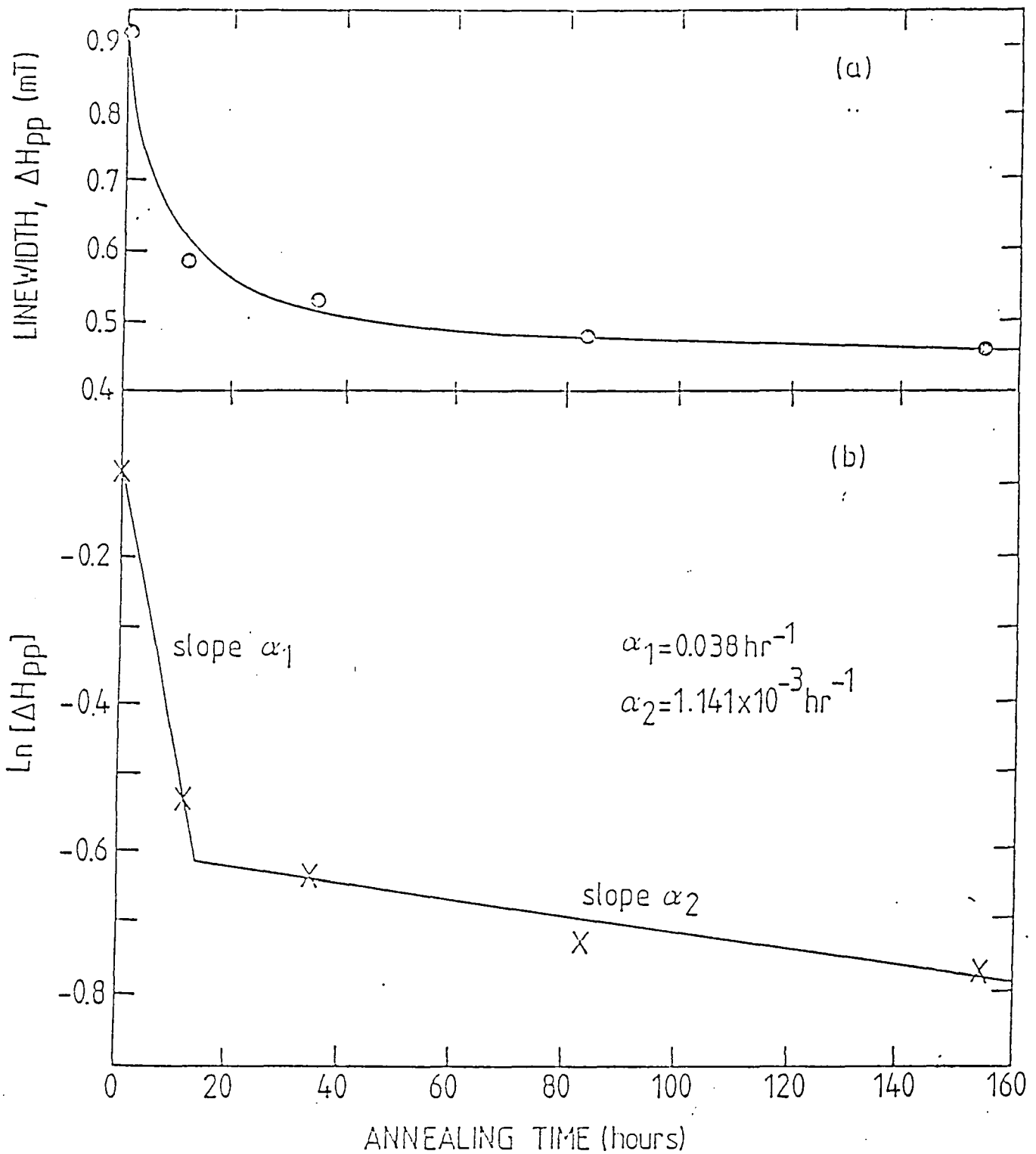
Figure 7.4: VARIATIONS OF (a) LINEWIDTH ΔH_{pp} AND (b) Ln [ΔH_{pp}] WITH ANNEALING TIME; SINGLE CRYSTAL Cr/MgO, 3,600 p.p.m. Cr, H//<100>, 293K.

that there was an exponential decay of the form:

$$[\triangle H_{pp}]_t = [\triangle H_{pp}]_0 exp^{-\alpha t} \tag{7.5}$$

where:$[\triangle H_{pp}]_t$ is the peak-to-peak linewidth after heat treatment of t hours, $[\triangle H_{pp}]_0$ is the peak-to-peak linewidth before heat treatment, and α is a constant and may be determined from the slope of the plot of $ln[\triangle H_{pp}]$ against annealing time, t.

This was confirmed by the semi-log plot shown in Figure 7.4b which however reveals two linear regions of different slope representing two separate decay times. Similar annealing experiments were made with two other single crystals, containing 2500 ppm Cr and 5000 ppm Cr respectively and the data is shown in Figure 7.5. Each of these crystals also exhibited a two stage reduction in linewidth resulting from annealing and the collected decay rate data is given in Table 7.2, which also includes a result obtained from a sample of powdered single crystal.

7.4 Experimental Results for Cr/MgO Powders

7.4.1 Characterization of the EPR Spectra

Powders were prepared from single crystal chippings of five chromium doped MgO samples. The chippings were crushed and the powders were sieved through a $185\mu m$ mesh. Spectra were recorded from all five powders and comparison with the single crystal spectra shows that the two are almost identical and confirms that
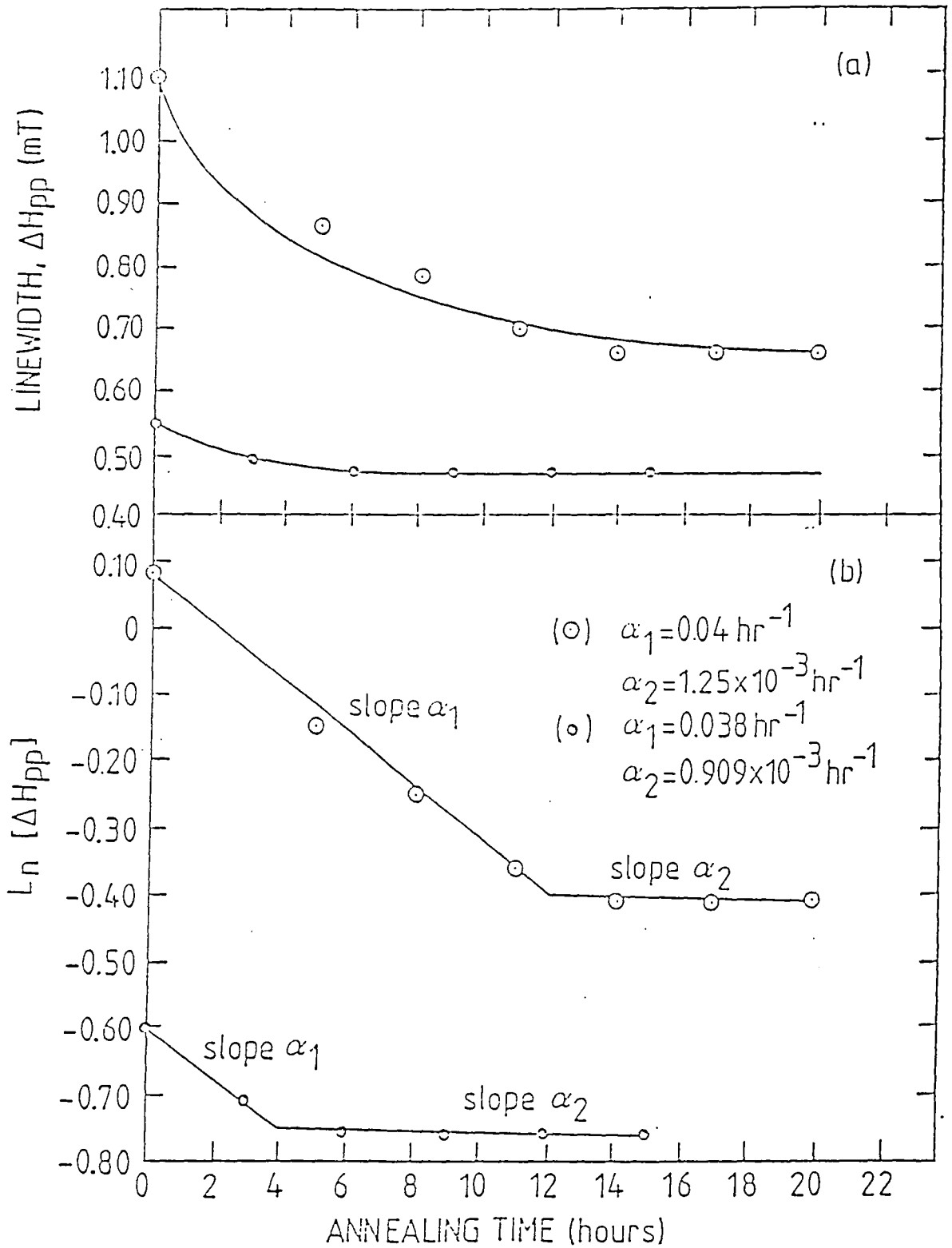
Figure 7.5: VARIATIONS OF (a) LINEWIDTH ΔHpp AND (b) Ln [ΔHpp] WITH ANNEALING TIME; SINGLE Crystal Cr/MgO, 5,000 p.p.m. Cr (⊙), 2,500 p.p.m. Cr (○), H//<100>, 293 K.

the powder spectrum can be identified with isolated Cr^{3+} ions in sites of octahedral symmetry. The powder is a collection of randomly oriented crystallites but the resonant magnetic fields of the various transitions are independent of polar angle. The cubic Cr^{3+} spectra obtained from the powder samples were analysed to give the g, A and $\triangle H_{pp}$ values listed in Table 7.3; these agree to within experimental error with those obtained from the single crystal samples (Table 7.1) and also with those published in the literature [7.7,7.11]. It is noticeable that, for each doped sample, the linewidth is greater than in the corresponding single crystal from which the powder was made. Only the cubic Cr^{3+} spectrum is observed for the powder samples. The axial Cr^{3+} spectrum and the Cr^{3+} pair spectrum, both of which were observed for the single crystal samples, are not seen. This is because these spectra are highly anisotropic and the associated transitions are spread over a wide range of magnetic fields. Thus the powder spectra are much cleaner than the single crystal spectra in that the number of lines observed is greatly reduced.

Computer simulation of the powder spectrum of Cr^{3+} in octahedral sites in MgO were also undertaken [7.16]. The values of A and g determined experimentally from the single crystal spectrum at a particular dopant concentration were used to simulate the powder spectrum at the same dopant concentration. Because of this the computed powder spectrum at any given dopant concentration should, if the simulation procedure is valid, be identical to the experimental single crystal spectrum at the same dopant concentration. This was found to be the case.

Chromium concentration (ppm)	Linewidth $\triangle H_{pp}$ (mT)	g-Factor	Hyperfine structure constante A($\times 10^4 cm^{-1}$)	Frequence (GHz)
800	0.568	1.9793	16.43	9.4290
3600	0.929	1.9804	16.41	9.4275
7400	0.721	1.9797	16.31	9.4280
9500	0.587	1.9793	16.42	9.4270
15100	0.674	1.9791	16.59	9.4275

Table 7.3: EPR Parameters for powdered Cr/MgO samples; 293K.

Annealing time (HRS)	Linewidth $\triangle H_{pp}$ (mT)	g-Factor	Hyperfine structure constante A($\times 10^4 cm^{-1}$)	Frequence (GHz)
0	0.929	1.9804	16.41	9.4275
12	0.772	1.9791	16.60	9.3800
24	0.690	1.9796	16.42	9.3790
35	0.699	1.9792	16.56	9.3800
83	0.646	1.9791	16.58	9.3805
155	0.617	1.9790	16.50	9.3800

Table 7.4: EPR Parameters at 293K for 3600 ppm Cr/MgO powdered samples annealed for various times.

7.4.2 Annealing of Powder Specimens

At any given dopant concentration, the linewidth of the central transition of the cubic Cr^{3+} spectrum measured for the single crystal is the same as its width in the computer simulated powder spectrum, although it is considerably broader in the experimental powder spectrum. It might be thought that the discrepancy is due to the variation of dipolar linewidth with polar angle. However, it has been reported in the literature [7.10] that, at all the dopant concentrations examined here, the width of the central transition in the cubic Cr^{3+} spectrum is independent of the polar angle θ. Thus it appears that dipolar effects cannot explain the increase in the width of the central line in the cubic Cr^{3+} spectrum when a single crystal is powdered.

We propose that the linewidth of the $M = +1/2 \leftrightarrow -1/2, \pm3/2 \leftrightarrow \pm1/2$ transition is greater in the powder than in the single crystal due to the effects of lattice strain. An experiment was undertaken which provided evidence supporting this suggestion. A similar annealing experiment to that conducted for the single crystal doped with 3600 ppm Cr was undertaken for the corresponding powder. Table 7.4 shows the values of g, A and $\triangle H_{pp}$ measured from the cubic Cr^{3+} spectra which were recorded after the powder had been subjected for various lengths of time to the "annealing" heat treatment. A plot of the linewidth of the central transition against time is illustrated in Figure 7.6(a) and Figure 7.6(b) shows the relationship between $ln(\triangle H_{pp})$ and annealing time. As in the single crystal case, A and g are unaffected by the annealing process. The decrease of the linewidth and the $ln(\triangle H_{pp})$ with the
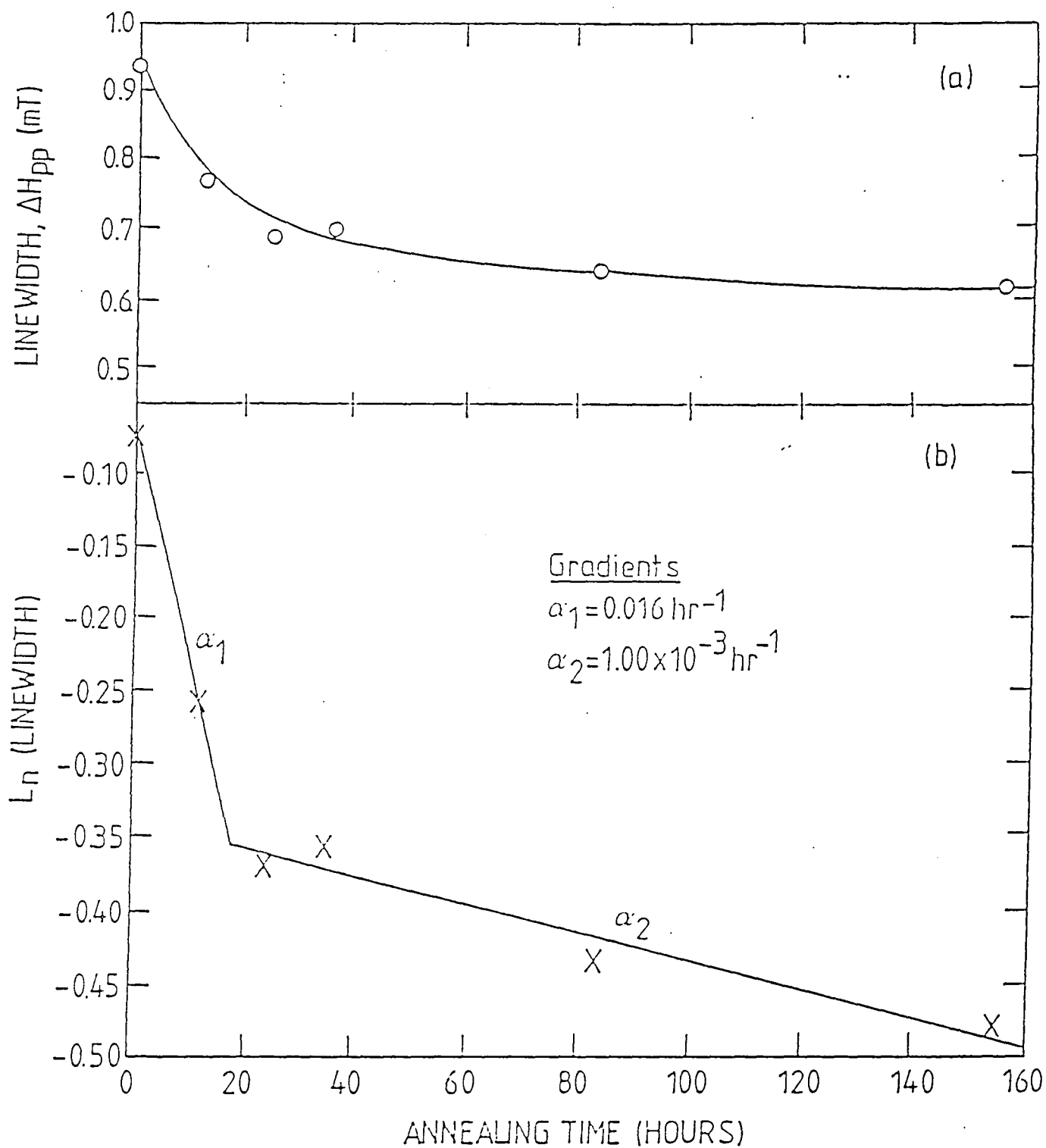
Figure 7.6: VARIATION OF (a) LINEWIDTH ΔHpp AND
(b) ln (ΔHpp) WITH ANNEALING TIME FOR 3,600 p.p.m.
Cr/MgO POWDER; 293 K.

annealing time is also similar in form for the single crystal and powdered samples doped with 3600 ppm of chromium. However, for the powdered sample the decay rates are smaller than for the single crystal.

7.5 Discussion.

In discussing the reasons for the systematic reduction in linewidth as a function of annealing time, one factor may by eliminated at the outset. This is that a decrease in the concentration of isolated Cr^{3+} ions in cubic sites would result in a reduction of $\triangle H_{pp}$, simply because the degree of line broadening arising from dipolar interactions would decrease. However, it has been established, as described in detail by Skinner [7.16], that the annealing process is unlikely to bring about a reduction in the concentration of these ions. Therefore it is proposed that the linewidth decreases after annealing because internal strains in the crystal, which lead to EPR line broadening, are removed as a result of heat treatment. Consideration of the single crystal data indicates that there are two sources of strain in the crystal. One is readily removed by the heat treatment and consequently the initial decrease in linewidth is rapid. The other is not relieved so rapidly by the annealing process and the exponential decay of the linewidth is less rapid. The change in decay rate is not likely to be due to the physical shape of the sample i.e. it is not because the strain in the regions of the lattice surrounding paramagnetic ions near the surface is relieved faster than in the bulk. This may be deduced from comparison of the decay rates for the powdered and

single crystal 3600 ppm Cr/MgO specimens. Although the ratio of surface area to volume is greater for the powder than for the single crystal, in each case there are two distinct decay rates, the annealing times at which the change in rate occurs are similar and the magnitudes of the decrease in the linewudth brought about by the annealing process are also similar.

Each isolated Cr^{3+}ion in octahedral symmetry has a cation vacancy associated with it and although both types of point defect will distort the lattice the strain fields surrounding them will be different. It is proposed that the rapid decay rate is a result of cationic vacancy strain relief and that the slower decay is caused by the removal of lattice distortion originally brought about when Mg^{2+} ions are replaced by Cr^{3+}dopant ions in the host material. With single crystals the changeover point from the rapid to the slower decay occurs at successively longer times as the chromium concentration increase, e.g. from 4 hours with 2500 ppm Cr to 12 hours with 5000 ppm Cr.

Turning to the results obtained from the powdered single crystal material it can be noted first that Figures 7.4a and 7.6a and also Figures 7.4b and 7.6b are virtually identical indicating that the sources of strain in the single crystal and powder samples are the same. Therefore, the sources of strain in the powder are also associated with lattice distortion in both the regions immediately surrounding the cationic vacancies and in those near the isolated Cr^{3+}ions in substitutional sites. The exponential decay of the powder linewidth with increasing annealing time also follows equation

7.5. Examination of the decay rate data given in Table 7.2 shows that both types of lattice strain are relieved by the annealing process at a slower rate in the powder than in the single crystal.

Grinding will increase lattice distortion both in the regions surrounding each cationic vacancy and each isolated Cr^{3+} ion located at a substitutional site. It is noticeable that the annealing time at which the rapid decrease in the linewidth ceases is greater in the case of the powder than in the case of the single crystal. This indicates that there is more strain associated with the rapid decay rate in the powder sample than in the single crystal sample doped at the same level. For confirmation, all five chromium doped MgO powders were annealed for 24 hours using the same heat treatment. Cubic Cr^{3+} spectra were recorded and the values obtained for the crystal field parameters (A and g) and the linewidth $\triangle H_{pp}$ at each dopant concentration are given in Table 7.5. Once again, g and A are unaffected by the annealing process whilst, at each dopant concentration comparison with Table 7.3 shows that the linewudth of the cubic Cr^{3+} central transition is less in the spectrum of the heat treated powder than in the spectrum of the powder before heat treatment. The comparison also shows that, in general, annealing has the greatest effect on the powders which have the largest linewidths before heat treatment. This suggests that the greater the initial amount of strain in powder sample, the greater will be the reduction in lattice distortion for a given period of heat treatment. In addition, the increase in the linewidths of the $M = +1/2 \leftrightarrow -1/2, \pm 3/2 \leftrightarrow \pm 1/2$ transition in the cubic Cr^{3+} spectrum upon

Chromium concentration (ppm)	Linewidth $\triangle H_{pp}$ (mT)	g-Factor	Hyperfine structure constante A($\times 10^4 cm^{-1}$)	Frequence (GHz)
800	0.556	1.9795	16.48	9.3805
3600	0.690	1.9796	16.42	9.3790
7400	0.437	1.9793	16.38	9.3790
9500	0.416	1.9795	16.11	9.3790
15100	0.442	1.9793	16.49	9.3790

Table 7.5: **EPR Parameters at 293K for annealed Cr/MgO powder samples (annealed at** $500°$ **C for 24 HRS and cooled slowly (over 10 HRS)).**

powdering a single crystal sample is, in general, greater the smaller the initial single crystal linewidth. This leads to the conclusion that powdering a single crystal sample introduces lattice distortion more readily if the single crystal is relatively strain free than if the single crystal is highly strained. Thus it appears there is a maximum amount of lattice distortion which the host lattice can support.

REFERENCES

7 .1. J.S.Thorp and A.R.Skinner, J. Magnetism and Magnetic Materials, 69, 34 (1987)

7 .2. R.S.de Biasi and A.A.R.Fernandes, J. Phys. C:Solid state Phys. 16, 5481 (1983).

7 .3. H.E.Buckley, Crystal Growth, John Wiley and Sons, 1951.

7 .4. E.R.Feher, Physical Review, 136, A145, (1964).

7 .5. B.Bleaney and K.D.Daners, Proc. Phys. Soc. (london) A64, 1135, (1951)

7 .6. K.D.Bowers, Proc. Phys. Soc. (london) A65, 860, (1952)

7 .7. W.Low, Phys. Rev. 105, 801,(1957)

7 .8. J.Weber, H.Ennen, U.Kaufmann and J.Schneider, Phys. Rev. B21, 2394, (1980)

7 .9. K.W.H.Stevens and C.A.Bates "Crystal Field Theory in Magnetic Oxide" Part I (Ed. D.J.Craik), Wiley-International N.Y. (1975)

7 .10. J.S.Thorp, M.D.Hossain and L.J.C.Bluck, J. Mat. Sci. 14, 2853 (1979)

7 .11. J.E.Wertz and P.Auzins, Phys. Rev. 106, 484, (1957).

7 .12. G.Rlus and A.Herve, Solid State Comm. 11, 795, (1972)

7 .13. F.G.Marchal and V.W.Parnpton, J. Phys. C. 1, 594, (1968)

7 .14. J.R.Flectcher and K.W.H.Steven, J. Phys. C. 2, 444, (1969).

7 .15. F.S.Hann, Phys. Rev. B4, 3854, (1971)

7 .16. A.R.Skinner, Ph.D. Thesis, Durham University (1986).

CHAPTER EIGHT

MAGNESIOCHROMITE FORMATION
AND EPR LINEWIDTHS IN Cr/MgO

8.1 Introduction

In a number of previous epr studies the linewidth versus concentration behaviour of several magnesia systems doped with transition metal ions has been investigated. These studies included for example Cr/MgO [8.1], and Mn/MgO [8.2] where the main interest was to use the systems as vehicles for testing the validity of epr line broadening theories, particularly of dipolar interaction between isolated or clustered ions. The Fe/MgO system has also been extensively examined, [8.3,8.4,8.5] and it was shown that, in Fe doped crystals, magnesio-ferrite precipitates are formed. These ferrimagnetic precipitates have been studied in some depth partly because of their interest as a system exhibiting fine particle magnetism and partly because the frequent occurrence of iron as an impurity in some commercial magnesias used for refractory insulators raises the question of the role of impurites or heat induced phases in determining the electrical properties of the ceramic. In the present work on the Cr/MgO system the main aim was to re-examine the epr linewidth versus concentration variation so as to be able to make a comparison with the de Biasi and Fernandes broadening theory [8.6] which takes account of exchange interactions as well as the previously discussed

purely dipolar broadening mechanism [8.7,8.8].

The Spin Hamiltonian parameters of various Cr/MgO epr spectra have been fairly extensively reported. Chromium was first detected in MgO as isolated Cr^{3+} ions in sites of octahedral symmetry [8.9]. Since then the Cr^{3+} spectrum has been observed by several other groups e.g. [8.10] and Cr^{3+} has also been found in sites of tetragonal [8.11] and orthorhombic [8.12] symmetry. The Cr^{2+} ion is not detectable with conventional epr but has been observed by acoustic paramagnetic resonance [8.13]. The Cr^{+} species has only been reported in irradiated MgO [8.14]. Chromium tends to adopt the $(+3)$ oxidation state, even where it substitutes for a $(+2)$ ion, and Cr^{+2} is only found in appreciable quantities in samples which have been prepared in a reducing atmosphere [8.15]. The Cr^{3+} ions which enter the MgO lattice show a strong preference for octahedral co-ordination [8.16]. However, it is difficult for Cr^{3+} ions to compensate for their single excess positive charge with respect to the Mg^{2+} ions of the host lattice either by valency variation or by the inclusion of cationic vacancies. This leads to a lack of solubility of Cr^{3+} ions in MgO : there seems to be a saturation concentration of isolated ions which the MgO lattice can support. Any remaining Cr^{3+} ions tend to cluster and form precipitates of the spinel $MgCr_2O_4$ which is electrically neutral and therefore provides its own internal charge compensation.

The lack of solubility of Cr^{3+} in MgO and the consequent formation of magne-

siochromite has been studied by several groups of workers [8.17] using a variety of analytical techniques including EPR, x-ray diffraction, diffuse reflectance spectroscopy and magnetic susceptibility measurements. It has been established that incorporation of equal quantites of Cr^{3+} and Li^+ ions leads to dispersion of the chromium ions, because no charge compensation is required for Cr^{3+} -Li^+ pairs. It thus appears that, in Cr/MgO crystals grown by electrofusion, such as those examined here, the expected behaviour at low concentrations is that the chromium will exist mainly as Cr^{3+} ions which are isolated and substitute for Mg^{2+} ions. In these circumstances, the Cr^{3+} excess charge will be compensated by Mg^{2+} vacancies, one vacancy for every two Cr^{3+} ions. At higher doping levels (greater than one atomic percent) the Cr^{3+} ions cluster and combine with Mg^{2+} ions, O^{2-} ions and vacancies to form precipitates of the spinel phase, $MgCr_2O_4$ .This has implications for linewidth studies, which are discussed below.

8.2 Spinel Structure

The general formula of spinel like compounds is XY_2O_4 , where X is usually a divalent cation and Y a trivalent cation. The crystal structure is cubic and like the magnesium oxide structure, is based upon a close-packed face-centred cubic arrangement of the oxygen anions. However, the spinel unit cell is much larger than that of MgO and contains a total of 32 anions and 24 cations.

The 24 cations fill the interstitial sites in the cubic close packed array of O^{2-} ions; there are a total of 96 such sites in each unit cell. Sixty four of the interstitial sites are each tetrahedrally surrounded by four O^{2-} anions and the remaining 32 are each octahedral surrounded by six O^{2-} anions. Only one eighth of the tetrahedral or type 'A' sites and one half of the octahedral or type 'B' sites are actually occupied by cations. In the case of normal spinels the divalent cations occupy the tetrahedral A sites and the trivalent cations occupy the octahedral B sites. A spinel is referred to as being inverse if half the trivalent cations occupy A sites (the remaining trivalent and divalent cations are randomly distributed among the octahedral B sites). Disordered spinels have the divalent and trivalent cations randomly distributed over all the A and B sites.

Magnesiochromite is a normal spinel (the 8 Mg^{2+} ions occupy tetrahedral sites and the 16 Cr^{3+} ions occupy octahedral sites in the unit cell). This is because the crystal field stabilization energy of Cr^{3+} ions is much greater in octahedral than in tetrahedral sites and therefore they will preferentially occupy the octahedral interstices[8.16]. Since the spinel and magnesium oxide crystal structures are both based on the same cubic close packed array of O^{2-} anions, precipitates of compounds with the spinel structure tend to form in MgO with their crystallographic axes aligned with those of the host lattice i.e the lattice of the spinel precipitate is in register with that of the host MgO crystal. That precipitates of $MgCr_2O_4$ and $MgFe_2O_4$ can form in MgO without distorting the arrangement of the anions in the surrounding host

lattice is also suggested by the fact that the lattice parameters of these compounds are almost exactly twice that of MgO ($a_{MgO} = 4.2112\overset{\circ}{A}$; $a_{MgCr_2O_4} = 8.32\overset{\circ}{A}$; $a_{MgFe_2O_4} = 8.37\overset{\circ}{A}$).

8.3 E P R Linewidth Theories .

Recently, de Biasi and Fernandes [8.6] have modified the Van Vleck [8.7] and Kittel and Abrahams [8.8] dipolar broadening theories to include the effect of exchange interactions. In dilute solid solutions the effect of exchange is quite different from its effect in concentrated solutions i.e. in substances where all or almost all of the cationic sites are populated by paramagnetic ions. In the latter case, the exchange interaction leads to exchange narrowing [8.7]. In dilute solutions, the probability that several ions are coupled together by exchange forces is very low. On the other hand, there is a significant number of pairs of exchange coupled ions. These pairs do not contribute to the broadening of the main resonance line, since the ground state of such a pair (assuming antiferromagnetic coupling, as is usually the case) is a singlet. Ions which are too far apart to be exchange coupled only interact with each other via the dipolar mechanism. The de Biasi and Fernandes approach quantifies the number of exchange coupled pairs in a dilute solid solution and excludes the ions so coupled from the summation terms in the expressions [8.18] for the dipolar linewidth and cut-off fields of the truncated Lorentzian lineshape.

In his dipolar broadening theory, Van Vleck [8.7] assumed that there is no hyperfine interaction or zero-field splitting of the spin energy levels, and this restricts the range of application of the theory. As the Kittel and Abrahams and de Biasi and Fernandes models are both based on Van Vleck's original theory, their models only hold for ions with S = 1/2 in any symmetry or for ions with $S < 2$ in cubic symmetry. On the other hand, Pryce and Stevens [8.19] demonstrated that Van Vleck's theory (and therefore Kittel and Abrahams and de Biasi and Fernandes models) can be applied in the presence of hyperfine interactions to each of the lines of the hyperfine structure, provided that the hyperfine splitting is larger than the linewidth of the individual lines. Hence de Biasi and Fernandes' model is directly applicable to Cr^{3+}ions in magnesium oxide. The de Biasi and Fernandes' model leads to the following general expressions:

$$\triangle H_{pp} = (\pi/2\sqrt{3})A(S)f_e[S_{1\theta}(r_e)]^{3/2}[S_{2\theta}(r_e)]^{-1/2} \qquad (8.1)$$

$$H_c = H_0 \pm (3/2)B(S)\,[S_{2\theta}(r_e)/S_{1\theta}(r_e)]^{1/2} \qquad (8.2)$$

Here $A(S)$and $B(S)$are constants which depend upon the parameters characterizing the paramagnetic ion and the host lattice i.e:

$$A(S) = \frac{\mu_0 g\beta}{4\pi a^3}\,[\frac{S(S+1)}{1.4 + 0.3(S^2 + S)^{-1}}]^{1/2} \qquad (8.3)$$

$$B(S) = \frac{\mu_0 g\beta}{4\pi a^3}[0.3 + 1.4S(S+1)]^{1/2} \qquad (8.4)$$

and a is the nearest neighbour distance in the host lattice. The other components of equations (8.1) and (8.2) are defined as follows :

$$f_e = f(1 - f)^{z(r_e)} \qquad (8.5)$$

111

$$S_{1\theta}(r_e) = a^6 \sum_{r_{jk}>r_e} r_{jk}^{-6}(1 - 3cos^2\theta_{jk})^2 \qquad (8.6)$$

$$S_{2\theta}(r_e) = a^{12} \sum_{r_{jk}>r_e} r_{jk}^{-12}(1 - 3cos^2\theta_{jk})^4 \qquad (8.7)$$

In these relations f_e is the concentration of substitutional ions not coupled by the exchange interaction, r_e is the effective range of the exchange interaction and $z(r_e)$ is the number of cationic sites included in a sphere of radius r_e. For powdered samples, the powers of the direction cosines in equations (8.6) and (8.7) can be replaced by their averages over a sphere ($(1 - 3cos^2\theta_{jk})^2 = 4/5$ and $(1 - 3cos^2\theta_{jk})^4 = 48/35$). The peak-to-peak linewidth and the cut off fields are then given by :

$$\triangle H_{pp} = C_1 A(S) \qquad (8.8)$$

$$|H_c - H_0| = C_2 B(S) \qquad (8.9)$$

where

$$C_1 = (\pi\sqrt{7/15})f_e[S_1(r_e)]^{3/2}[S_2(r_e)]^{-1/2} \qquad (8.10)$$

$$C_2 = (3\sqrt{21/7})[S_2(r_e)/S_1(r_e)]^{1/2} \qquad (8.11)$$

$$S_1(r_e) = a^6 \sum_{r_{jk}>r_e} r_{jk}^{-6} \qquad (8.12)$$

$$S_2(r_e) = a^{12} \sum_{r_{jk}>r_e} r_{jk}^{-12} \qquad (8.13)$$

The values of the coefficients C_1 and C_2 are independent of the parameters of the paramagnetic ion and the host lattice. C_1 is a function of the total concentration of the paramagnetic ion, the range of the exchange interaction and the lattice geometry. C_2 depends only on the lattice geometry and the range of the exchange interaction.

To apply de Biasi and Fernandes theory to impurity ions distributed in magnesium oxide powders we need to compute the values of C_1 and C_2 for an FCC lattice. C_1 and C_2 are readily determined once the values of the summations $S_1(r_e)$ and $S_2(r_e)$ defined by equations (8.12) and (8.13) are known. As the convergence of these summations is relatively slow, their evaluation becomes much easier if they are written in the form :

$$S_1(r_e) = a^6 [S_1(\infty) - \sum_{r_{jk}<r_e} r_{jk}^{-6}] \tag{8.14}$$

$$S_2(r_e) = a^{12} [S_2(\infty) - \sum_{r_{jk}<r_e} r_{jk}^{-12}] \tag{8.15}$$

The values of $S_1(\infty) = \sum r_{jk}^{-6}$ and $S_2(\infty) = \sum r_{jk}^{-12}$ for an FCC lattice are given in the literature [8.23]. If the paramagnetic ions occupy cationic sites in the host lattice the radius vectors, r_{jk}, may be determined using trigonometry. The results for a general FCC lattice are shown in Table 8.1. Here n is the number of the order of each coordination (n=1 includes no neighbouring sites, n=2 the nearest neighbour sites and so on), $r = r_{jk}/a$ is the radius of the corresponding sphere and N is the number of cationic sites on the surface of the nth coordination sphere. The summations $S_1(r_e)$ and $S_2(r_e)$ are truncated at the surface of a particular coordination sphere, depending on the range of the exchange interaction.

The values of C_1 and C_2 are shown in Figure 8.1 and Table 8.2 respectively. The concentration dependence of C_1, illustrated in Figure 8.1 for ten different ranges of the exchange interaction, shows that, for the same impurity concentration, the value of C_1, and hence the linewidth, tends to decrease as the range of the exchange

n	r	N	Nr^{-6}	Nr^{-12}	$S_1(r_e)$	$S_2(r_e)$
2	$\sqrt{2}/2$	12	96.000	768.000	19.631	8.440
3	$\sqrt{3}/2$	6	6.000	6.000	13.631	2.440
4	1	24	7.104	2.102	6.527	0.338
5	$\sqrt{2}$	12	1.500	0.187	5.027	0.151
6	$\sqrt{10}/2$	24	1.536	0.098	3.491	0.053
7	$\sqrt{3}$	8	0.296	0.011	3.195	0.042
8	$\sqrt{14}/2$	48	1.104	0.024	2.091	0.018
9	2	6	0.096	0.002	1.995	0.016
10	$3\sqrt{2}/2$	36	0.396	0.004	1.599	0.012

Table 8.1: Calculated values of $S_1(r_e)$ and $S_2(r_e)$ for the FCC lattice.

n	C_2	$z(r_e)$
1	5.089	0
2	1.288	12
3	0.831	18
4	0.447	42
5	0.340	54
6	0.242	78
7	0.225	86
8	0.182	134
9	0.176	140
10	0.172	176

Table 8.2: Calculated values of C_2 and $z(r_e)$ for the FCC lattice.
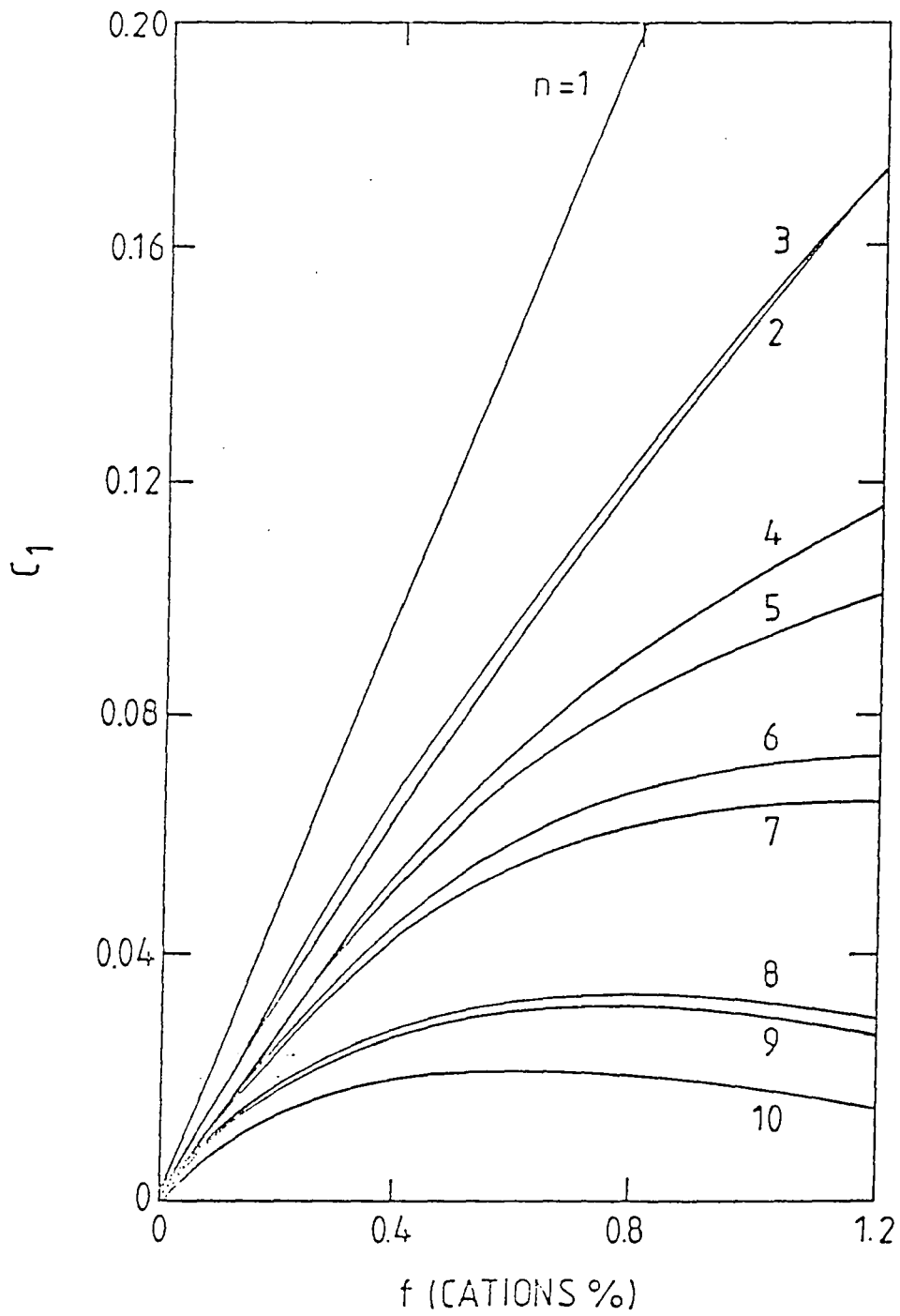
Figure 8.1: Concentration dependence of the linewidth coefficient C_1 for a face-centred cubic lattice and several ranges of the exchange interaction.

interaction is increased. Table 8.2 demonstrates that the coefficient C_2, and thus the value of $|H_c - H_0|$, decreases as the range of the exchange interaction is increased.

If clustering effects are important the model can still be used provided that the equation :

$$f_e = f(1 - pf)^{z(r_e)} \tag{8.16}$$

is used in place of equation (8.5) (p is known as the "clustering factor " and is defined as the ratio of the actual probability that a neighbouring cationic site is occupied to the probability of occupation if the distribution were random). In applying the theory to the Cr^{3+} linewidths examined here the major steps in the analysis are to calculate the theoretical dependence of the peak-to-peak linewidth upon dopant concentration for various values of n from equation (8.8), [A(S) is a numerical constant which simply depends upon the parameters characterizing the dopant ion and is given by equation (8.3); C_1 may be determined for various values of n and at a number of different dopant concentrations with the aid of Tables 8.1 and 8.2 equation (8.5) and (10)], to compare a graph of experimental peak-to-peak linewidth against concentration with the theoretical curves to determine n and finally to obtain the values of r_e and C_2 corresponding to n from Tables 8.1 and 8.2.

8.4 Experimental Techniques.

The E.P.R spectra were recorded at room temperature with a Varian V4502-12

9GHz spectrometer for a series of Cr doped MgO single crystals and powders which had a nominal range of Cr concentration from 800 ppm Cr to 15000 ppm Cr. All the single crystals were also examined by reflection high energy electron diffraction (RHEED) in order to detect the presence of the spinel phase in the cubic MgO host matrix. In order to remove residual strain (which would lead to line broadening [8.20]) heat treatment at an annealing temperature of 500°C was chosen. The phase diagram of the MgO-$MgCr_2O_4$system, Figure 8.2, indicates that, at this temperature and for dopant concentrations of the order of 1%, two phases will exist. In the case of chromium doped MgO these phases are a solid solution of Cr^{3+}ions in MgO and the spinel $MgCr_2O_4$. In the as received state, the more lightly doped Cr/MgO single crystals (those containing 800 ppm, 3600 ppm and 7400 ppm of chromium) did not display diffraction spots due to the spinel $MgCr_2O_4$in their RHEED diffraction patterns. Consequently, these crystals were heat treated at 800°C in an oxygen atmosphere for 10 hours and then quenched to room temperature. It was hoped that the higher temperature would promote growth of the spinel phase and that quenching would preserve the high temperature distribution of the Cr^{3+}ions between the solid solution and clustered phases thereby enabling the spinel spots to be observed on re-examination by RHEED. The main evidence for the formation of magnesio-chromite precipitates came from RHEED investigations. Five as received single crystals of Cr/MgO with different dopant concentration were examined using RHEED. The work was carried out on a JEM -120 electron microscope operating at 100 kV. The electron beam of the microscope impinged upon the large face of the sample under investigation
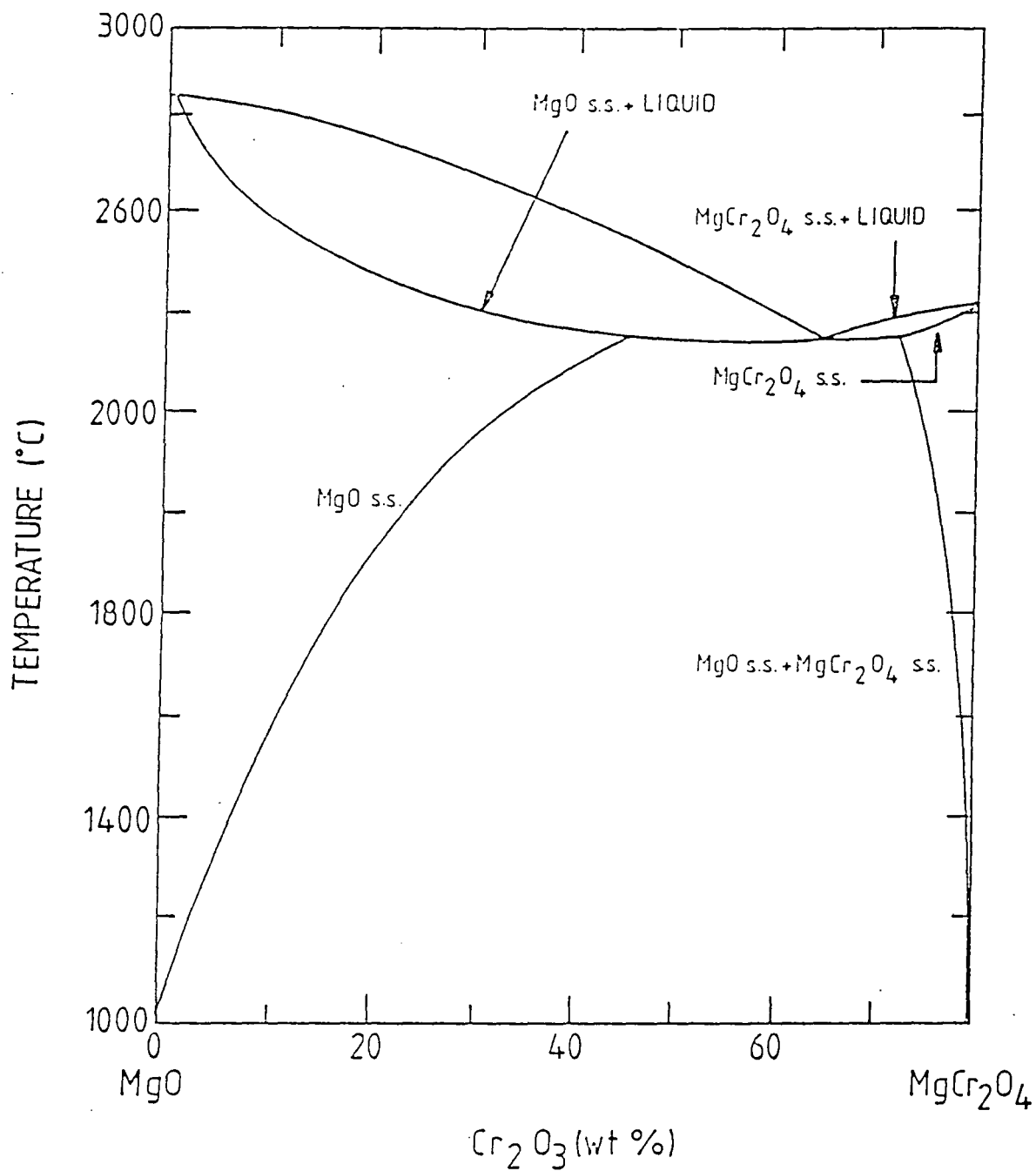
Figure 8.2: Phase equilibrium diagram for the system MgO-$MgCr_2O_4$

(which had typical dimensions of 10 mm x 5 mm x 1 mm) at a glancing angle (one or two degrees) and was diffracted by the crystal lattice.

A comprehensive account of the RHEED technique has been given by Russell [8.21]. Further experimental and theoretical details which are particularly relevant to the RHEED work reported in this section are given by Inglis [8.22] who, using a similar approach to that adopted here, investigated the formation of the spinel magnesioferrite ($MgFe_2O_4$) in iron doped MgO.

The samples to be investigated were cleaned in acetone, dried in air and then etched in fuming nitric acid for varying lengths of time. The etchant attacks MgO much more rapidly than it attacks the spinel precipitates; this results in the formation of etch hillocks on the sample surface with spinel phase material at the peaks. Thus, etching in this way will cause the electron beam to irradiate spinel precipitates preferentially when it is glanced off the surface. The spots in the diffraction pattern arising from the precipitates are therefore artificially increased in intensity compared with those arising from the MgO host material, thereby increasing the sensitivity of RHEED to the presence of the spinel phase.

8.5 RESULTS.

8.5.1 EPR Linewidth Results.

8.5.1.1 Single Crystals .

The peak-to-peak linewidth of the central transition of the cubic Cr^{3+} spectrum (which represents three coincident lines corresponding to the $M = +1/2 \leftrightarrow -1/2$ and $M = \pm 3/2 \leftrightarrow \pm 1/2$ transitions) was measured with the magnetic field parallel to a $< 100 >$ direction in the crystal for each doped sample. The values obtained are plotted against total nominal chromium concentration in Figure 8.3. The least squares method was used to fit the experimental points to the cubic equation :

$$\triangle H_{pp}(mT) = 0.27 + 3.44 \times 10^{-4}[Cr]$$

$$-5.55 \times 10^{-8}[Cr]^2 + 2.25 \times 10^{-12}[Cr]^3 \qquad (8.17)$$

where [Cr] is the nominal chromium concentration in ppm by weight

It is clear from Figure 8.3 that the experimental dependence of EPR linewidth upon chromium concentration does not agree with that predicted by the dipolar broadening theory of de Biasi and Fernandes. The measured linewidths are much smaller than expected and the form of the experimental curve does not correspond with that of any one of the theoretical curves calculated for different ranges of the exchange interaction using de Biasi and Fernandes model. Indeed, the measured linewidths are so much smaller than those predicted by dipolar broadening theory, it
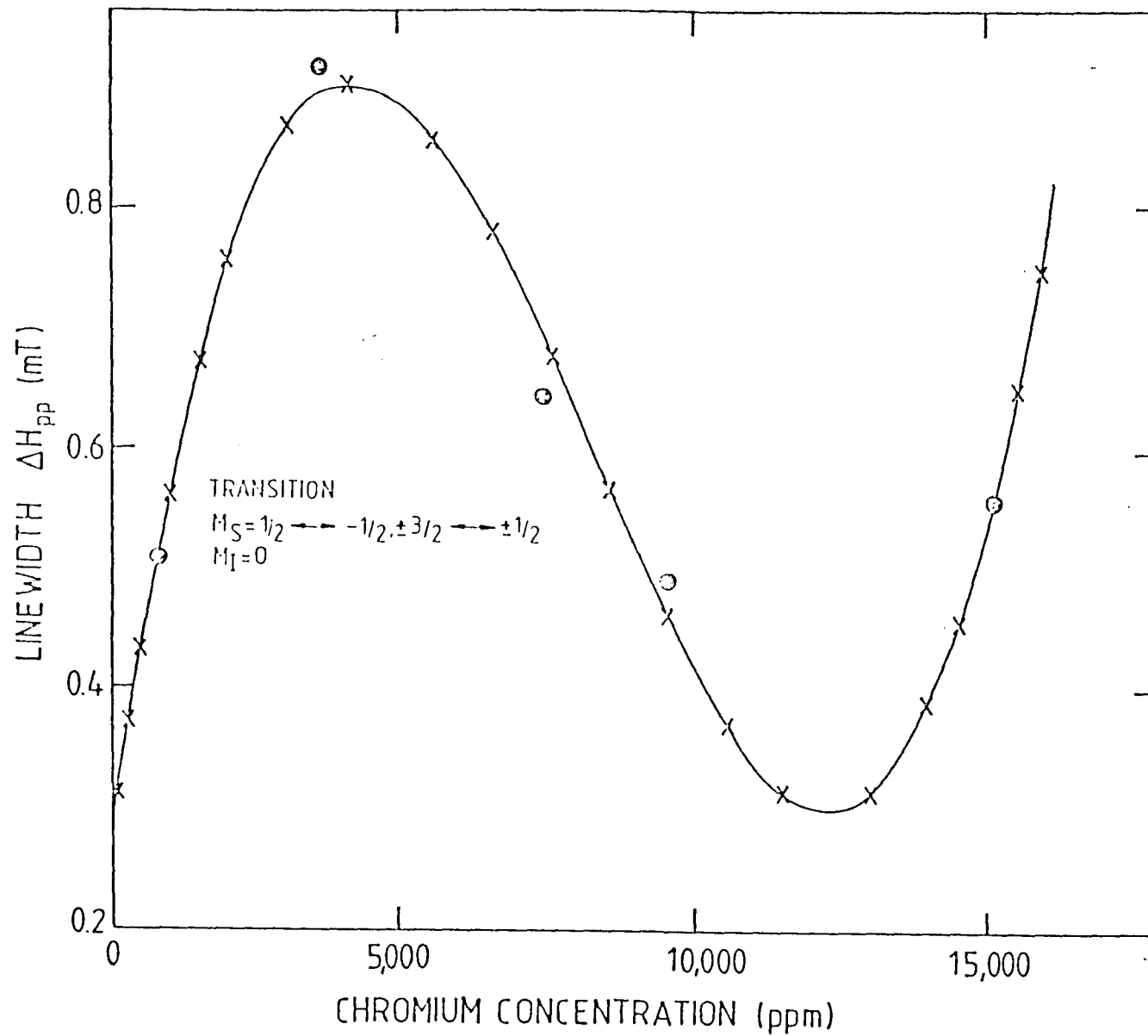
117

Figure 8.3: Variation of linewidth with chromium concentration for single crystal Cr/MgO (293K, H// <100>); experimental (⊙), equation 17 (x).

has been assumed in the past, quite reasonably, that the central transition linewidth is independent of the chromium concentration [8.10]. Strictly speaking, the de Biasi and Fernandes model, is only valid for powders. Consequently further measurements were made on a series of powdered single crystals.

8.5.1.2 Powdered Single Crystals .

The linewidth between points of maximum slope, $\triangle Hpp$, of the central transition in the cubic Cr^{3+} spectrum was measured for each powder sample and each heat treated powder sample and the values obtained are plotted against total nominal chromium concentration in Figures 8.4 and 8.5 respectively. The data points lie on curves described by cubic equations. Using the least squares method , the equation giving the best fit to the experimental points for the powder samples was found to be :

$$\triangle H_{pp}(mT) = 0.36 + 2.98 \times 10^{-4}[Cr]$$

$$-4.74 \times 10^{-8}[Cr]^2 + 1.92 \times 10^{-12}[Cr]^3 \qquad (8.18)$$

whilst for the annealed powder samples the best fit was obtained for the equation :

$$\triangle H_{pp}(mT) = 0.49 + 1.18 \times 10^{-4}[Cr]$$

$$-2.33 \times 10^{-8}[Cr]^2 + 1.01 \times 10^{-12}[Cr]^3 \qquad (8.19)$$

where [Cr] is the nominal total chromium concentration in ppm. The variation of linewidth with chromium concentration for the powder samples and also for the heat
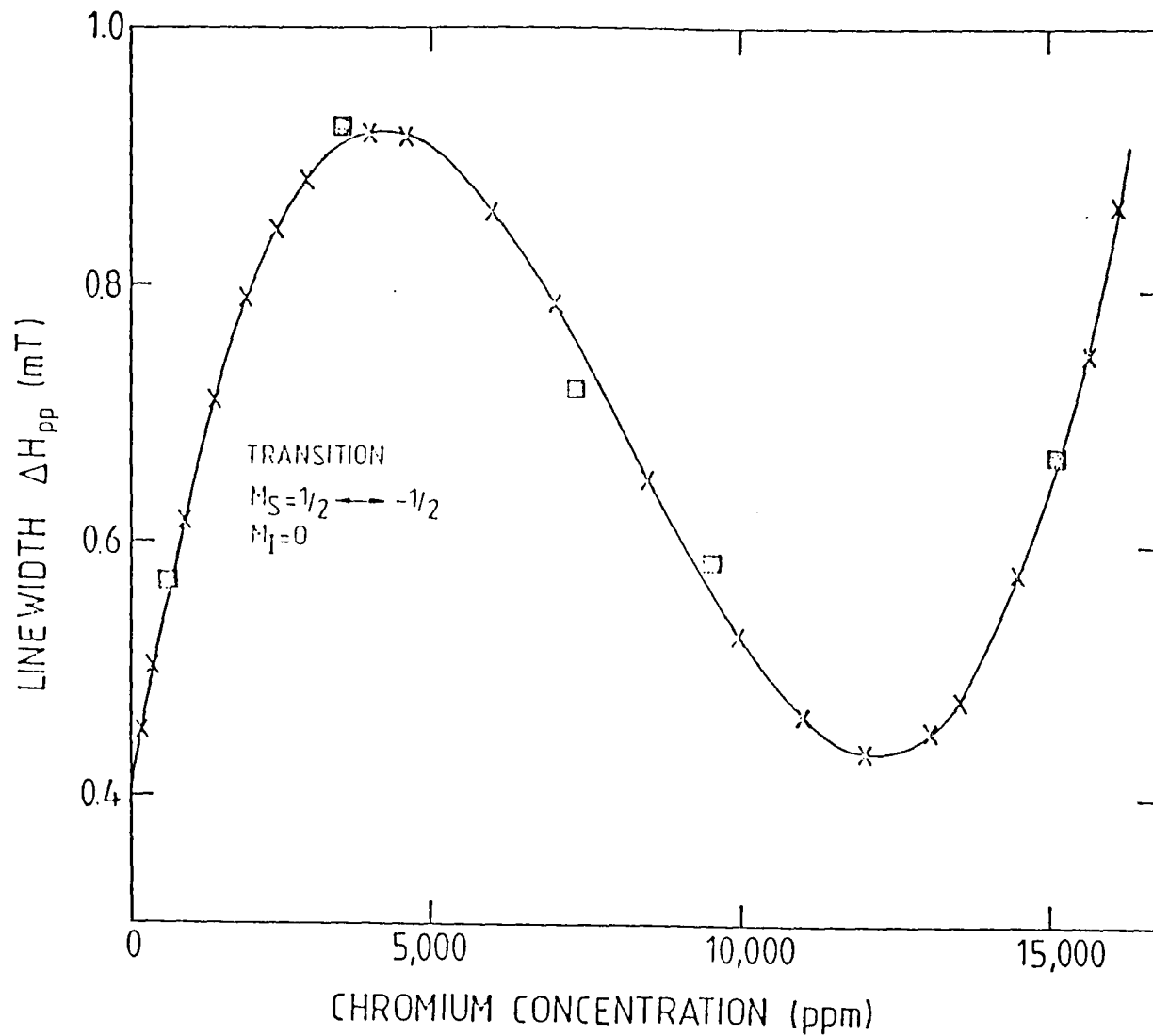
Figure 8.4: Variation of linewidth with chromium concentration for powdered Cr/MgO; 293K; experimental (□), equation 18, (x).
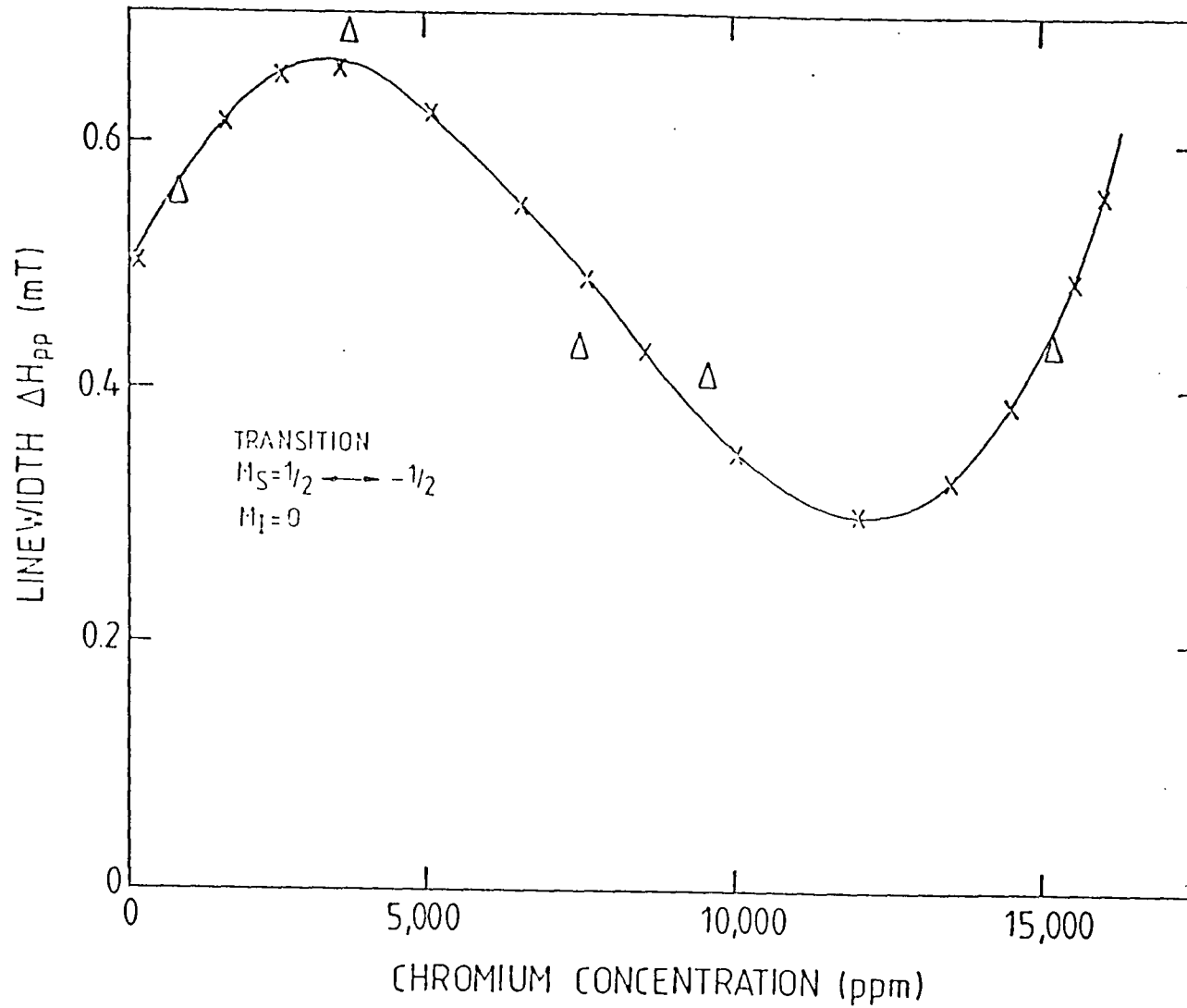
Figure 8.5: Variation of linewidth with chromium concentration for annealed Cr/MgO powders; 293K; experimental (Δ), equation 19, (x).

treated powder samples is very similar in form to that for the single crystal samples when H is parallel to a $< 100 >$ direction in the crystal (see Figure 8.3). Thus the experimental dependence of linewidth upon nominal chromium concentration for both the powder and annealed powder samples cannot be explained solely in terms of de Biasi and Fernandes dipolar broadening theory although Cr/MgO is an ideal system to which their theory may be applied. We suggest that the discrepancy between theory and experiment is due to the fact that a significant proportion of the chromium dopant exists in precipitates of the spinel phase $MgCr_2O_4$.

8.5.2 RHEED Results .

The RHEED pattern shown in Figure 8.6 was obtained from the sample doped with 800 ppm of chromium after it had been etched for 1 minute, and was obtained with the electron beam almost parallel to a $< 100 >$ direction. The MgO lattice is face centred cubic and, the diffraction spots may be indexed with reciprocal lattice points corresponding to the reflecting planes producing the spots which are consistent with this type of lattice. Furthermore, the spacings of the diffraction spots confirm that the face centred cubic lattice producing these RHEED patterns has a lattice parameter equal to that of MgO.

Similar patterns were obtained from the samples doped with 3600 ppm and 7400 ppm of chromium. Variation of the etching time did not produce any changes in

the patterns observed. Figure 8.7 was obtained from a sample doped with 15100 ppm of chromium after it had been etched for one minute . The spots which are wholly or partially due to MgO may be determined by comparing Figures 8.6 with 8.7 (the MgO spots are more intense than the rest in the patterns of Figure 8.7). The additional spots which appear in Figure 8.7 arise from a second cubic lattice which is in alignment with the MgO host lattice and which has a lattice parameter equal to twice that of MgO. It is thought that the additional spots are caused by precipitates of the spinel magnesiochromite $MgCr_2O_4$ which, in the bulk, has a lattice parameter of $8.333\AA$ almost exactly twice that of MgO ($a_{MgO} = 4.2112\AA$). The indices given to the diffraction spots refer to the Miller indices of the reflecting planes in the $MgCr_2O_4$ lattice which are responsible for them. Evidence that the assignment of the additional spots to $MgCr_2O_4$ is reasonable is provided by the x-ray ASTM index card of this material, which, although it refers to x-ray diffraction, is equally applicable to RHEED data. Firstly, of the reflections which the ASTM index indicates are allowed, all are either present, or would be present at positions which overlap with the spots due to MgO reflections, in Figure 8.7. Secondly, the reflections which the ASTM index predicts will be absent are either absent or overlap with host lattice reflections, so that it is not possible to determine whether there are spinel spots at these positions.

The etching time did have an effect upon the RHEED patterns of the samples for which spinel spots were observed. For etching times greater than one minute rings were also observed, as shown in Figure 8.8 which illustrates the RHEED patterns
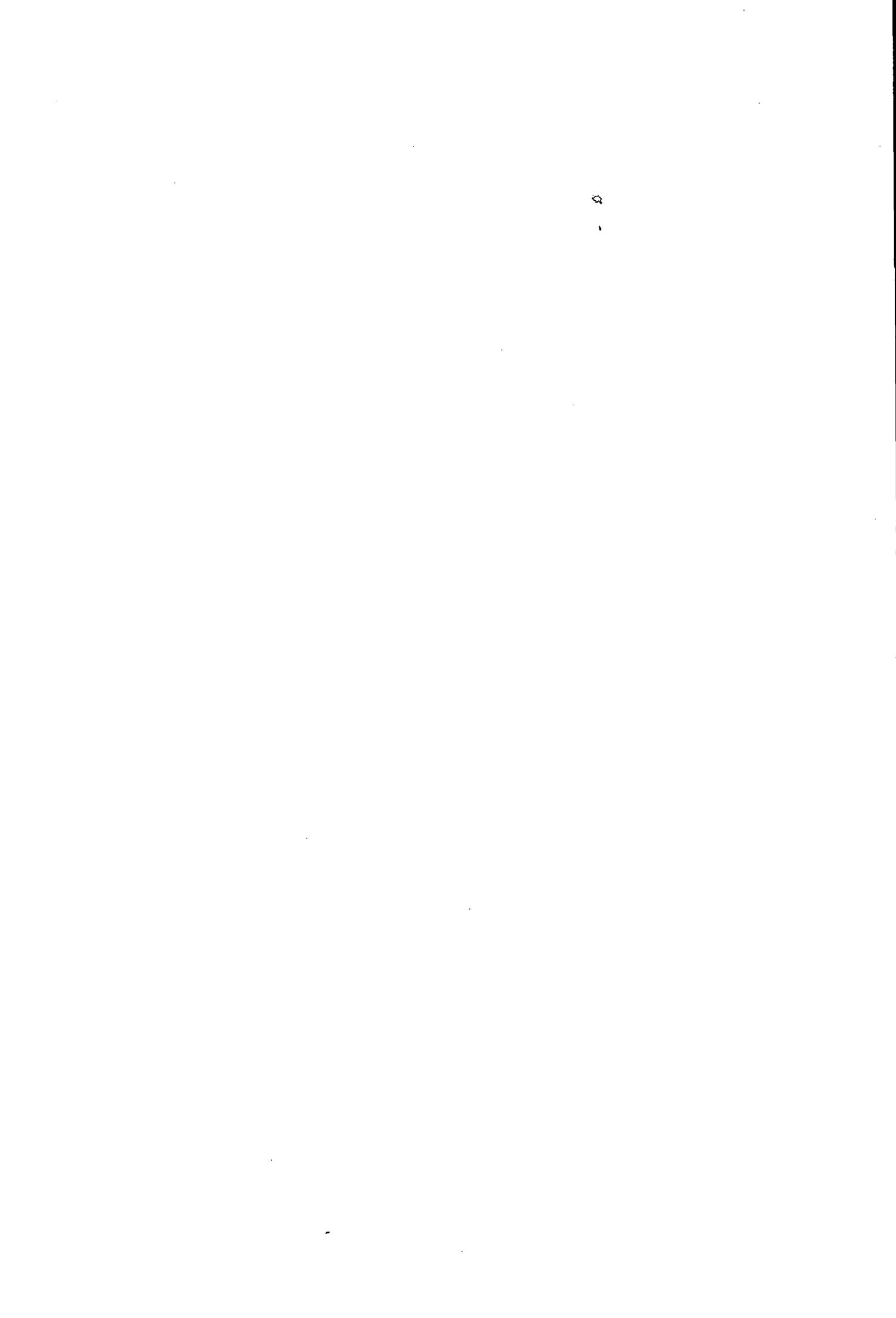
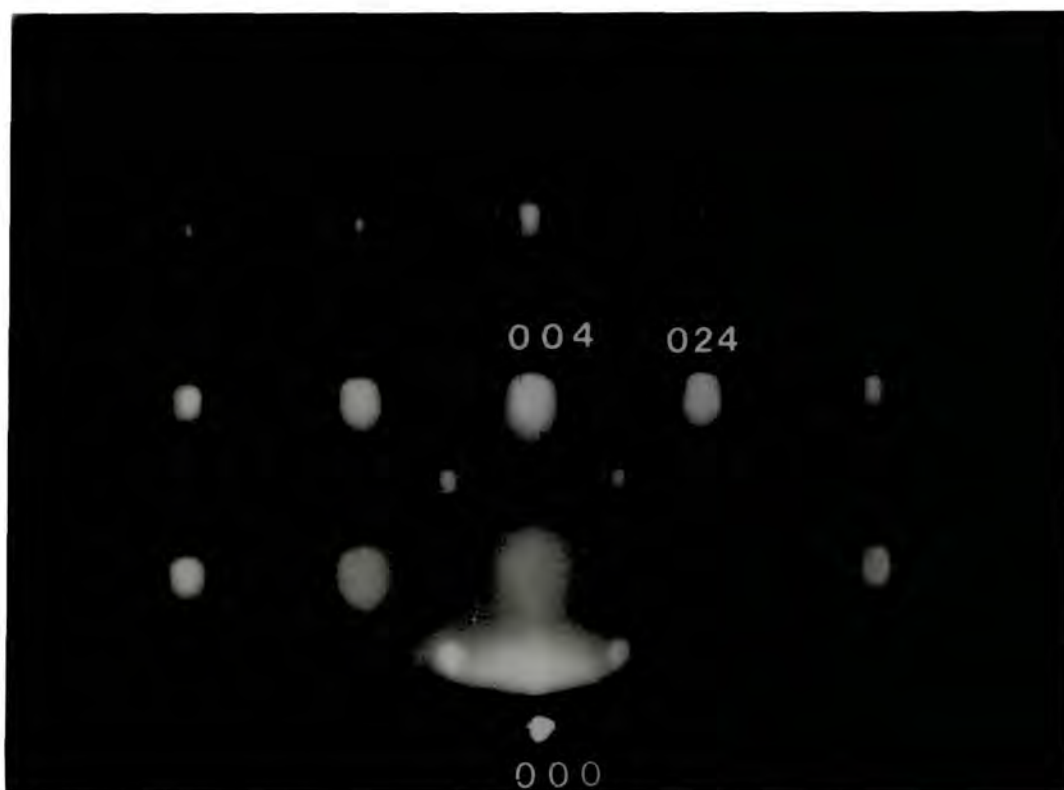Figure 8.6: RHEED pattern from Cr/MgO single crystal; dopant concentration 800ppm, teching time 1 min.

Figure 8.7: RHEED pattern from Cr/MgO single crystal; dopant concentration 15,100ppm, etching time 1min.
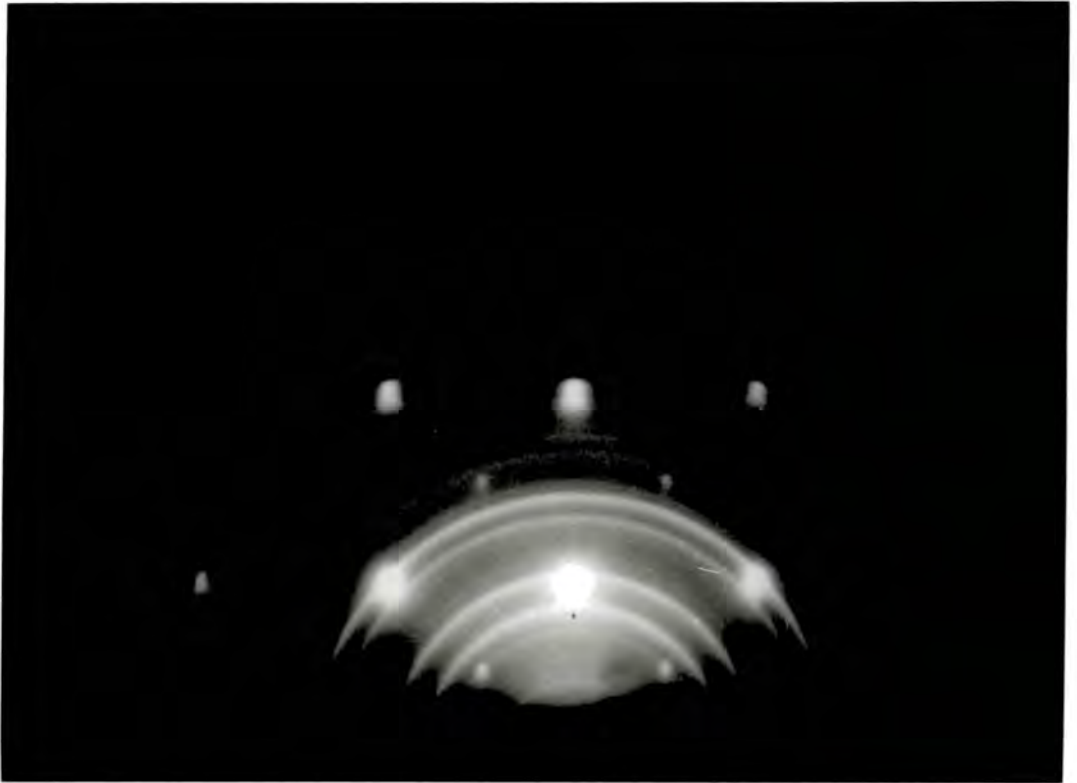
Figure 8.8: RHEED pattern from Cr/MgO single crystal; dopant concentration 15,100ppm, etching time 25 min.

recorded with the electron beam parallel to a< 100 > direction for the sample doped

with 15100 ppm of chromium after it had been etched for 25 minutes. The pattern of

rings is consistent with them being due to the spinel precipitate and not the MgO host.

As rings are an indication of polycrystallinity, the spinel precipitates responsible for

the rings are not aligned with the MgO host lattice but have random orientations. It is

thought that excessive etching causes the base of the etch hillocks which is composed

of MgO to be dissolved away, thereby depositing the insoluble spinel precipitates,

initially located at the peaks of the etch hillocks, onto the sample surface. The

precipitates will be deposited on the surface with random orientations and hence give

rise to a "powder" diffraction pattern composed of rings. The lightly doped samples

(those containing 800 ppm, 3600 ppm and 7400 ppm of chromium), whose RHEED

patterns did not show the presence of magnesiochromite were heat treated at 800°C

for 10 hours in an oxygen atmosphere in order to try to induce growth of the spinel

phase. Re-examination by RHEED showed that only in the sample doped with 7400

ppm of chromium had any spinel precipitates been formed.

8.6 Discussion .

In a recent paper de Biasi and Fernandes analysed experimental linewidth data

for a series of Cr/MgO powders in terms of their theoretical model and found that

the linewidth of the central transitions in the cubic Cr^{3+} spectra recorded laid on the

theoretical curve for n=5 (see Figure 8.1). Substituting the constants appropriate for

chromium and the value n=5 into equation (8.8), it follows that the dependence of the linewidth between points of maximum slope upon chromium concentration for de Biasi and Fernandes samples obeys the equation:

$$\triangle H_{pp}(mT) = 629f(1 - f)^{54} \qquad (8.20)$$

where f is the fractional chromium concentration of isolated Cr^{3+} ions. We suggest that the difference between the concentration dependence of the linewidth in the present samples and the examined by de Biasi and Fernandes could be accounted for by the fact that $MgCr_2O_4$ precipitates are present in our annealed powder samples but not in de Biasi and Fernandes. Using equation (8.20), we can find the points on the curve of this equation corresponding to the linewidths measured for our samples and read off from the fractional concentration axis the concentrations of chromium existing as isolated Cr^{3+} ions in cubic sites. This procedure has been carried out for the annealed powder samples and the deduced isolated Cr^{3+} ion concentrations in sites of octahedral symmetry are given in column three of Table 8.3 in units of ppm. The remainder of the dopant is assumed to exist in the $MgCr_2O_4$ phase and the concentrations of this species (calculated simply by subtracting the isolated ion concentration) from the total nominal dopant concentration are given, in ppm, in column four of Table 8.3. The deduced concentrations, while approximately correct, do not take account of the small fraction of the dopant which exists as isolated Cr^{3+} ions in sites of axial symmetry. Inspection of Table 8.3 shows that the isolated Cr^{3+} ion concentration in the annealed powder samples examined lies in the range 870 ppm. Cordischi et al [8.17] estimated the relative concentrations of isolated Cr^{3+} ions

Total Nominal Chromium Concentration (ppm)	$\triangle H_{pp}$ mT (Experimental)	Cr^{3+} Concentration (ppm)	
		Isolated Ion	Spinel
3600	0.960	1514	2086
7400	0.437	902	6498
9500	0.416	870	8630
15100	0.442	934	14166

Table 8.3: Concentration of Cr^{3+} existing as isolated ions and the spinel $MgCr_2O_4$ for the annealed powder samples.

and $MgCr_2O_4$ in Cr/MgO samples prepared in air by comparing the intensity of the central transition in the cubic Cr^{3+} spectrum to that of the broad line attributed to the spinel phase. They found that the isolated Cr^{3+} ion concentration ranged from approximately 1800 ppm to 2700 ppm in the samples examined. Considering the different preparation conditions, one might expect that, as is found experimentally, the degree of solubility of Cr^{3+} in the host lattice differs between Cordischi et al samples and the ones examined here. Even so, both sets of results indicate that the solubility of Cr^{3+} in MgO is limited and, allowing for the difficulty in determining absolute concentrations from EPR data, the degree of agreement between our results and Cordischi et al concerning the maximum concentration of Cr^{3+} ions which can enter into solid solution is encouraging.

REFERENCES

8.1. J.S.Thorp and M.D.Hossain J. Mat. Sci. 15, 3041, (1980)

8.2. J.S.Thorp and A.R.Skinner, J. Magnetism and Magnetic Material 69, 34,(1987).

8.3. G.P.Wirtz and M.E.Fine J. Appl. Phys. 38, 3729, (1967)

8.4. A.D.Inglis and J.S.Thorp J. Mat. Sci. 16, 1887, (1981).

8.5. A.D.inglis, G.J.Russell and J.S.Thorp J. Mat. Sci. 17, 2939, (1982).

8.6. R.S.de Biasi and A.A.R.Fernandes J. Phys. C:Solid state Phys. 16, 5381, (1983)

8.7. J.H.Van Vleck Phys. Rev. 41, 208, (1932).

8.8. C.Kittel and Elihu Abrahams Phys. Rev. 90, 238, (1953).

8.9. W.Low Phys. Rev. 105, 801, (1957).

8.10. J.S.Thorp, M.D.Hossain and L.J.C.Bluck J. Mat. Sci. 14, 2853,(1979).

8.11. R.A.Serway, S.A.Marshall and R.B.Robinson Phys. State Solid B 56, 319, (1973).

8.12. J.J.Davies and J.E.Wertz J. Phys. C:Solid State Phys. 8, 1235, (1975).

8.13. F.S.Ham Phys. Rev. B 4, 3854, (1971).

8.14. G.Rius and A.Herve Solid State Comm. 11, 795, (1972).

8.15. D.Cordischi, D.Gazzoli and M.Valigi J. Sol. Sta. Chem. 24,371, (1978).

8.16. J.D.Dunitz and L.E.Orgel J.Phys. Chem. sol. 3, 318, (1957).

8.17. D.Cordischi, J.C.Vickermen and A.Cimino Trans. Faraday Soc. 66, 1312, (1970).

8.18. A.R.Skinner Ph.D. Thesis University of Durham 1986.

8.19. M.H.L.Pryce and K.W.H.Stevens Proc. Phys. Soc. 63, 36, (1950).

8.20. J.S.Thorp, A.R.Skinner and A.S.AL-Hawery J. Magnetisum and Magnetic Material To be published.

8.21. G.J.Russell Prog. Crystal Growth and Charact. 5, 291, (1982).

8.22. A.D.Inglis Ph.D. Thesis University of Durham 1981.

8.23. J.E.Jones and A.E.Ingham Proc. Roy. Soc. A107, 636, (1925).